UNIVERSITÀ
DEGLI STUDI
DI PADOVA

Sede Amministrativa: Università degli Studi di Padova

Centro di Ateneo di Studi ed Attività Spaziali “Giuseppe Colombo” (CISAS)

SCUOLA DI DOTTORATO DI RICERCA IN : SCIENZE TECNOLOGIE E MISURE SPAZIALI
INDIRIZZO: ASTRONAUTICA E SCIENZE DA SATELLITE
CICLO: XXVI

GROUND CALIBRATIONS OF PHEBUS SPECTROMETER ONBOARD OF BEPICOLOMBO MISSION

Direttore della Scuola : Ch.mo Prof. Giampiero Naletto

Coordinatore d’indirizzo: Ch.mo Prof. Giampiero Naletto

Supervisore: Dott.ssa Maria Guglielmina Pelizzo

Co-supervisore: Dott.ssa Zuppella Paola

Dottorando : Alain Jody Corso

for Urania

Abstract

Probing of Hermean Exosphere by Ultraviolet Spectroscopy (PHEBUS) is a two channels spectrometer working in the Extreme Ultraviolet (EUV) and Far Ultraviolet (FUV) range. It will be onboard of ESA Bepicolombo mission and it is devoted to study the composition, the formation mechanisms and the dynamics of the Mercury exosphere. The instrument has French leadership but Russian, Japanese and Italian teams are involved in the project. In particular, the Italian team is responsible of the radiometric ground calibrations of the instrument.
In this work an innovative approach to model the radiometric behavior of an optical instrument is described and applied to PHEBUS. The model obtained takes into account also the effects induced by the polarized light. We have found that, under specific conditions, the radiometric response can be divided into two main components: the *efficiency term* which takes into account the efficiency of each optical element and the *geometrical parameter* which takes into account the geometry of the instrument (field of view, entrance pupil diameter, etc...).
In additional to the theoretical model, the PHEBUS calibration activates carried out at the CNR-IFN UOS Padova laboratory are also presented. All activities are focused to determine and experimentally validate the PHEBUS radiometric model by using both an optical sub-system level and an instrument level measurements. In the sub-system level measurements, each optical component has been characterized in order to retrieve the instrument efficiency. Instead, with instrument level measurements, the geometric parameters which affect the radiometric response as well as the instrument linear range and its spectral behavior can be experimentally determined: all these points will be fully described and the early experimental results presented.

Riassunto

Probing of Hermean Exosphere by Ultraviolet Spectroscopy (PHEBUS) è uno spettrometro a due canali che lavora nell'estremo ultravioletto (EUV) e nel lontano ultravioletto (FUV). Questo spettrometro sarà a bordo della missione ESA BepiColombo e si dedicherà allo studio della composizione, dei meccanismi di formazione e della dinamica dell'esosfera di Mercurio. Lo strumento è realizzato dalla Francia ma ad esso collaborano Russia, Giappone e Italia. In particolare, il team italiano è responsabile delle calibrazioni radiometriche a terra dello strumento.
In questo lavoro, è descritto un innovativo approccio per modellizzare il comportamento radiometrico di uno strumento ed esso è applicato a PHEBUS. Questo nuovo modello consente di considerare anche gli effetti della luce polarizzata sulla risposta radiometrica dello strumento. E' stato trovato che, sotto determinate condizioni, la risposta radiometrica può essere divisa in due parti principali: *il termine di efficienza* che tiene conto dell'efficienza di ogni componente ottico e *il parametro geometrico* che tiene conto della geometria fisica dello strumento (campo di vista, diametro della pupilla d'ingresso, ecc...).
In aggiunta al modello teorico dello strumento, sono anche presentate le attività di calibrazione di PHEBUS che sono state svolte presso il laboratorio del CNR-IFN UOS Padova. Tutte le attività hanno lo scopo di determinare e validare sperimentalmente il modello radiometrico di PHEBUS utilizzando misure a livello dei sotto componenti ottici e dell'intero strumento. Con le misure a livello di sotto componenti, ogni componente ottico è stato caratterizzato allo scopo di determinare l'efficienza dello strumento. Invece, con le misure a livello di strumento, i parametri geometrici che condizionano la risposta radiometrica, il range di linearità dello strumento e il suo comportamento spettrale possono essere caratterizzati sperimentalmente: tutti questi aspetti verranno ampliamente descritti e i primi risultati sperimentali presentati.

Acknowledgements

I thank the French team of PHEBUS for these stimulant years of work. In particular, I wish to thank Jean-Francois Mariscal for the good times we had during the optical sub-systems measurements and the QM activities. I thank Nicolas Rouanet for his many teachings on optics field (and not only) and for the fruitful discussions that we had: I have learned a lot from him. I thank Jean-Luc Maria for the "PHEBUS opportunities" that he gave me and, finally, I enormously thank Eric Quémerais, the PHEBUS Principal Investigator, for his support, his help and his teachings during these three years.

Ringraziamenti

Ci sono molte persone che devo ringraziare per aver contribuito a farmi diventare la persona che sono oggi. I miei genitori e mia sorella Consuelo, che mi hanno sempre supportato ed aiutato, fin da quando ero piccolo, in tutte le cose che volevo o decidevo di fare: loro sono stati i principali autori di questa creazione. Assieme a loro c'è anche Valentina, la mia adorata moglie, che in questi ultimi undici anni mi ha sempre sopportato (notare la o al posto della u nella parola sopportato) ed è stata un punto fermo nella mia vita: di solito si dice *dietro ad un uomo c'è sempre una grande donna* e nel mio caso credo sia proprio vero.
Ringrazio il grande maestro Renato Pante ed i Klomer Brass, composti da Fabio, Giacomo, Lucio ed il sottoscritto, per le divertenti prove ed i bei concerti che da anni proponiamo in giro per l'Italia: come si dice in questi casi, *Onori a Renato Pante e ... ai Klomer Brass!*
Un grazie a tutti gli amici delle principali bande musicali che in questi anni ho frequentato e che tutt'ora frequento (Arsié, Fiera di Primiero, Castello Tesino): con loro, in questi anni mi sono sempre divertito ed ho passato momenti stupendi che rimarranno sempre nei miei ricordi.
All'associazione Rheticus di Feltre, diventata una parte importante della mia vita, per le ore passate a contemplare ed ammirare le bellezze che il cielo stellato ci offre, nonché per tutte le esperienze vissute nel realizzare la nostra piccola *città delle stelle*.
Un grazie a Dino, Fabio, Ilaria, Ivan e Mirko, per le belle serate dopo prove di banda trascorse davanti alla mitica super-pizza di Agana. E, parlando di pizza, un grazie anche a Idea Pizza di Padova per le succulente pizze con patate arroste e sfilacci di cavallo che in questi anni di università e di dottorato hanno reso speciali le pause pranzo.
Infine un grazie al mio supervisore ed a tutti i colleghi incontrati in questi anni al Laboratorio LUXOR per le belle giornate di lavoro e le stimolanti esperienze che mi hanno offerto.

Contents

List of Tables

List of Figures

Introduction

The messenger of the gods

The planet Mercury is the closest rocky planet to the Sun, situated at about one-third of the Sun-Earth distance. This position makes Mercury a planet with extreme environmental conditions in term of temperatures[1] and solar irradiation[2]. Its orbit is elliptical, with an aphelion of $70 \cdot 10^6$ km, a perihelion of $46 \cdot 10^6$ km and an average eccentricity around 0.21. Despite its small Sun-distance, Mercury can be directly observed from Earth when it is far enough from the Sun[3] but with poor information: the maximum apparent diameter reached is only 13" even if it is able to be a very bright object in the sky, with a magnitude that can vary from -2.6 to about 5. In fact, the most of our current knowledge of Mercury is due to the two spacecraft that visited the planet in the past.

Mercury's sidereal period is 87.97 days with an orbital speed close to 50 km per second, faster than any other planet. On the contrary, Mercury has a very slow rotation period of $\simeq$ 58.65 days. This configuration between the orbit period and spin period is said $3:2$ *spin-orbit resonance* because the planet rotates three times for every two revolutions around the Sun; the $3:2$ spin-orbit resonance could be explained by the chaotically variation of the eccentricity induced by the gravitational influence of the Sun and other planets in the solar system [3]. The synodic period is about 176 days obtaining that a mercurian day is twice longer than the mercurian

[1] The temperatures can span the range from about $-180°$C in the night-side up to $180°$C in the day-side of the planet.

[2] The solar flux received by the planet can change by more than a factor of two throughout a mercurian year.

[3] Mercury never reaches distances greater than $28°$ away from the Sun. Due to its small angular distance, the planet is always close to the Sun and then it can be observed only in the morning, before the sunrise, or in the evening, after the sunset. From Earth, Mercury exhibits phases like the Moon and Venus.

year. The axial tilt is almost zero ($\simeq 0.027°$) and it prevents the illumination of the planet poles, leaving them always in relative shadow: craters in these shadow parts could have water-ice or sulphurs.

Mercury has a diameter of about 40% longer and a mass about 4.5 times greater than Moon. Mercury's density can be also used to infer details of its inner structure. Currently, we think that Mercury has a large melted core (42% of the total volume) composed by metallic (70%) and silicate (30%) materials, making the planet one of the densest planets in the solar system after Earth. Mercury has also a stable weak dipolar magnetic field [4]. Its source could be due to a dynamo effects produced by the material circulation in the iron-rich melted core and maintained by the strong tidal effects caused by the planet's high orbital eccentricity. The magnetic field is strong enough to deflect the solar wind around the planet, creating a small but very dynamic magnetosphere. Recent spacecraft explorations have shown a complex interaction of this magnetosphere with the particles and the fields transported by the solar wind. For example, solar wind ions and electrons can be trapped by this magnetosphere and accelerated toward the surface. In contrast, when the magnetic fields carried by the solar wind connect to Mercury's magnetic field, we could have the formation of twisted magnetic flux tubes: some of these structures become open windows on the planet's magnetic shield through which the solar wind particles may enter and directly impact Mercury's surface.

The surface appears similar to the Moon, with the typical geological features such as mare-like plains and cratering which suggest a geological inactivity for billions of years. From the crater density analysis, were found that parts of crust could be older than 3.8 billion years while, other parts with lower densities of craters, may be younger than 1 billion years [5]. Recently, was also found the volcanic origin of the plains [6] but most of the geological history of the planet has to be discovered yet.

One of the main problems in modern Mercury science concerns the formation, sustaining and evolution of the tenuous atmosphere of the planet, called *exosphere*, although the planet is not large enough to retain by gravity a permanent thick atmosphere. Usually, the exosphere is the uppermost layer of the atmosphere of a planet, where the particle density is so low that the particles no longer collide with each other and some are moving fast enough to reach the escape velocity and escape to space. However, for Mercury the exosphere starts at the surface in which occurs many particular processes that feed the exospheric species. In the last 30 years, from the spacecraft and ground bases observations we have observed different species in the planet exosphere, including Hydrogen, Helium, Oxygen, Sodium, Calcium, Potassium and, recently, Magnesium. The relative abundances and dynamic of these species are still badly understood but, from the data collected, many exospheric models devoted to justify the exosphere sustaining and dynamics were proposed. Actually, the model conventionally accepted justifies the exosphere existence and species abundance with the superposition of different *source* and *sink*

mechanisms [7]. In the source mechanisms are considered the processes which deliver new exospheric material to the surface and the mechanisms which release material directly from the surface[4] or with processes such as solar wind particles capture or radiogenic decay. For example, part of the observed abundances of H and He can be explained by solar wind capture or radiogenic decay of heavy elements. On the other hand, when the surface interacts with the solar wind, the solar radiation, other exospheric particles or micrometeoroids different species can be released. The impact of an energetic particles with the surface can release species by physical sputtering (as occurs for a main part of Ca and Mg abundances) or after a chemical reaction (as occurs for Na and OH species). The interaction of the surface with the solar radiation can produce thermal desorption or UV *photon stimulated desorption* (PSD) that could be efficient release processes on the planet dayside for volatile species such as Na and K. Vaporization for impact of micrometeoroids is also an energetic process that can be an efficient source for all species presented in the exosphere.

New exospheric material is delivered to the surface by diffusion, regolith turnover and ion-recycling. Diffusion processes bring new material (Na, K, Ca, ...) to the surface through cracks, rock fragments, voids grains, crystalline lattices or the surface grains. The regolith turnover bring exospheric material mainly by impacts gardening. In the ion-recycling, the part of the exospheric materials is ionized by UV solar photons, trapped and transported to the night-side by the magneto-tail. The ions transported into the night-side surface can be neutralized and absorbed into the surface and then released later during Mercury's day.

The possible sinks for depleting Mercury's exosphere include thermal escape, photoionization and entrainment in the solar wind, surface implantation. Thermal escape is an efficient process for the lighter elements such as H and He. However, thermal escape assisted by solar radiation pressure occurs for sodium and presumably also for potassium: for example, up to 10% of the total sodium production rate is lost by escape during periods of maximum solar radiation pressure. In additional, the neutral atoms in the exosphere can be ionized by the solar photons and carried away by the solar wind and magnetosphere. Removal of material from the exosphere via surface implantation can occur either through adsorption onto surface grains or through chemical interactions, such as those that produce space weathering effects in the regolith. Adsorption is more productive on the night-side, where evaporation is less effective at releasing the material. Adsorption also includes the process of cold-trapping material, such as in shadowed areas at high latitudes, or under outcroppings. In Figure 1 is summarized the life cycles of the exospheric species.

[4]In this class of source mechanisms we consider the release of exospheric material from the surface after the interaction with solar wind particles, solar radiation or accelerated exospheric particles.

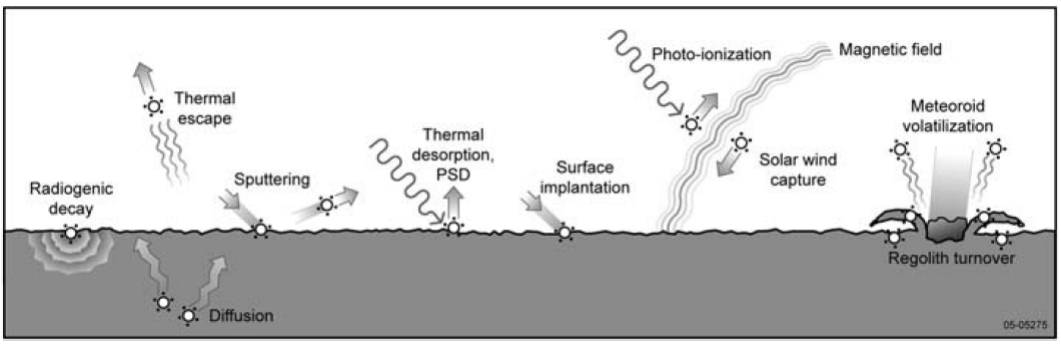

Figure 1. Sources and sinks processes in the Mercury exosphere.

Despite the vast amount of data collected by two space mission and the ground telescopes, the Mercury system still remains a mystery: in fact, a lot of aspects concerning its geology, its interior, its magnetosphere or its exosphere are not completely understood. For this reason, the new mission BepiColombo, which is in an advanced state of development, will be launched toward Mercury and with a highly comprehensive set of instrument and instrument suites it will improve our knowledge of this planet. Among the instruments onboard BepiColombo, the Probing of Hermean Exosphere by Ultraviolet Spectroscopy (PHEBUS) instrument is a double spectrometer working in the Extreme Ultravioley (EUV) and in the Far Ultraviolet (FUV); it will be developed to study the composition, dynamics and formation mechanisms of the Hermean exosphere by using spectroscopy analysis. The data collected by PHEBUS can be correctly interpreted if its radiometric and spectral behaviour is well known.
In this thesis the radiometric aspects of PHEBUS are deeply discussed and an accurate radiometric model of the instrument is developed. In additional to the theoretical model, the PHEBUS calibration activates carried out at the CNR-IFN UOS Padova laboratory are also presented. All activities are focused to determine and experimentally validate the PHEBUS radiometric model by using both an optical sub-system level and an instrument level measurements. In the sub-system level measurements each optical component has been characterized in order to retrieve the instrument efficiency. Instead, with instrument level measurements, the geometric parameters which affect the radiometric response as well as the instrument linear range and its spectral behavior can be experimentally determined. The thesis is organized as follow:
Chapter 1 gives an overview of the BepiColombo mission, describing its payload, its scientific objectives and the mission operations. In this chapter is also described the spectrometer PHEBUS, presenting its scientific objectives and its optical layout.

Chapter 2 is the core of this thesis and it presents the approach adopted for the radiometric modelling of PHEBUS. This chapter presents the radiometric model with a general discussion and shows hoe the results obtained can be applied to PHEBUS.
Chapter 3 are described the optical sub-systems characterizations performed at the CNR-IFN UOS Padova laboratory. The results obtained from this activity are presented and discussed.
Chapter 4 are described the preliminary calibration activities performed on the qualification model of PHEBUS. The optical set-ups developed for these activities are described together the early results obtained.
Chapter 5 are reported the conclusions of this work.

Chapter 1

A new mission to Mercury

From the beginning of the space exploration, only two space missions have explored the Mercury planet: the Mariner 10 [8] and the MESSENGER mission [9, 10].

The first mission, Mariner 10, encountered Mercury three times between the 1974 and 1975 and it carried onboard seven instruments devoted to investigate the planet (see Figure 1.1(a)): an extreme ultraviolet spectrometer, a magnetometer, two twin television telescopes with digital tape recorder, an infrared radiometer, a solar plasma analyzer, a charged particles analyzer , and a radio wave propagation experiment. The primary scientific objectives of the mission were to observe Mercury's (and also Venus) environment, atmosphere, surface, and body characteristics. However, the heliocentric orbit adopted for the three flybys had a period almost exactly twice of Mercury and then the same side of Mercury was observed at each flyby: at the end of the mission, only about 45% of the surface was observed and mapped taking over 2.800 photos (Figure 1.1(b)). Despite this, the mission contributed enormously to our understanding of the planet taking a lot of data that would be impossible to retrieve through ground-based observations: for example Mariner 10 discovered the Mercury tenuous atmosphere, consisting primarily of hydrogen, helium and oxygen [11, 12] as well as a magnetic field [13] and a large iron-rich core; its radiometer readings suggested that Mercury has a night-time temperature of $-183\,^{\circ}\mathrm{C}$ and maximum daytime temperatures of 187° [14].

In 2004, about 30 years later the first Mercury flyby of the Mariner 10, a second mission to Mercury was launched. The MESSENGER (MErcury Surface, Space ENvironment, GEochemistry and Ranging) mission main objectives are to complete and complement the observations made by Mariner 10, explore the nature of Mercury exosphere and magnetosphere, characterize the chemical composition of the surface, study the geological history of the planet, determine the size and state of the planet core. In order to address the goals expected, the MESSENGER mission is equipped by eight instruments: the Mercury Dual Imaging System (MDIS), the Gamma-Ray

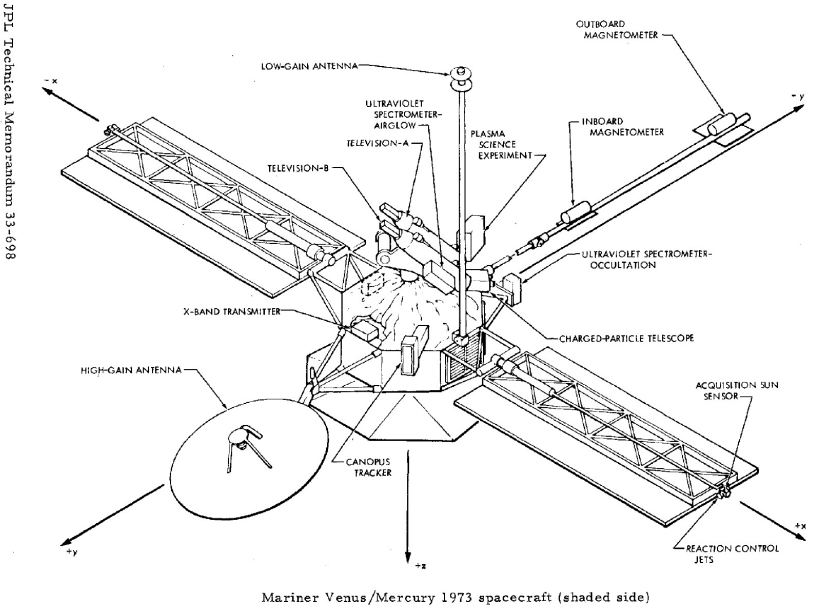

(a)

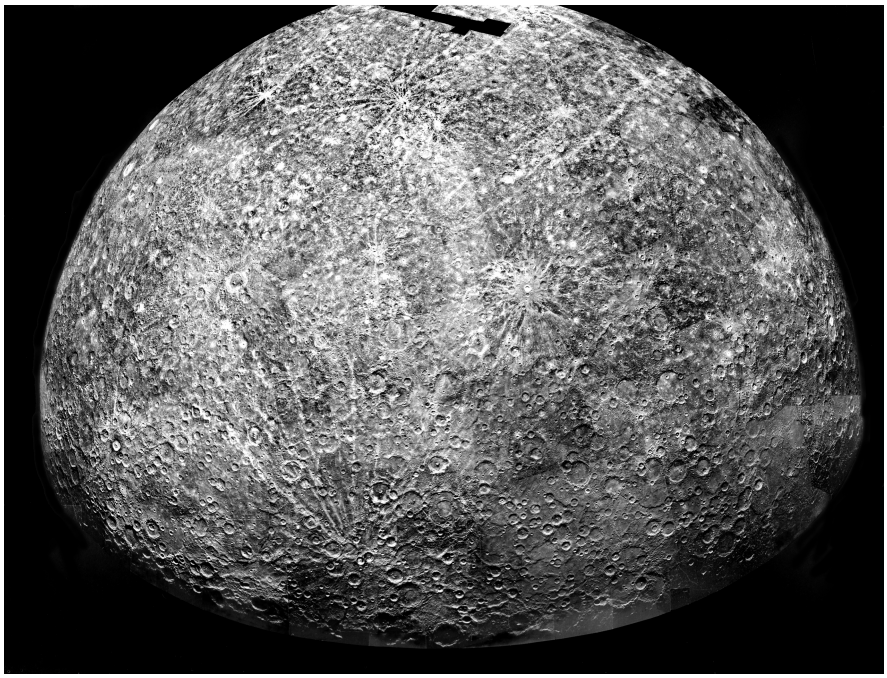

(b)

Figure 1.1. The scheme of the Mariner 10 spacecraft (a) and the first map of the Mercury surface (b) obtained from the 2800 photos taken during the three flybys.

and Neutron Spectrometer (GRNS), the X-Ray Spectrometer (XRS), the Magnetometer (MAG), the Mercury Laser Altimeter (MLA), the Mercury Atmospheric and Surface Composition Spectrometer (MASCS), and the Energetic Particle and Plasma Spectrometer (EPPS). After three flybys, the spacecraft was inserted in the Mercury orbit on March 18, 2011 and, actually, the mission is still in operation. Up to now, MESSENGER has successfully completed the global map of the planet with a resolution up to 250 m/pixel [15], it has performed more detailed studies about its geology, evolution history and volcanism [16, 17, 18, 19], it has studied with more detail the Mercury magnetic field components [4], it has made spectroscopic studies of the multitude of species in the surface [20] and in its exosphere, including, for the first time, Magnesium [21, 22].

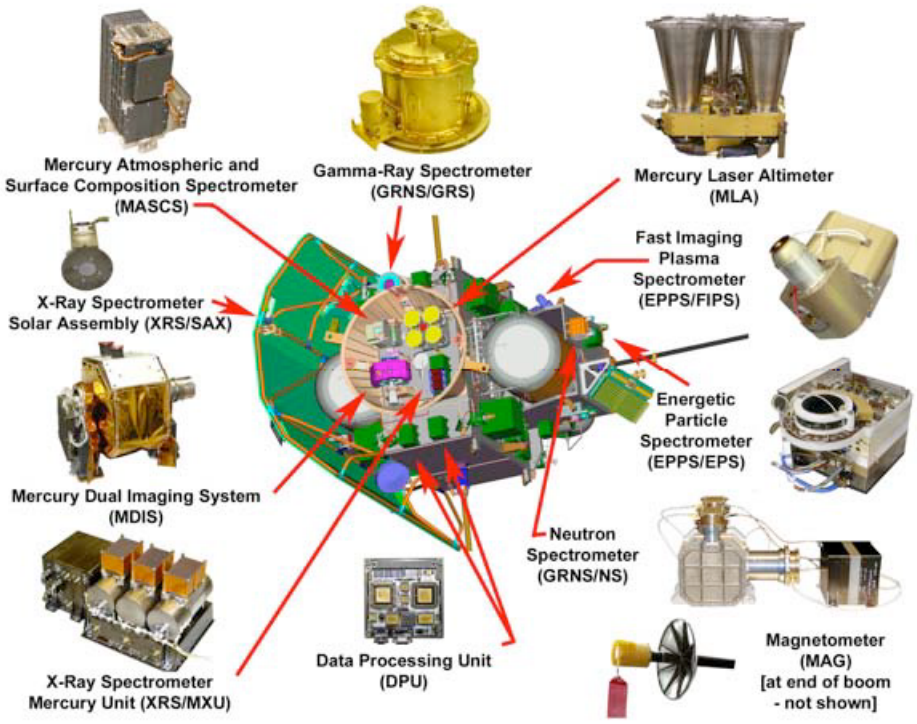

Figure 1.2. The NASA MESSENGER spacecraft with its payload.

With this background, a new third mission, the ESA/JAXA BepiColombo mission [23, 24], is under development and it will be launched on July 2016. The mission is composed by two dedicated spacecraft that will study the planet and its environment with a wide set of instruments. Its scientific objectives are similar to those of MESSENGER mission but they will be achieved with an high synergy between the two missions in order to maximize as much as possible the scientific returns: during

the mission, MESSENGER has provided a lot of valuable discoveries about Mercury and its environment that will be used as background by the BepiColombo mission in tuning its observations to the most important targets. In the first section of this chapter the BepiColombo mission, its scientific objectives and its payload are synthetically discussed; in the second section the PHEBUS instrument, the EUV/FUV spectrometer that will be on board of Bepicolombo, is widely presented.

1.1 BepiColombo: mission overview and scientific goals

BepiColombo is a dual spacecraft mission to Mercury carried out jointly between ESA (European Space Agency) and JAXA (Japanese Aerospace Exploration Agency). The mission will address a comprehensive set of scientific questions in order to gain knowledge about Mercury planet, its evolution history and its surrounding environment. Both spacecraft will be launched together in July 2016 [24] and they will carry a large number of "state of the art" scientific instruments. One spacecraft, the *Mercury Planetary Orbiter* (MPO), is led by ESA and its payload comprises eleven experiments and instrument suites. The MPO will focus on a global characterization of Mercury through the investigation of its interior, surface, exosphere and magnetosphere. The second spacecraft, the *Mercury Magnetosphere Orbiter* (MMO), is led by JAXA and will carry five experiments or instrument suites to study the environment around the planet including its exosphere, its magnetosphere, and the interaction processes with the solar wind and the planet itself.

In additional to the two orbiters, the BepiColombo mission has two additional segments that are very important during the interplanetary journey: the *Mercury Transfer Module* (MTM) and the *the MMO Sunshield and Interface Structure* (MOSIF). During the interplanetary journey, the two orbiters, the MTM and the MOSIF module are connected together, forming the *Mercury Composite Spacecraft* (MCS) shown in Figure 1.3. The MTM provides the thrust required to reach Mercury and the large amount of power required by the solar electric propulsion system. The MOSIF module provides the interface structure between the MPO and the MMO and protects the MMO from the Sun radiation until it has reached its operational orbit.

The mission has been named in honor of Giuseppe (Bepi) Colombo (1920-1984), who was a brilliant Italian mathematician, who made many contributions to planetary research, celestial mechanics, including the development of new space flight concepts. He is well-known for explaining that Mercury rotates three times about its axis while it completes two orbits around the Sun. He also proposed to NASA the interplanetary trajectory for Mariner 10 using gravity assist that allowed even

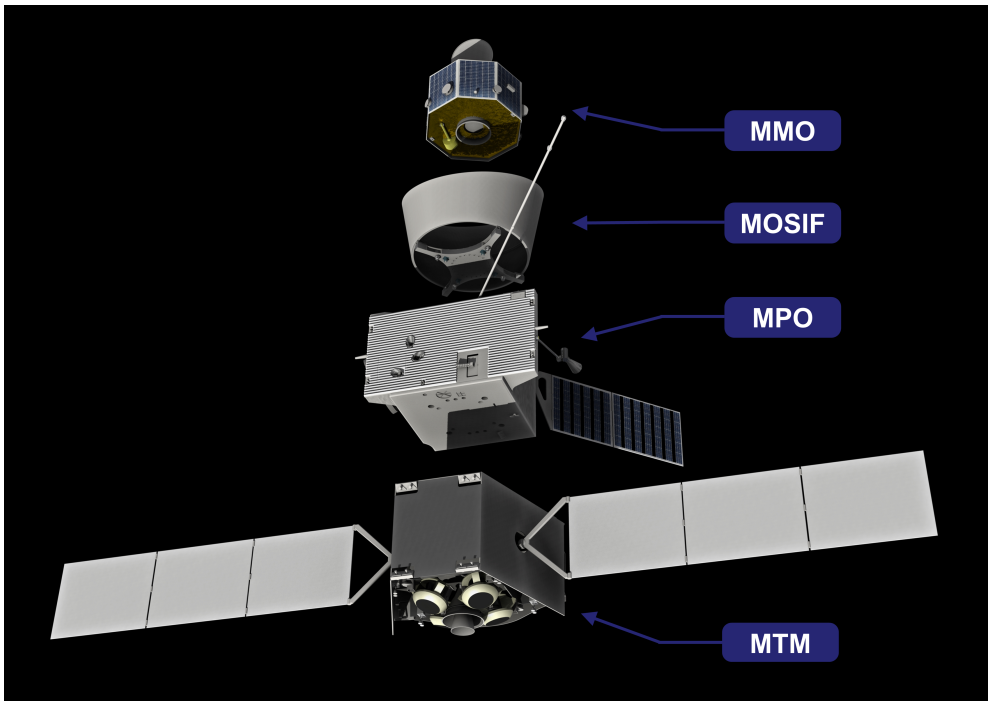

Figure 1.3. Exploded view of the BepiColombo cruise configuration named Mercury Composite Spacecraft (MCS).

three Mercury flybys (1974-1975).

1.1.1 Scientific objectives

BepiColombo is a planetary Cornerstone mission of ESA's *Cosmic Vision Program*, and is devoted to the thorough exploration of Mercury and its environment. The scientific objectives that BepiColombo mission will try to address with its payload can be summarized with the following points:

- Study and understand the Mercury formation and geological history, its interior structure and composition; these information are important because they can help us to better understand the composition of the primitive solar nebula and the formation of our planetary system.

- Study the actual Mercury surface: understand its composition, its geology and if it is volcanically or tectonically active today.

- Study its intrinsic magnetic field and its magnetosphere; understand why a small planet as Mercury has a magnetic field and other bigger planets like Venus, Mars and the Moon don't have it. Understand how the magnetic

field interacts with the solar wind and if Mercury is characterized by features reminiscent of the aurorae, radiation belts and magnetospheric sub-storms observed at Earth.

- The exosphere composition and dynamics: what are the formation mechanisms of the exosphere?

- Research of sulphur or water ice inside the permanently shadowed craters of the polar regions.

- Since the advance of Mercury's perihelion was explained in terms of space-time curvature, we can take advantage of the proximity of the Sun to test general relativity with improved accuracy.

All these scientific objectives will be addressed in synergy with the MESSENGER mission which is still collecting important data: the "MESSENGER experience" will help us to choose the most interesting targets on Mercury and will be a needful source of information for the Bepicolombo's observations.

1.1.2 The BepiColombo payloads

The scientific goals expected from BepiColombbo mission will be addressed by a highly comprehensive set of instruments and instrument suites. In the following only a short summary of the MPO and MMO instruments are given: each instrument is described in detail in many specific articles such as the references of [23].

The MPO payload:

- The *BepiColombo* Laser Altimeter (BELA) will measure and characterize the topography and surface morphology of Mercury. BELA will provide absolute topographic height and position with respect to the Mercury centered coordinate system useful to create a digital terrain model that allows, together the data collected by others instruments, a quantitatively exploration of the geology, the tectonics and the age of the planet's surface. The returned laser signal can be also used to measure the local surface roughness and albedo.

- The *Italian Spring Accelerometer* (ISA), is a three-axis high-sensitivity accelerometer. It will be devoted to study the global gravity of Mercury field, its time variations due to solar tides, the local gravity anomalies, the rotation state of Mercury and the motion of Mercury's center of mass. Furthermore, the instrument will also perform experiments devoted to testing Einstein's theory of General Relativity reaching an unprecedented level of accuracy.

- The *MPO Magnetometer* (MPO/MAG) is an experiment consisting of a dual fluxgate magnetometer system that can measure 3D magnetic fields from DC up to 128 Hz within ±2048 nT with a digital resolution better than 60 pT; magnetic field contamination from the electronic systems of the spacecraft is avoided performing differential measurements from two sensors, one inboard and one outboard of the spacecraft. The MPO/MAG will measure the planet magnetic field in order to understand it and its source in great detail. This will help us to understand the origin, evolution and current state of the planetary interior. Furthermore, the activity of MPO/MAG will be supported by similar measurements made by the MMO Magnetometer, in order to distinguish the effects of the magnetospheric currents on the MPO measurements. In additional, MPO/MAG will help us to study the interaction of the solar wind with Mercury's magnetic field and the planet itself. This interaction will lead to the formation of the global magnetospheric current systems that are highly dynamic.

- The *MErcury Radiometer and Thermal Infrared Spectrometer* (MERTIS) is an IR-imaging spectrometer which will provide detailed information about the mineralogical composition of Mercury's surface by mapping the emittance with a spatial resolution of 500 m and a high-spectral resolution: MERTIS will cover a wavelength range from 7 to 14 μm with a spectral resolution up to 90 nm. In addition MERTIS will be able to measure thermo-physical properties of the surface like thermal inertia and surface texture.

- The *Mercury Gamma-Ray and Neutron Spectrometer* (MGNS) will measure the elemental surface and subsurface composition by measuring the nuclear lines of major soil-composing elements, the leakage flux of neutrons and the lines of natural radioactive elements. It will also determine the regional distribution of volatile depositions on the polar areas of Mercury which are permanently shadowed from the Sun, and provide a map of column density of these depositions with the accuracy of 0.1 g cm^{-2} and with a surface resolution of about 400 km.

- The *Mercury Imaging X-ray Spectrometer* (MIXS) is a dual channel spectrometer designed to analyze the surface atomic composition using the X-ray fluorescence (XRF) analysis. The primary scientific goal of MIXS is to produce with a high spatial resolution the global elemental abundance maps of key rock-forming elements with an accuracy of $10 - 20\%$. Furthermore, the instrument can confirm if the auroral zone, where energetic particles interact with the surface, is an intense source of continuum and line X-rays. The interpretation of the MIXS measurements requires the knowledge of the solar X-ray flux monitored by the SIXS experiment.

- The *Mercury Orbiter Radio-science Experiment* (MORE) will address scientific goals in geodesy, geophysics and fundamental physics. It will help to determine the gravity field of Mercury as well as the size and physical state of its core. It will provide crucial experimental data to understand the planet's internal structure and it will test theories of gravity with unprecedented accuracy. MORE will also measure the gravitational oblateness of the Sun. Finally, MORE will also contribute to the determination of Mercury's obliquity (i.e. the obliquity of the equator with respect to the orbital plane) and the amplitude of its 88-day physical librations in longitude: these two quantities, together with the coefficients of the second-degree harmonics of the gravity field, will indicate if the Mercury has a molten core and, eventually, it will help to determine the radius of this molten core.

- The *Probing of Hermean Exosphere by Ultraviolet Spectroscopy* (PHEBUS) instrument is a dual-channel EUV/FUV spectrometer devoted to characterize the structure, composition and dynamics of Mercury's exosphere and to understand the coupled surface-exosphere-magnetosphere system. It will be described with more detail in Section 1.2.

- The *Search for Exospheric Refilling and Emitted Natural Abundances* (SERENA) experiment will provide information about the global surface - exosphere - magnetosphere system and its interaction with the solar wind. The experiment consists of four sensors that can be operated individually: the Emitted Low-Energy Neutral Atoms (ELENA) measures energetic neutral particles (above 50 eV) escaping from the surface of Mercury, the Start from a Rotating Field Mass Spectrometer (STROFIO) that is a neutral particle spectrometer monitoring the cold exospheric gas composition with a high mass resolution, the Miniature Ion Precipitation Analyzer (MIPA) that is an ion spectrometer for 10 eV-15 keV energies measuring ions that precipitate towards the surface, and the Planetary Ion Camera (PICAM) that is an ion mass spectrometer with 1 eV-3 keV energies range. SERENA and PHEBUS observations are both complementary and highly supportive to each other: for example PHEBUS will produce global mapping of the exosphere and SERENA will measure in situ both neutrals and ions.

- The *Spectrometer and Imagers for MPO BepiColombo Integrated Observatory System* (SIMBIO-SYS) instrument suite is an integrated package for the imaging and spectroscopic investigations of the Mercury's surface. It consists of a Stereo Channel (STC) which will provide the global color coverage of the surface in full stereo at 50 m/pixel resolution, an High spatial Resolution Imaging Channel (HRIC) which it will characterize special surface targets with high-resolution images up to about 5 m/pixel in four different bands, and a Visible

Infrared Hyperspectral Imager Channel (VIHI), which is a hyperspectral imager in the visible and near-infrared range that will map the planet in order to provide the global mineralogical composition of the surface. The science goals of SIMBIO-SYS are to characterize the surface geology, volcanism, global tectonics, surface age, surface composition and geophysics of Mercury. It incorporates capabilities to perform medium-spatial resolution global mapping in stereo and color imaging using two pan-chromatic and three broad-band filters, respectively, as well as high-spatial resolution imaging with pan-chromatic and three broad-band filters and imaging spectroscopy in the spectral range $400 - 2000\,\mathrm{nm}$.

- The *Solar Intensity X-ray and particle Spectrometer* (SIXS) experiment will monitor solar X-rays (SIXS-X) in the spectral range $1 - 20\,\mathrm{keV}$ with $300\,\mathrm{eV}$ of resolution and the energetic particles (SIXS-P). The X-ray data are mandatory for a fluorescence analysis of MIXS spectra. Furthermore, due to the high variability of the intensity and energy spectrum of both X-rays and energetic particles, simultaneous operations of SIXS and MIXS is required. Moreover, the observations of solar X-rays and energetic particles are important for a large number of others investigations: they include exospheric studies with SERENA and PHEBUS on MPO and most studies with the MMO payload. In additional, it will give important information about the physics of the Sun and, in particular, it will monitor the solar X-ray corona and solar flares in order to determine their temporal variability and spectral classification.

The MMO payload:

- The main objective of the Mercury Dust Monitor (MDM) is to investigate the dust environment in the region of the solar system between 0.31 to 0.47 AU. For example, the impact of micro-meteoroids may contribute significantly as one of the source processes of the planet's tenuous atmosphere and the dust environment around the planet. This instrument is designed in order to detect impact momentum, the characteristic and the density of the dust. The viewing direction almost covers a half-sphere.

- The primary objective of the MMO Magnetometer (MMO/MAG) is to collect magnetic field measurements in synergy with MPO/MAG. The instrument is designed to measure magnetic fields with an accuracy of about $10\,\mathrm{pT}$, a dynamic range of $\pm 2048\,\mathrm{nT}$ and a time resolution up to $128\,\mathrm{Hz}$.

- The *Mercury Plasma/Particle Experiment* (MPPE) is a comprehensive instrument package for plasma, high energy particle and energetic neutral atoms

measurements. It consists of seven sensors: two Mercury Electron Analyzers (MEA1 and MEA2), a Mercury Ion Analyzer (MIA), a Mercury mass Spectrum Analyzer (MSA), an High Energy Particle instrument for electrons (HEP-ele), an High Energy Particle instrument for ions (HEP-ion) and an Energetic Neutrals Analyzer (ENA). The instruments will provide useful information about the plasma and particle environment around the planet.

- The *Mercury Sodium Atmospheric Spectral Imager* (MSASI) is a high-dispersion visible spectrometer working in the spectral range around sodium D2 emission (589 nm). A Fabry-Perot etalon is used to achieve a compact design. A one degree-of-freedom scanning mirror is employed to obtain full-disk images of the planet. This instrument will observe the Sodium in the planet exosphere and it will collect precious information about its dynamic.

- The *Plasma Wave Investigation* (PWI) is designed and developed in collaboration between Japanese and European scientists. PWI onboard the MMO spacecraft will provide the first electric fields, plasma waves, and radio waves measurements from the Mercury plasma environment. It will give important information regarding energy exchange processes in the small magnetosphere where the role of micro-physics is more visible than anywhere else. The PWI will observe both waveforms and frequency spectra in the frequency range from DC to 10 MHz for the electric field and from 0.1 Hz to 640 kHz for the magnetic field.

1.1.3 Mission operations

According to the current program [24], the BepiColombo dual spacecraft will be launched by an Ariane 5 from the Spaceport in French Guiana, on July 2016. During the journey towards Mercury, BepiColombo will make a first gravity assist with the Earth about one year after launch in order to deflected its trajectory towards Venus. Two consecutive Venus flybys in a 1:1 resonance will reduce the BepiColombo orbit perihelion to Mercury distance and a sequence of additional five Mercury flybys will lower the relative velocity of the spacecraft. Four final thrust arcs will further reduce the relative velocity to the point where Mercury will weakly capture the spacecraft on 1 January 2024, after about 7.5 years of cruise, without an orbit insertion maneuver being required. During this phase, the MTM will be separated from the spacecraft stack. After the insertion in an initial orbit of approximately 490×178000 km, a series of maneuvers will be performed in order to reach the MMO operation orbit where the two modules will be separated. The MPO with the MOSIF still attached performs another two maneuvers for pericentre raising and apocentre lowering, and then it will separate the MOSIF in a safe direction while the MPO will descend to

its own mission orbit. In the scientific operation phase, the MMO will travel around Mercury in a polar orbit with a period of approximately 9.3 hours, a perihermion of 400 km and an apohermion of 11824 km. The orbit will be coplanar with that of the MPO, which will have an orbital period of around 2.3 hours with a perihermion of 400 km and an apohermion of 1508 km. A sketch of the orbits foreseen during the scientific phase is shown in Figure 1.4.

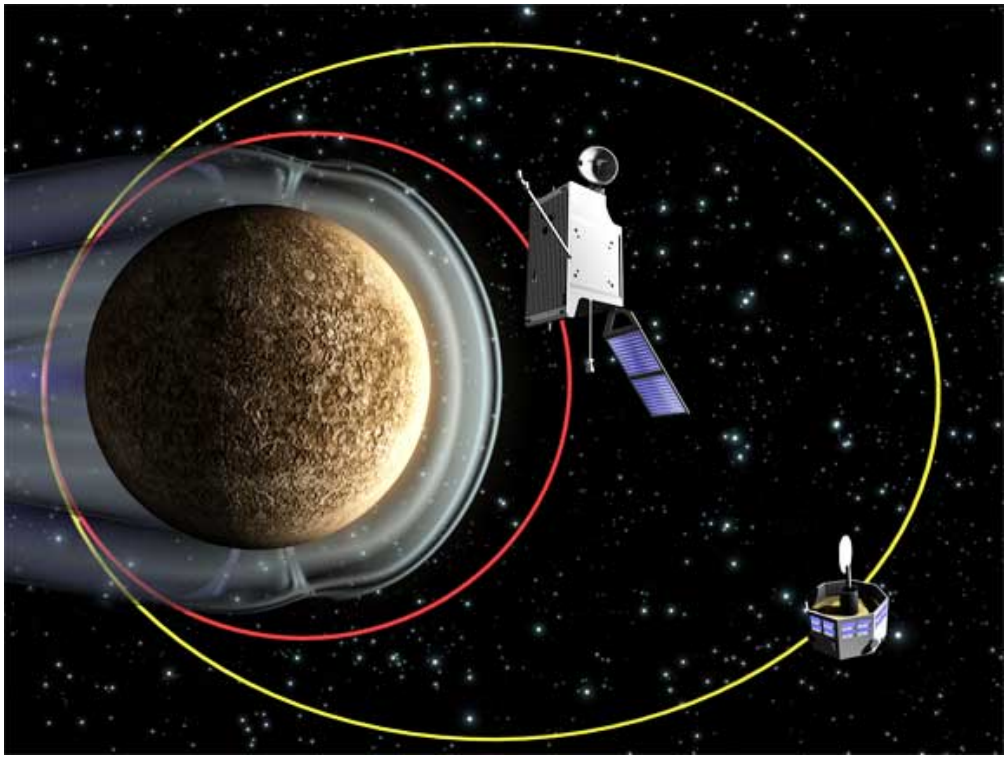

Figure 1.4. BepiColombo spacecraft in Mercury orbit: MMO will have a polar orbit with a period of approximately 9.3 hours, a perihermion of 400 km and an apohermion of 11824 km while the MPO will have an orbital period of about 2.3 hours with a perihermion of 400 km and an apohermion of 1508 km. The two orbits will be coplanar.

1.2 The PHEBUS instrument

Probing of Hermean Exosphere By Ultraviolet Spectroscopy (PHEBUS) is a double spectrometer that will be onboard of ESA BepiColombo mission (see Figure 1.5). It is basically composed by two channels, one devoted to the EUV range from 55 nm to 155 nm and the other devoted to the FUV range from 145 nm to 315 nm [1]. Two additional lines at 404.4 nm (Calcium) and 422.8 nm (Potassium) are also monitored

with a dedicated NUV path. This instrument is developed with an international cooperation of four countries: French which has the leadership of the instrument, Russia which has the responsibility of the scanning system, Japan which has the responsibility of the EUV/FUV detectors and Italy which has the responsibility of the ground calibrations.

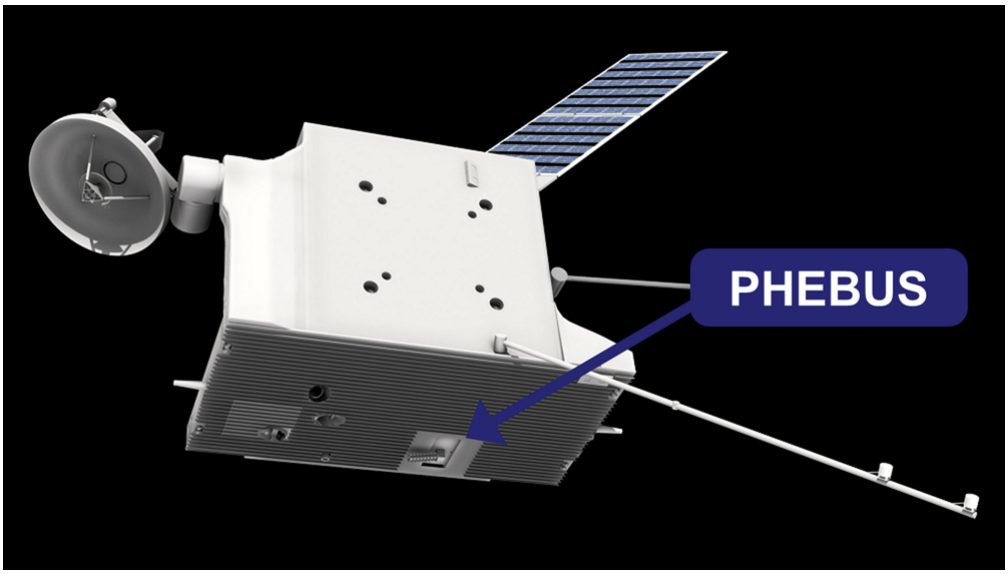

Figure 1.5. The position of PHEBUS in the BepiColombo MPO. The instrument is collocated in the backside of the orbiter, in the middle of the radiator. This position allows to point the field of view of the instrument in any direction along the orbital plane.

1.2.1 Instrument concept

The optical configuration of PHEBUS has been designed with a minimum of reflections in order to maximize the total instrument efficiency. In Figure 1.6 is reported a 2D-optical layout of PHEBUS whereas in Figure 1.7 is reported a 3D-illustration of its optical and mechanical design.

The structure of the instrument can be divided into two independent parts. The first part is the *collecting part* and it is composed by a stray-light rejection baffle, an off-axis parabolic entrance mirror and the entrance slit: the light coming from the exit diaphragm of the baffle is collected by the entrance mirror and it is focused on the entrance slit. An additional movable mechanism, named *scanning system*, allows the rotation of the baffle and the mirror around the optical axis of the instrument and traversing the entrance slit: with this movable capability, the instrument can scan the Mercury's exosphere during the observations and it can also move its gaze to the

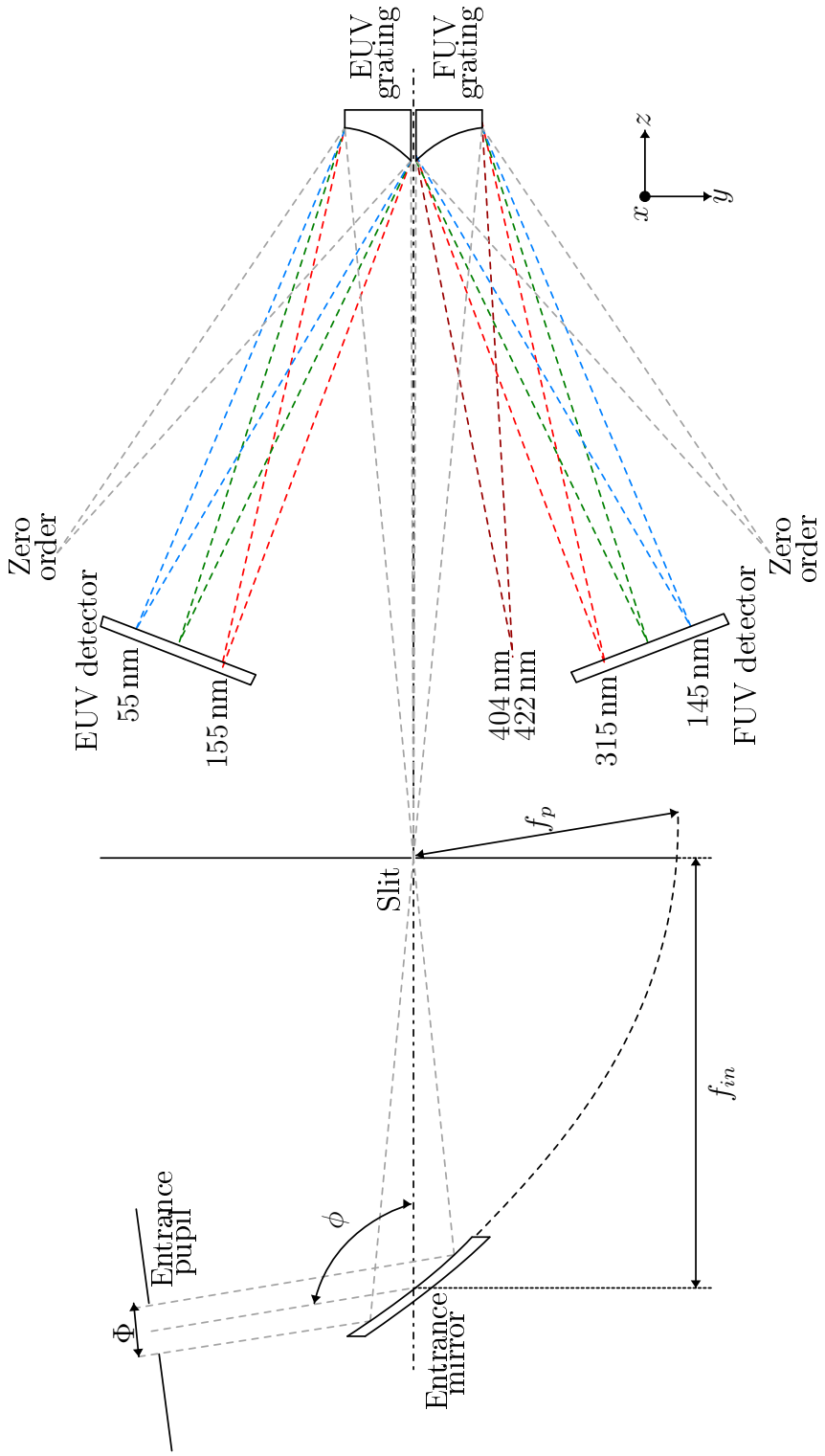

Figure 1.6. 2D representation of the optical layout of PHEBUS. The entrance working angle ϕ of the spectrometer is 100°, the entrance pupil diameter Φ is 25.4 mm and the working focal length of the entrance mirror f_{in} is 170 mm. In the image is also shown the total parabolic shape with focal length $f_p = 70.24$ mm of the entrance parabolic mirror.

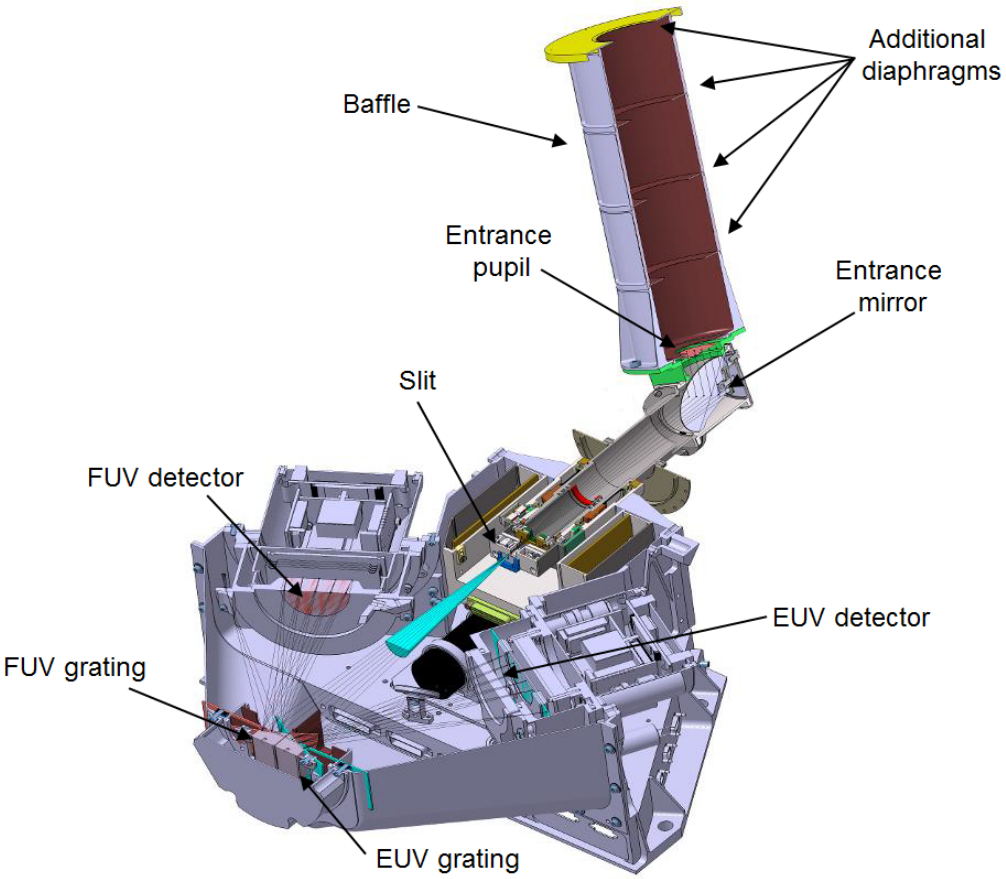

Figure 1.7. 3D representation of the optical and mechanical layout of PHEBUS. The light coming from the baffle is collected by the entrance mirror and focused on the entrance slit which is the spectrometer input. The spectrometer is composed by two gratings, one for the EUV range and the other for the FUV range. The spectrum is collected by two Micro-Channels Plate (MCP) detectors with a Resistive Anode Encoder (RAE).

stars for periodic in-flight calibrations. In fact, the instrument is independent to the spacecraft from an observation point of view, avoiding spacecraft slew for specific pointing request. The baffle of the instrument has the important task to protect the instrument entrance from dangerous direct light coming from bright sources, like the Mercury surface on the day side, placed outside of the defined guard angle ($\simeq 8°$). However, the sources place outside the guard angle illuminate the upper inner part of the baffle with a stray-light risk due to multiple reflections and diffusion on the internal surface. In order to perform exospheric observations as close as the guard angle value from the Mercury illuminate surface, the inner part of the baffle must to have an attenuation as much as possible (at least 10^6) and a very good inner surfaces quality; an additional improvement of the stray-light attenuation is achieved with a system of four diaphragms as shown in Figure 1.8. The exit diaphragm of the baffle has a diameter of $\Phi = 25.4\,\text{mm}$ and it is the entrance pupil of the instrument.

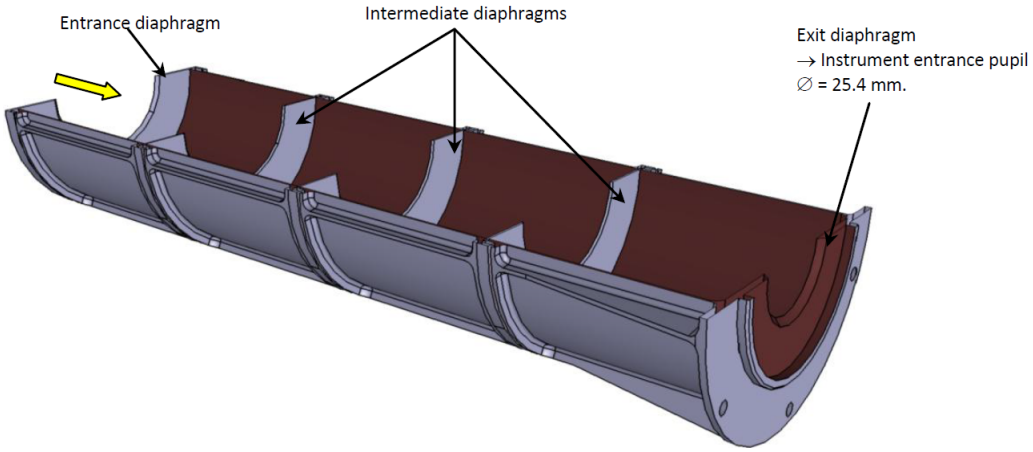

Figure 1.8. 3D mechanical layout of the PHEBUS baffle. Geometric characteristics of the baffle, such as the length, the number of diaphragms and their dimensions are calculated according to the stray light rejection specifications. The inner part of the baffle is black coated to avoid light reflection. The baffle has a rejection angle of 8.26° and an attenuation higher than 10^6.

The entrance mirror is an off-axis paraboloid calculated in order to have an effective focal length of 170 mm and a folding angle ϕ of 100°; the substrate is obtained using sintered Silicon Carbide (SiC) on top of which an optical SiC reflective coating is deposited by chemical vapor deposition process. The optical surface of the mirror is super-polished (the roughness is about 0.5 nm RMS) in order to avoid as much as possible the stray-light inside the instrument. The figure shape error required is lower than 200 nm RMS at 633 nm in order to limit the stars images size in the focal plane during the in-flight calibrations.
The slit is accommodated at the focal plane of the entrance mirror, and it defines

the Field of View (FoV) of the instrument during exospheric observations and it influences also the instrument spectral resolution. Considering the sketch of the

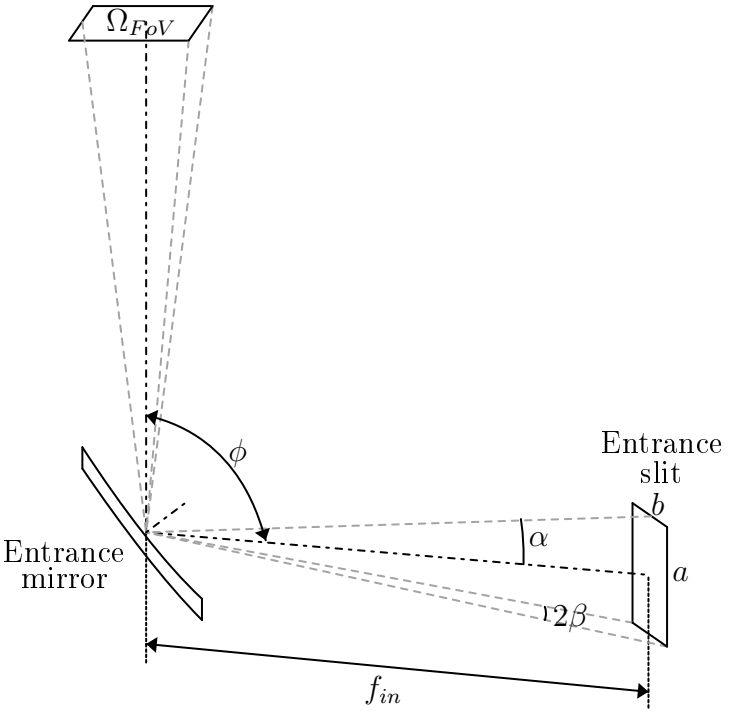

Figure 1.9. Sketch of the collecting part geometry of PHEBUS useful for the Field of View computation. The slit dimensions $a \times b$ are $5.667 \times 0.283\,\mathrm{mm}^2$ and the entrance mirror focal length f_{in} is 170 mm. The folding angle ϕ is 100°.

collecting part of PHEBUS reported in Figure 1.9, we can determine the FoV of the instrument. Considering the focal length of the entrance mirror and the dimension of the entrance slit ($a = 5.667\,\mathrm{mm}$, $b = 0.283\,\mathrm{mm}$), with the paraxial approximation we have

$$\alpha \simeq \frac{a}{2f_{in}} = 0.95°$$
$$\beta \simeq \frac{b}{2f_{in}} = 0.048°$$

and

$$\Omega_{FoV} = 2\alpha\, 2\beta \simeq \frac{ab}{f_{in}^2} = 0.18\,\mathrm{deg}^2$$

obtaining a Field of View of about $2° \times 0.1°$. Experimental measurements of the Field of View were performed on the PHEBUS QM [25]. It was found that the FoV computed with the paraxial approximation contains between 75% and 82% of the

energy, continuously varying as a function of the scan angle. The total energy is contained in a FoV of about $2.3° \times 0.4°$ [25]. This variation can be attributed to the aberrations and stray light introduced by the entrance mirror.
In the star observations performed during periodic in-flight calibrations the stars images size are bigger than the slit size due to the entrance mirror aberrations. However, in this phase the total flux collected from a star is very important for the success of the calibration. For this reason, the total flux collected by the instrument is maximized by removing the entrance slit. The dimension of the window when the entrance slit is removed is $9 \times 4.2\,\mathrm{mm}^2$ [26]. With the paraxial approximation, when the slit is removed we have

$$\alpha' \simeq \frac{a'}{2f_{in}} = 1.52°$$
$$\beta' \simeq \frac{b'}{2f_{in}} = 0.71°$$

and

$$\Omega_{FoV} = 2\alpha'\,2\beta' \simeq \frac{a'b'}{f_{in}^2} = 4.3\,\mathrm{deg}^2$$

Finally, to protect the detectors from occasional excessive illumination, the optical path can be blocked by a shutter located in the proximity of the slit. The shutter is activated by an electromagnetic actuator either in automatic or manual mode. In the automatic mode two photo-diodes are located before the shutter and they monitor the intensity of the incoming light, closing the shutter when a pre-selected threshold is achieved.

The second part of the instrument, simply called *spectrometer part*, starts from the entrance slit and it is composed by two aberration corrected holographic gratings, one for the FUV channel and the other for the EUV channel, and the detectors. The FUV grating has a mean grooves density of $\simeq 1600\,\mathrm{grooves/mm}$ while the EUV grating has $\simeq 2700\,\mathrm{grooves/mm}$. They are composed by an aluminum substrate in which the groove profile is obtained by laminar ion-etched optimized for the respective spectral range and coated by a platinum reflective film; their radius of curvature is 170 mm and their active area size is 42 mm by 15 mm. The required spectral resolution is 1 nm for EUV and 1.5 nm for FUV. These values were compared with the results of the optical design optimization: the Full Width at Half Maximum (FWHM) band is about 0.5 nm for the EUV range, and 0.8 nm on FUV. Furthermore, the Full Width at 1% of maximum (FW1%) band is about 0.9 nm for the EUV range, and 1.5 nm for the FUV range (these calculated values do not include any spreading effects due to scattering by gratings).
The spectrum detection is based on the photon counting method and is done using a 5-stage Micro-Channel Plate (MCP) detectors with Resistive Anode Encoder (RAE) [27, 28]. Photocathodes are CsI for the EUV range, and CsTe sealed with a

MgF_2 protective window for the FUV range. For the EUV detector, the CsI photocathode efficiency is very sensitive to the moisture and air ambient and then also it requires a protective window; however, the EUV radiation does not propagate through windows below to 115 nm. The EUV detector is then sealed with a movable MgF_2 window, which allows to keep the required vacuum (lower than 10^{-2} mbar) with a dedicated pumping system. This pumping system will be removed as late as possible before the launch. When the instrument is in vacuum conditions (during experimental calibrations activities or when the instrument is in the space) an actuator will open the movable window for collect the EUV radiation. The size of the detectors active area is $40 \times 25\,mm^2$ equivalent to a matrix of 1024×512 virtual pixels (spectral $\times$ spatial). Thanks to the very high sensitivity of the MCP+RAE detectors, the instrument is only devoted to the detection of very faint emissions. Furthermore, Calcium and Potassium lines are selected by the FUV grating. These extra visible lines are monitored using photomultipliers (PM) with bialkali photocathode used in photon counting mode. However, due to the size of the FUV detector, the two PMs cannot be directly accommodated at the focal point of the two wavelengths of interest: as solution, a double aperture deviation prism and two spherical mirrors take the light at 404.4 nm and 422.8 nm in front of the FUV detector and deviate it towards the PMs.

1.2.2 Scientific goals

PHEBUS is a spectrometer that will observe the Mercury exosphere in the EUV and FUV range and it will be devoted to detect and analyze the faint emission lines of this target. The dynamic range of the expected emissions is very height: some species can be easily measured with short integration time less than 1 min but other species are very faint and they require an integration time even more than 1 h. Moreover, some species are mixed with other emission lines: for example, Xe I with S I in the EUV range, and OH with Al I in the FUV range. They can be estimated by subtraction if the other line is already known with others methods. Considering the optical layout of the instrument, a mean detection limit can be estimated: about 0.1 R for the EUV channel, and about 0.2 R for the FUV channel. A list of the emissions detectable by PHEBUS is reported in Table 1.1.

From the species measurements, a lot of questions concerning to the composition and vertical structure, the dynamics and the formation mechanisms of the Mercury exosphere can be successfully addressed. The scan capabilities of PHEBUS allow a vertical exploration of the exosphere, providing a map of the species variation with the altitude and information about composition, temperature, release processes and vertical dynamics (Objective 1); in addition, the variation of the species from the day to night side can be followed and analyzed (Objective 2). During these observations, new species never detected before are expected [29], including metallic species (Si,

Detection Difficulty	EUV channel	FUV channel
Easy (≤ 1 min)	He I, CO, O I, H I, C I, N I	Mg I, Si I, Na I, C I, Fe I, S I, Al I, CO, H I, Ni I, Mg II, O I
Medium (≤ 10 min)	S I, S II, H_2, C II	Ca I ,H_2 , Li I
Hard (≤ 1 h)	Xe I, Ne I	Fe II, OH
Very hard(several hours)	Kr I, Ar I	Al II, K I, Xe I, Ca I

Table 1.1. Classification of the expected species and their detection difficulty as reported in [1]. For a more detailed list, with also the wavelengths and the line intensities, see [2].

Fe, etc.), atoms (C, N, S, etc.), molecules and radicals (H_2O, H_2, OH, CO), noble gases (Ar, Ne), ions (He+, Na+, Mg+, etc.), in addition to the already detected species (Na, K, Mg, Ca, O, H, He) [11, 12, 21, 22, 30]. From the detection of species produced by different release mechanisms (e.g. Sodium by thermal desorption and PSD, Calcium by sputtering), a map of the ratios between two specific species used as a signature of a certain release mechanism can be obtained together the characterization of systematic and/or local (in space and/or time) deviations signing this release mechanism (Objective 3).
In EUV and FUV ranges the ions can be mapped as function of time and space and compered with the neutral species obtaining a characterization of the dynamic of the exosphere (Objective 4). Moreover, the ions and neutral species observed in the magnetosphere, synergistically with MMO measurements, should allow to follow planetary ions from their formation regions in the exosphere, through the magnetosphere, until their escape or re-injection into the exospheric system through the magneto-tail (Objective 5). From the measurements of the escape rates of the species, together the data collected by other geochemical instruments (e.g. the X-ray spectrometer), the regolith composition of the surface can be characterized. The comparison between escape rates and exosphere density for the species detected gives information about the residence time of this species in the regolith-exosphere system and, more generally, on the geochemical cycles and source-sink balance (Objective 6).
Finally, as usually occur in an interplanetary mission, some observations on the dark side of Mercury will be dedicated to the water-ice and sulfurs research which may be present in some craters at high latitude (Objective 7). In fact, some craters close to the poles never receive direct sunlight and water-ice coming from comets impacting Mercury may have accumulated there. The principle of the detection is easy. On the night side of the planet, the main source of Lyman-α radiation at 121.6 nm is caused by the scattering of solar photons by hydrogen atoms in the interplanetary medium. This scattering creates a glow at 121.6 nm which illuminates the night side

of Mercury. At high ecliptic latitudes, the Lyman-α emission is about 500 R and varies by one or two hundred Rayleigh[1] according to the solar cycle. If water-ice is present on the surface of the planet, it will be detected by variations of the surface albedo at 121.6 nm. Assuming that the mean EUV albedo of Mercury is close to the value of the EUV albedo of the Moon, that is around 4%, we should get a signal around 20 R. For water-ice, the albedo at 121.6 nm is close to 2% with a decrease of the signal by a factor two.
In addition to the main scientific objectives, PHEBUS will contribute to some other studies concerning to the astrophysics, the solar physics and the solar system physics. For example, the measurements at the H, He, He+ emission lines (121.6, 58.4 and 30.4 nm) can provide new information about the interstellar gas in the heliosphere and its interaction with the solar wind. Furthermore, the emission lines of the solar corona can be observed when the sun is occulted by the Hermean disk: in this configuration the coronal lines will be superimposed with Mercury exospheric lines but many information about the corona composition and dynamics could be obtained. Moreover, from the Mercury orbit, PHEBUS will be able to observe in the EUV and FUV range the interaction between comets and asteroids with the inner part of the heliosphere as well as the spectrum of hot UV stars useful to characterize their composition and temperature.

In order to address the scientific objectives, different modes of observation will be used sequentially. These modes have been defined to optimize the science returns avoiding instrument damages or degradation. For the exospheric science, four modes of operation can be used. In the *Mode 1* the disk of Mercury is used as shield against the solar light; the illuminated exosphere is observed above the dark part in the near-terminator region, when the spacecraft is in the night-side. In this mode, which can be used during ingress or egress, PHEBUS can probe the regions with altitude as low as possible (reaching also the surface), where exospheric species density is highest. In the *Mode 2* is performed a sampled vertical scan of the atmosphere, between the lowest admissible altitude(0 km if the spacecraft is in the shadow, or a specified guard altitude if it is on the dayside) to typically 1000 km of altitude. In *Mode 3*, the instrument field of view is aligned with the velocity vector of the spacecraft and the exospheric emission over the illuminated part of the orbit are continuously

[1]The Rayleigh (R) is a unit of photon flux, used to measure very weak emissions like the Mercury exosphere lines. One Rayleigh (1 R) is defined as a column emission rate of 10^{10} photons per square meter per column per second. The relationship between photon radiance, $\boldsymbol{L}$ (ph m^{-2} sr^{-1}), and $\boldsymbol{R}$ (in units of Rayleigh) is simply

$$\boldsymbol{R} = \boldsymbol{L}\frac{10^{10}}{4\pi}$$

recorded. The data collected from this operation mode allow to reconstruct, through differentiation, the local density of observed species along the orbit. The same can be done if the field of view is oriented in the anti-velocity direction or at a defined angle from it. With a similar concept, in *Mode 4* the baffle orientation is continuously changed in order to observe the illuminated exosphere at a fixed altitude during the orbit. The information collected in this operation mode allow to map the exospheric characteristics as function of the altitude and orbital position.
For the water-ice and sulfur research the operational *Mode 5* is used. In this mode, the instrument field of view is pointed downward to the nadir on the night-side of the planet. The albedo of the surface, illuminated by the interplanetary glow at 121.6 nm, is mapped in selected regions of interest, in order to search surface ice layers (H_2O, SO_2, N_2, CO_2, etc..). Finally, in the operational *Mode 6*, the instrument field of view is pointed toward targets outside of the Mercury system. Typical targets are stars (for calibration purposes or science purposes), eventual comets or asteroids in the inner part of the heliosphere or part of the solar corona. In Figure 1.10 are schematically reported the observation modes foreseen for PHEBUS.

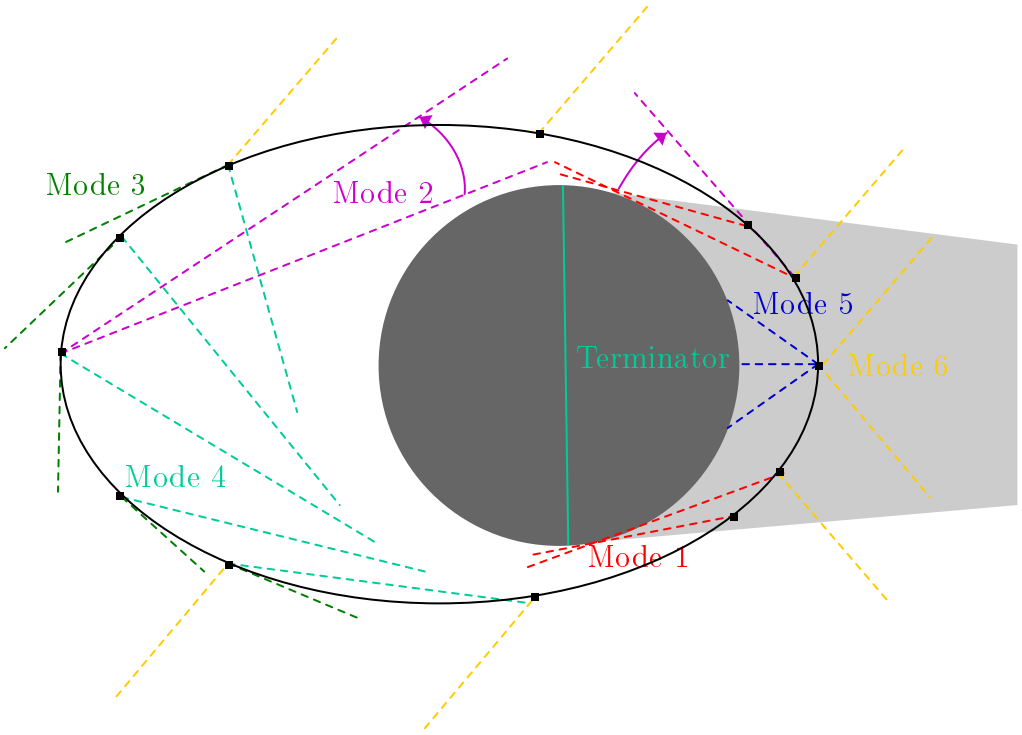

Figure 1.10. Schematic view of the different observation modes foreseen for PHEBUS.

1.2.3 PHEBUS models

In the development of PHEBUS, different kinds of instrument models have been realized in order to test if the design requirements have been achieved.

- The *Structural Thermal Model* (STM): is a model representative from the thermal and mechanical point of view. It is realized in order to test if the thermo-mechanical design achieves the project requirements (thermal resistance, vibration and shock test, etc.). This prototype has mounted inside only dummy components with similar mass to the final optical components.
- The *Optical prototype* (OP): is a model useful to test the optical concept of the instrument only from an optical point of view.
- The *Electronic Model* (EM): is used to test the electronic of the instrument (functions, EM compatibility, ect.). No optical components are mounted in the EM model.
- *Qualification Model* (QM): it is identical to the final instrument from all the points of view (i.e. thermal, mechanical, optical and electronic). It will be tested in the same way as the final instrument and it will be very useful as a "spare" model if further investigations will be necessary once the final instrument has been already launched. For these instrument, the calibration is required.
- *Flight Model* (FM) : it is the final model that will be launched.

The calibration activities are foreseen for both the QM and FM. Obviously, the FM calibration is needed in order to understand the data collected by the instrument during the mission. On the other hand, the QM calibration is also important for two reasons: the QM calibration activities can be used as training for the FM calibration activities and the calibrations obtained will be used as cross-comparison between the QM and FM. In the following chapters the radiometric characterization problem will be addressed and the experimental activities performed and/or planned will be applied to both models.

Chapter 2

The radiometric model of PHEBUS

When an instrument observes a faint target, its objective is to know the radiance L (photons $\mathrm{m}^{-2}\,\mathrm{sr}^{-1}\mathrm{s}^{-1}$) of an extended source (with respect to the source wavelength) by measuring a count rate R (in general counts s^{-1}). The model that links what we measure (the count rate R) and what we want to know (the radiance L) is the main purpose of the radiometric model. We can sum up the issue as follow:

$$R^{(tot)} = \mathfrak{R}_{extended}(L)$$

where $\mathfrak{R}_{extended}$ is the *radiometric function* of the instrument for extended sources observations [31]. An instrument may also observe stars either because a star appears in the field of view or for in-flight calibrations purposes or because the star itself is the scientific target. A star is not extended but a punctual object and it is more convenient characterized the source with its irradiance S (photons $\mathrm{m}^{-2}\mathrm{s}^{-1}$) at the entrance pupil plane. The radiometric function becomes

$$R^{(tot)} = \mathfrak{R}_{punctual}(S)$$

The operating range of the instrument is usually designed in order to have a linear behavior in term of radiance (or irradiance). With this assumption the function $\mathfrak{R}$ is also linear and the previous relations become

$$\begin{aligned} R^{(tot)} &= G_{eff}L \qquad \text{for extended sources} \\ R^{(tot)} &= A_{eff}S \qquad \text{for punctual sources} \end{aligned}$$

where G_{eff} is named *effective Étendue* ($\mathrm{m}^2\,\mathrm{sr}$) and A_{eff} is named *effective collecting area* (m^2).

In this chapter is discussed how to build a full radiometric model for a general optical instrument taking into account also the polarization status of the source. The method proposed is applied to the spectrometer PHEBUS [31]. The first section gives some concepts about the polarization and the mathematical methods to

analyze it. In the second section the analysis of the effects induced by PHEBUS onto an incoming light is presented and in the third section the main geometrical factors that can be affect the total count rate $R^{(tot)}$ of the instrument are discussed. Finally, in the last section, the full radiometric model of PHEBUS is presented.

2.1 The polarized light effects

Christian Huygens was the first to suggest that light was not a scalar quantity based on his work on the propagation of light through crystals; it appeared that light had preferred directions. This vectorial nature of light is called polarization. After about a century of investigations it was demonstrated by Maxwell that the light is an electromagnetic wave. Form the Maxwell's equations solution, if we fix a Cartesian system and we take as propagation direction the z-direction, the light can be described with its electric filed vector $\boldsymbol{E}$ which lying in the xy plane [32]. Furthermore, the electric field may conveniently be considered as composed by two components along the x and y directions

$$\begin{aligned} E_x(t,z) &= E_{0x}\cos\left(\omega t - \frac{2\pi}{\lambda}z + \delta_x\right) \\ E_y(t,z) &= E_{0y}\cos\left(\omega t - \frac{2\pi}{\lambda}z + \delta_y\right) \end{aligned} \tag{2.1}$$

where E_{0x} and E_{0y} are the amplitudes of the components, δ_x and δ_y are the phases of the components, λ is the wave's wavelength and ω is the wave's angular frequency. As the field propagates in the space, the resultant vector $\boldsymbol{E}$ describes a projected locus of points in the plane xy which can be easily derived from a combination of the equations 2.1; after algebraic manipulations we have [32]

$$\frac{E_x^2}{E_{x0}^2} + \frac{E_y^2}{E_{y0}^2} - 2\frac{E_x}{E_{x0}}\frac{E_y}{E_{y0}}\cos\delta = \sin^2\delta \tag{2.2}$$

where $\delta = \delta_y - \delta_x$ and the time-dependence of E_x and E_y has been omitted. Equation 2.2 is recognized as the equation of an ellipse and shows that during the propagation the locus of points projected on to the x-y plane in general is an ellipse. This behavior is called *optical polarization*, and the equation 2.2 is called the *polarization ellipse*; in figure 2.1 some examples of different kinds of locus that can be obtained from equation 2.2 are shown.

The electric field components can be also written as

$$\begin{aligned} E_x(t,z) &= \mathrm{Re}\left[\left(E_{0x}e^{j\delta_x}\right)e^{j\left(\omega t - \frac{2\pi}{\lambda}z\right)}\right] = \mathrm{Re}\left[\overline{E_x}e^{j\left(\omega t - \frac{2\pi}{\lambda}z\right)}\right] \\ E_y(t,z) &= \mathrm{Re}\left[\left(E_{0y}e^{j\delta_y}\right)e^{j\left(\omega t - \frac{2\pi}{\lambda}z\right)}\right] = \mathrm{Re}\left[\overline{E_y}e^{j\left(\omega t - \frac{2\pi}{\lambda}z\right)}\right] \end{aligned} \tag{2.3}$$

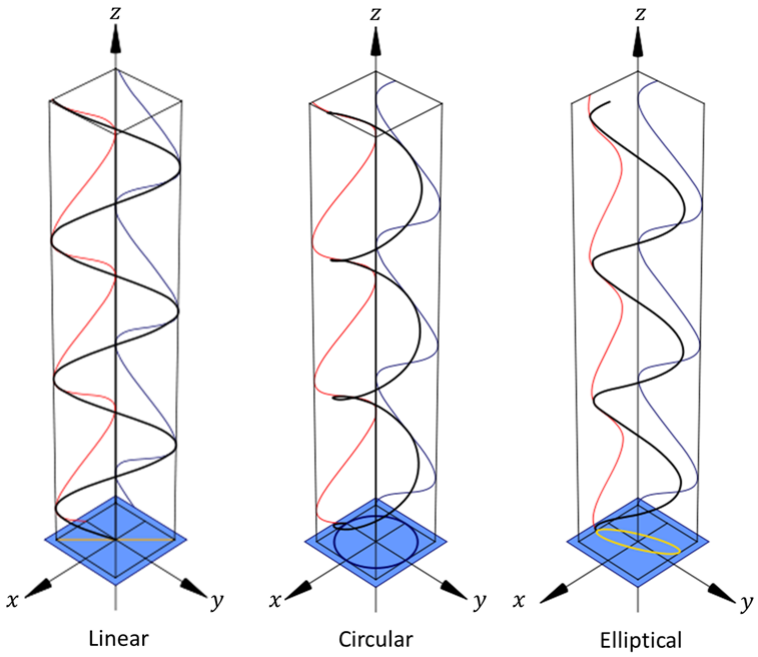

Figure 2.1. Examples of polarization locus that can be obtained from equation 2.2

where j is the imaginary unit. From equations 2.3 it seems clear that the electric field components can be uniquely identified by the complex numbers $\overline{E_x}$ and $\overline{E_y}$, named fasor, with modulus and phase equal to the amplitude and phase of the component represented (e.g. E_{0x} and δ_x for the x-component and E_{0y} and δ_y for the y-components) [33]. In fact, this operation is a fasorial transformation of the electric field which suppresses the propagation information without loss of generality and simplifies the calculations in polarization problems; hereafter the electric fields will be only described with their fasor, always indicated without the over-line.

The formalism of the polarization ellipse is applicable only when the light beam is full-polarized. When the light is unpolarized or partially polarized the electric filed direction has a random variation during the propagation and the equations 2.1 are not useful for its mathematical description; in these cases, different approaches of analysis have to be considered.

2.1.1 The Stokes - Mueller formalism

A full polarized beam of light can be described with different kinds of mathematical models each of which is suitable to specific problems. For example the polarization ellipse and the Jones's formalism [34, 35] are useful when the light is full-polarized and the electric fields can be described with mathematical expressions. On the contrary, when light is unpolarized or partially polarized the electric fields cannot be described with a simple equation: typical examples are the polarization behavior problems of imaging or non-imaging optical instruments observing natural sources. In such cases, a good mathematical description of the polarization effects can be obtained using the *Stokes-Mueller's formalism* [36, 37].

In 1852, Sir George Gabriel Stokes (1819-1903) observed that the polarization state of polarized light could be completely described by four measurable quantities now known as the Stokes polarization parameters. Let x-y-z be a reference system in which the z-direction is the propagation direction of a light beam with a generic polarization state. We define the Stokes's parameters of a light beam as

$$\begin{aligned} S_0 &= |E_x|^2 + |E_y|^2 \\ S_1 &= |E_x|^2 - |E_y|^2 \\ S_2 &= 2\,\mathrm{Re}\left(E_x E_y^*\right) \\ S_3 &= 2\,\mathrm{Im}\left(E_x E_y^*\right) \end{aligned} \tag{2.4}$$

where E_x and E_y are respectively the x-direction and y-direction components of the electric field of the light beam and E_y^* is the complex conjugate of E_y. The Stokes parameters just defined give a complete and unique description of any polarization state of light. The first parameter S_0 is the total irradiance of the light beam while the parameter S_1 describes the amount of horizontal or vertical linear

polarization, the parameter S_2 describes the amount of $+45$ or -45 linear polarization, and the parameter S_3 describes the amount of right or left circular polarization contained within the beam. The definition 2.4 shows also that the Stokes parameters are real quantities and are based on beam irradiances instead of the electric fields. This aspect is important because the amplitude of the optical field cannot be observed directly while, with the detectors, the quantity that can be measured is the irradiance: in fact, the Stokes parameters can be derived from four irradiance measurements [38]. As consequence of the definition 2.4, the Stokes parameters always satisfy the relation

$$S_0^2 \geq S_1^2 + S_2^2 + S_3^2$$

where the equality sign is applied when we have completely polarized light and the inequality when we have partially polarized light or unpolarized light. This aspect suggests us that in a partially polarized beam with irradiance $S_{tot} = S_0$ the parameters S_1, S_2 and S_3 describe the polarized part of the beam with an irradiance S_{pol} computable with the relationship

$$S_{pol} = \sqrt{S_1^2 + S_2^2 + S_3^2}.$$

Then, the Stokes parameters allow us to describe the degree of polarization P for any state of polarization applying the definition

$$P = \frac{S_{pol}}{S_{tot}} = \frac{\sqrt{S_1^2 + S_2^2 + S_3^2}}{S_0}$$

where the value of $P = 1$ corresponds to completely polarized light, $P = 0$ corresponds to unpolarized light, and $0 < P < 1$ corresponds to partially polarized light.

The four Stokes parameters can be also arranged in a column vector and written as

$$\boldsymbol{S} = \begin{pmatrix} S_0 \\ S_1 \\ S_2 \\ S_3 \end{pmatrix}$$

which is called Stokes vector. Usually, in the polarization problems we are interested to the polarization state of the light without considering the irradiance of the beam; then, in these cases it is more convenient to use the normalized Stocks vector $\widehat{\boldsymbol{S}}$ defined as

$$\widehat{\boldsymbol{S}} = \frac{1}{S_0}\boldsymbol{S}.$$

In Table 2.1 the normalized Stokes vectors for some useful polarization states are reported. The definition of the Stokes vector provides a formal method for treating

Polarization state	Electric field conditions	Stokes vector
Unpolarized	The electric field direction changes randomly	$\begin{pmatrix}1\\0\\0\\0\end{pmatrix}$
Linear horizontal	$E_{0y}=0$	$\begin{pmatrix}1\\1\\0\\0\end{pmatrix}$
Linear vertical	$E_{0x}=0$	$\begin{pmatrix}1\\-1\\0\\0\end{pmatrix}$
Linear at 45°	$E_{0x}=E_{0y},\quad \delta=0°$	$\begin{pmatrix}1\\0\\1\\0\end{pmatrix}$
Linear at −45°	$E_{0x}=E_{0y},\quad \delta=180°$	$\begin{pmatrix}1\\0\\-1\\0\end{pmatrix}$
Circular right	$E_{0x}=E_{0y},\quad \delta=90°$	$\begin{pmatrix}1\\0\\0\\1\end{pmatrix}$
Circular left	$E_{0x}=E_{0y},\quad \delta=-90°$	$\begin{pmatrix}1\\0\\0\\-1\end{pmatrix}$

Table 2.1. Examples of normalized Stokes vectors appearance for some useful polarization states.

numerous complicated problems involving polarized light and allows us to define the space $\mathbb{S}$ which contains the Stokes vector of any polarization state.

The typical problem that can be addressed with the Stokes vectors formalism is the interaction between an optical element (such as a lens, a mirror, a surface, a polarizer, ...) and an incoming light beam described by a vector $\boldsymbol{S}$. After the interaction with the element, the incoming vector $\boldsymbol{S}$ is changed in a new vector $\boldsymbol{S'}$ and this phenomena can be mathematically described by a transformation f defined

as

$$f : \mathbb{S} \to \mathbb{S}$$

where $\mathbb{S}$ is the Stokes space. Furthermore, if the optical component under investigation has a linear behavior in term of radiation irradiance, also f is a linear transformation and the relation between the incoming and outcoming Stocks vectors becomes

$$\boldsymbol{S'} = \begin{pmatrix} m_{11} & m_{12} & m_{13} & m_{14} \\ m_{21} & m_{22} & m_{23} & m_{24} \\ m_{31} & m_{32} & m_{33} & m_{34} \\ m_{41} & m_{42} & m_{43} & m_{44} \end{pmatrix} \boldsymbol{S} = \mathbf{M}\boldsymbol{S}$$

where $\mathbf{M}$ is the 4×4 matrix known as the Mueller matrix because it was introduced by Hans Mueller during the early 1940s.
The concept of Mueller calculus can be extended to a more complex optical system, composed by a set of linear optical elements, which change the polarization state of the impinging light beam according to the Mueller matrices $\mathbf{M}_i$ of each subsystem. The complex optical system can be still described with an equivalent matrix that can be computed by an orderly left-production of the components Mueller matrices. For example, the equivalent Mueller matrix $\mathbf{M}_{eq}$ of a complex optical system realized by N optical components is

$$\mathbf{M}_{eq} = \mathbf{M}_N \mathbf{M}_{N-1} \cdots \mathbf{M}_2 \mathbf{M}_1$$

where with $\mathbf{M}_1$ and $\mathbf{M}_N$ are indicated respectively the Mueller matrices of the first and last component encountered by the incoming light beam. In the following, the Mueller matrices of the principal optical components useful in our analysis are discussed.

2.1.2 Reference system in the Stokes-Mueller calculus

The Stokes vectors and the Mueller matrices are dependent to the reference system adopted in the analysis. Conventionally, the Cartesian system is fixed in order to have the z-direction as the propagation direction of the beam and then the electric field of the radiation lying in the x-y plane. However, when the problem analyzes the interaction between a beam and an optical component, also the directions x and y have to be uniquely defined.
Let us consider a light beam incident on an optical element. The *plane of incidence* is defined as the plane including the beam propagation direction (the z-direction) and the normal to the optical element surface; hereafter we choose the y-direction in order to place the y-z plane coincident with plane of incidence. With the convention just fixed, the x-direction is perpendicular to the plane of incidence and is known as s-polarization (from the German "senkrecht" for perpendicular) or σ - polarization

or transverse electric (TE) polarization; the y-direction is parallel to the plane of incidence and is known as p-polarization (from the German "parallel" for parallel) or π-polarization or transverse magnetic (TM) polarization.

2.1.3 The polarizer in the Mueller formalism

A polarizer element is an anisotropic attenuator of the orthogonal components of the electric field for an incoming beam. With the convention assumed for the reference system, the incidence plane is parallel to the y-z plane and then the electric field components of the incoming $\boldsymbol{E}$ and outcoming $\boldsymbol{E'}$ beam are related by the relationships

$$E'_x = a_x E_x, \quad 0 \leq a_x \leq 1$$
$$E'_y = a_y E_y, \quad 0 \leq a_y \leq 1$$

where a_x is the transverse electric (TE) attenuation coefficient and a_y is the transverse magnetic (TM) attenuation coefficient. The value zero and one are assumed respectively when the component is totally eliminated or completely conserved. Applying the results just discussed to the definition of the Stocks parameters 2.4, after some algebraic manipulations we find the Mueller matrix of the polarizer as

$$\mathbf{M}_{pol} = \begin{pmatrix} \frac{|a_x|^2+|a_y|^2}{2} & \frac{|a_x|^2-|a_y|^2}{2} & 0 & 0 \\ \frac{|a_x|^2-|a_y|^2}{2} & \frac{|a_x|^2+|a_y|^2}{2} & 0 & 0 \\ 0 & 0 & 2a_x a_y & 0 \\ 0 & 0 & 0 & 2a_x a_y \end{pmatrix}$$

2.1.4 The phase retarder in the Mueller formalism

Retarder elements introduce a phase shift $\phi = \phi_x - \phi_y$ between the orthogonal components of the incident beam. Mathematically, we can also think about it as a phase shift of $\phi/2$ along the x-axis and of $-\phi/2$ along the y-axis. With the same reference system defined before, the components of the emerging beam can be expressed by the relationships

$$E'_x = e^{\frac{\phi}{2}} E_x$$
$$E'_y = e^{-\frac{\phi}{2}} E_y$$

Substituting now the conditions just discussed into the Stokes parameters definition 2.4, after some algebraic manipulations we find the Mueller matrix of a retarder as

$$\mathbf{M}_{ret} = \begin{pmatrix} 1 & 0 & 0 & 0 \\ 0 & 1 & 0 & 0 \\ 0 & 0 & \cos\phi & \sin\phi \\ 0 & 0 & -\sin\phi & \cos\phi \end{pmatrix}$$

2.1.5 Mirrors and gratings in the Mueller formalism

A generic reflective element is an interface between two different mediums in which part of an incoming light is reflected back. Solving the Maxwell equations for the reflector, it can be shown that the polarization state of an incident beam changes after reflection. With the same convention for the reference system, the z-direction is the beam propagation direction and the incidence plane of the reflector is the y-z plane; from the Maxwell equations solution we have

$$E'_x = r_x E_x, \quad r_x \in \mathbb{C} \tag{2.5a}$$
$$E'_y = r_y E_y, \quad r_y \in \mathbb{C} \tag{2.5b}$$

where E_x, E_y and E'_x, E'_y are the incoming and outcoming electric field components, r_x is the transverse electric (TE) reflection coefficient and r_y is the transverse magnetic (TM) reflection coefficient. If the reflector is non-absorbent the reflection coefficients are real numbers always less than 1 and then it can changes only the relative amplitude between the electric field components. On the contrary, if the reflector is absorbent, its reflection coefficients are complex and they introduce also a phase shift between the electric field components: this is the general case of a mirror in which is chosen a high absorbent material in order to improve the reflection power at the interface [39]. Applying the definition of the Stokes parameters 2.4 with the conditions 2.5, after some algebraic manipulations we find the Mueller matrix

$$\mathbf{M}_{ref} = \begin{pmatrix} \frac{|r_x|^2+|r_y|^2}{2} & \frac{|r_x|^2-|r_y|^2}{2} & 0 & 0 \\ \frac{|r_x|^2-|r_y|^2}{2} & \frac{|r_x|^2+|r_y|^2}{2} & 0 & 0 \\ 0 & 0 & 2\,\mathrm{Re}\,(r_x r_y^*) & 2\,\mathrm{Im}\,(r_x r_y^*) \\ 0 & 0 & -2\,\mathrm{Im}\,(r_x r_y^*) & 2\,\mathrm{Re}\,(r_x r_y^*) \end{pmatrix}$$

It is interesting to note that the Mueller matrix of a generic reflector can be also derived describing its behavior as a polarizer with extinction coefficients r_x and r_y in series to a phase retarder with a delay ϕ [40]

$$\mathbf{M}_{ref} = \mathbf{M}_{ret}\mathbf{M}_{pol} = \begin{pmatrix} \frac{|r_x|^2+|r_y|^2}{2} & \frac{|r_x|^2-|r_y|^2}{2} & 0 & 0 \\ \frac{|r_x|^2-|r_y|^2}{2} & \frac{|r_x|^2+|r_y|^2}{2} & 0 & 0 \\ 0 & 0 & 2|r_x||r_y|\cos\phi & 2|r_x||r_y|\sin\phi \\ 0 & 0 & -2|r_x||r_y|\sin\phi & 2|r_x||r_y|\cos\phi \end{pmatrix}$$

where $|r_x||r_y|\cos\phi = \mathrm{Re}\,(r_x r_y^*)$ and $|r_x||r_y|\sin\phi = \mathrm{Im}\,(r_x r_y^*)$.

Finally, a grating and a reflector can be handled in the same way from the polarization point of view. In fact, a grating can be considered as a reflective element at its n-order in which it has its specific reflection coefficients.

2.1.6 The rotator in Mueller formalism

The geometry of an optical system can imply that the planes of incidence of the optical elements are not parallel one to each other; from a mathematical point of view, this situation can be modeled introducing a "dummy component", named rotator, which rotates the orthogonal electric field components E_x and E_y of an angle θ[1].

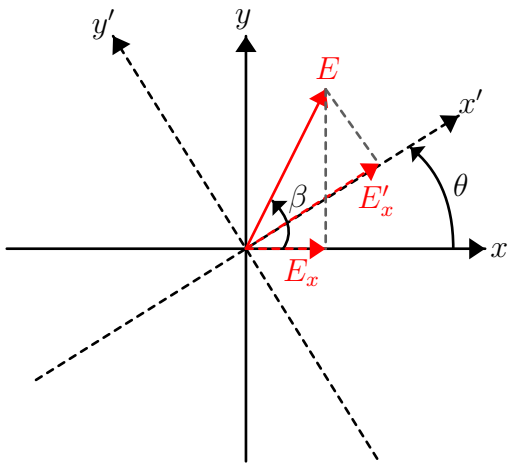

Figure 2.2. A sketch of the classical rotation problem performed by a rotator component.

As shown in Figure 2.2, if β is the angle between the vector $\boldsymbol{E}$ and axis x we have

$$E_x = E\cos\beta \tag{2.6a}$$
$$E_y = E\sin\beta \tag{2.6b}$$

and, at the same time, we can write

$$E'_x = E\cos(\beta-\theta) \tag{2.7a}$$
$$E'_y = E\sin(\beta-\theta) \tag{2.7b}$$

From equations 2.6 and 2.7, after some manipulations we find

$$E'_x = E(\cos\beta\cos\theta+\sin\beta\sin\theta) = E_x\cos\theta+E_y\sin\theta \tag{2.8a}$$
$$E'_y = E(\sin\beta\cos\theta-\cos\beta\sin\theta) = E_y\cos\theta-E_x\sin\theta \tag{2.8b}$$

[1]With this dummy component we change the base for the incoming Stokes vector because the new reference system is rotated by an angle θ with respect to the previous one.

Applying the results obtained in 2.8 into the definition of the Stocks parameters 2.4 after a lot of algebraic manipulations we find that a rotator element can be described by the Mueller matrix

$$\mathbf{M}(\theta) = \begin{pmatrix} 1 & 0 & 0 & 0 \\ 0 & \cos 2\theta & \sin 2\theta & 0 \\ 0 & -\sin 2\theta & \cos 2\theta & 0 \\ 0 & 0 & 0 & 1 \end{pmatrix}$$

It worth to note that in the matrix $\mathbf{M}(\theta)$ appears the angle 2θ and not the angle θ. Intuitively this is a directly consequence of the "irradiance nature" of the Stokes parameters definition.

2.1.7 Detector device in the Mueller calculus

A detector is a particular optical element because it gives a count rate R (photons $\mathrm{m}^{-2}\ \mathrm{s}^{-1}$) correlated to the total irradiance of an impinging light beam. In a general case, the detectors can be described as a transformation g defined as

$$g : \mathbb{S} \to \mathbb{R}^{+}$$

where the $\mathbb{R}^{+}$ is the set of the positive real numbers. In the applications, the detectors is designed in order to have a linear behavior with the irradiance or, alternatively, it is made to work in a linear part of its characteristic so that the transformation g becomes linear and in general is described by the relationship

$$R = \begin{pmatrix} \eta_1 & \eta_2 & \eta_3 & \eta_2 \end{pmatrix} \boldsymbol{S} = \mathbf{D}\boldsymbol{S} \tag{2.9}$$

The values η_i depend on the physics of the detector and usually they are experimentally obtained[2]. When the detector is polarization independent, the count rate R depends only on the total irradiance of the impinging light beam represented by the Stokes parameter S_0. In this case, the transformation 2.9 becomes

$$R = \begin{pmatrix} \eta_d & 0 & 0 & 0 \end{pmatrix} \boldsymbol{S} = \eta_d S_0 \tag{2.10}$$

where η_d is the total efficiency of the detector.

[2]If in front of the detector is interposed a protective window, the system can be described with the relationship

$$\mathbf{D}_{eq} = \mathbf{D}\,\mathbf{M}_{window}$$

where $\mathbf{M}_{window}$ is the Mueller matrix of the window. The results $\mathbf{D}_{eq}$ is still a vector of four element. Hereafter, the eventual protective window will be considered part of the detector and then in our discussion we will use also the equivalent transformation $\mathbf{D}_{eq}$.

2.2 PHEBUS and the polarized light

An exhaustive approach that takes into account the polarization state of the light entering into PHEBUS spectrometer and the polarization dependence of its efficiency[3] can be mathematically formalized in term of the Mueller-Stokes calculus. The idea proposed in this section has general validity and allows to improve the astronomical observations when applied to a flight instrument. In the case of PHEBUS, the Mercury's exosphere, that is still under investigation, could be slightly polarized [41, 42] and then the residual dependence to polarization must be evaluated to fully interpret the response of the instrument. The approach assumes that each optical instrument induces a polarization change on the input light, resulting in a very complex instrument response strongly dependent on the polarization status of the incoming light. In particular, it must be remembered that each optical component not only affects the throughput, but introduces also a phase shift between the impinging light components, whenever the incident angle is different from 0. Usually, these dependencies are not expressed in the calibration of optical instruments, being neglected in name of the *normal incidence configuration* usually adopted. The importance of this approach is even more dramatic if the instrument, as in the case of PHEBUS, is provided by a scanning system which changes dynamically the mutual position of the incidence planes of the optical elements.

2.2.1 The application of Mueller calculus to PHEBUS

The Mueller calculus is applied to PHEBUS and it is performed separately for EUV, FUV channel. The optical components involved in the path of light inside each channel are: the parabolic entrance mirror, that is shared in both channels, the EUV or FUV grating and the EUV or FUV detector. Furthermore, due to the rotation capability of the mirror around the instrument optical axis, the incidence plane of the entrance mirror rotates with respect to the incidence plane of the gratings obtaining a rotator effect. The geometry of the EUV channel is shown in Figure 2.3(a). Taking in account the figure, the PHEBUS equivalent matrix $\mathbf{M}_{PHEBUS}^{(EUV)}$ can be computed by the left-multiplication of the optical components Mueller matrices:

$$\mathbf{M}_{PHEBUS}^{(EUV)} = \mathbf{M}_{grating}^{(EUV)} \mathbf{M}_{scan}(\theta) \mathbf{M}_{mirror} \tag{2.11}$$

The detectors used to collect the radiation in PHEBUS are MCPs. In general, the detection efficiency associated to them depends on the polarization state of the

[3] The efficiency of the optical system doesn't take into account its geometric characteristic: the basic idea is to study the instrument response with a very small incoming beam entering in the center of the entrance pupil. Usually is said *a model built for the chief ray.*

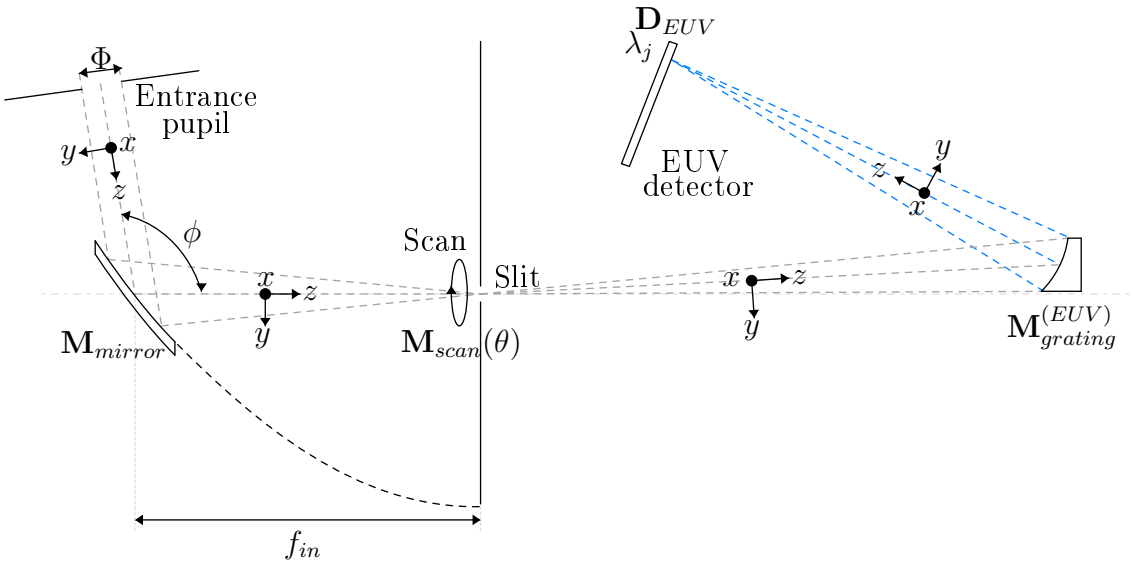

(a)

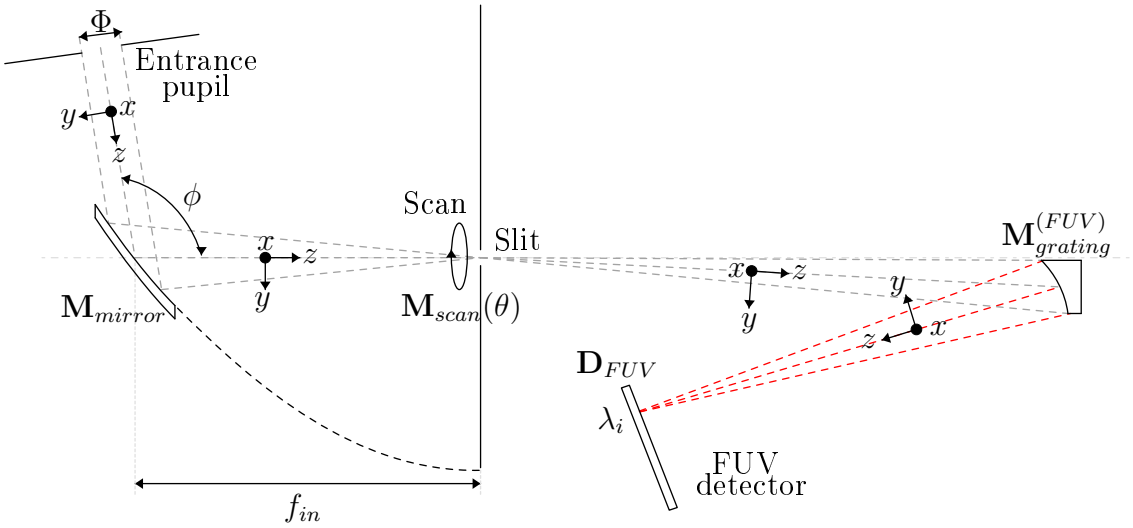

(b)

Figure 2.3. The PHEBUS channels optical layout: in Figure 2.3(a) is shown the EUV channel while in Figure 2.3(b) is shown the FUV channel. In the picture are also shown the optical components reference systems useful in Mueller calculus: z is the propagation direction, y is the transverse magnetic (TM) direction and x is the transverse electric (TE) direction.

incoming light and on the bias angle in the first stack [43]; however, the characterization performed onto the PHEBUS detectors has shown a negligible dependence on the polarization state of the impinging light beam [27, 28]. Then, taking into account this aspect, the detected signal is

$$\begin{aligned} R_{EUV} &= \mathbf{D}_{EUV}\mathbf{M}^{(EUV)}_{PHEBUS}\boldsymbol{S} = \boldsymbol{\eta}_{EUV}\boldsymbol{S} = \\ &= \begin{pmatrix}\eta_d & 0 & 0 & 0\end{pmatrix}\begin{pmatrix} m_{11} & m_{12} & m_{13} & m_{14} \\ m_{21} & m_{22} & m_{23} & m_{24} \\ m_{31} & m_{32} & m_{33} & m_{34} \\ m_{41} & m_{42} & m_{43} & m_{44}\end{pmatrix}\boldsymbol{S} = \\ &= \eta_{EUV}\left(m_{11}S_0 + m_{12}S_1 + m_{13}S_2 + m_{14}S_3\right) \end{aligned} \tag{2.12}$$

in which we can see that the relevant terms of the Mueller matrix $\mathbf{M}^{(EUV)}_{PHEBUS}$ are the coefficients of the first row. These coefficients are

$$\begin{aligned} m_{11} &= \frac{|r_x^{(g)}|^2 + |r_y^{(g)}|^2}{2}\frac{|r_x^{(m)}|^2 + |r_y^{(m)}|^2}{2} + \frac{|r_x^{(g)}|^2 - |r_y^{(g)}|^2}{2}\frac{|r_x^{(m)}|^2 - |r_y^{(m)}|^2}{2}\cos 2\theta \\ m_{12} &= \frac{|r_x^{(g)}|^2 + |r_y^{(g)}|^2}{2}\frac{|r_x^{(m)}|^2 - |r_y^{(m)}|^2}{2} + \frac{|r_x^{(g)}|^2 - |r_y^{(g)}|^2}{2}\frac{|r_x^{(m)}|^2 + |r_y^{(m)}|^2}{2}\cos 2\theta \\ m_{13} &= |r_x^{(m)}|^2|r_y^{(m)}|^2\frac{|r_x^{(g)}|^2 - |r_y^{(g)}|^2}{2}\cos\phi^{(m)}\sin 2\theta \\ m_{14} &= -|r_x^{(m)}|^2|r_y^{(m)}|^2\frac{|r_x^{(g)}|^2 - |r_y^{(g)}|^2}{2}\sin\phi^{(m)}\sin 2\theta \end{aligned} \tag{2.13}$$

where the suffix (m) indicates the entrance mirror, the suffix (g) indicates the grating and θ is the angle of the scanning system. Finally, we remind that these four parameters will depend on the wavelength λ of the incoming beam through the reflection coefficients of the entrance mirror and the efficiency of the grating.

With the same procedure followed for the EUV channel, the equivalent Mueller matrix for the FUV channel shown in Figure 2.3(b) is

$$\mathbf{M}^{(FUV)}_{PHEBUS} = \mathbf{M}^{(FUV)}_{grating}\mathbf{M}_{scan}(\theta)\mathbf{M}_{mirror} \tag{2.14}$$

and the output signal of the FUV detector will be

$$R_{FUV} = \mathbf{D}_{FUV}\mathbf{M}^{(FUV)}_{PHEBUS}\boldsymbol{S} = \boldsymbol{\eta}_{FUV}\boldsymbol{S} \tag{2.15}$$

The expression for each parameter of the generic Mueller matrix $\mathbf{M}_{PHEBUS}$[4] has been computed and reported in Appendix A for completeness reasons. Finally, we

[4]The equivalent Mueller matrix of PHEBUS has the same form for both channels. In fact, the coefficients expression changes numerically only for the efficiency of the grating; for this reason, hereafter the suffix will "(FUV)" and "(EUV)" will be omitted for convenience.

point out a general result: when the polarization state of the incoming light is taken into account, the efficiency of the instrument under investigation is a vector of four elements $\boldsymbol{\eta_I}$ obtained by the relationship

$$\boldsymbol{\eta_I} = \mathbf{D}\,\mathbf{M_I}$$

where $\mathbf{M_I}$ is the Mueller matrix of the instrument and $\mathbf{D}$ is the transformation that describes the instrument detector.

2.2.2 Numerical simulations of the polarization effects

In order to understand the effects of PHEBUS instrument onto the incoming beam polarization state, numerical simulations of the system were performed.
Starting from the optical elements design, the input information like materials, thickness of the coatings and the grooves/mm parameter for the gratings have been used to simulate the optical performances of each element: from the simulation results the Mueller matrix of each component has been derived. Finally, the equivalent Mueller matrix $\mathbf{M}_{PHEBUS}$ for each channel has been computed and discussed. The simulations obtained will be also compered with experimental data observed and any discrepancies will be evaluated. This is an important step because the simulations can be affected by uncertainty: for example, in the simulations of the optical coatings performances, the material optical constants used can be affected by uncertainty, especially at the wavelengths greater than 120nm. In the case of gratings reflectance, the simulations may instead be less significant because a grating response is harder to properly modeled due to the big quantity of parameters that affect the final result.

The entrance mirror simulations:

The entrance mirror of PHEBUS is an off-axis parabola working at 50° of incidence and it is realized by a super-polished Silicon Carbide substrate [1]. On top of the substrate a thick coating of SiC is deposited. The coating simulations of the entrance mirror have been performed by using the IMD software [44] and adopting for the Silicon Carbide material the Pallik's optical constants [45] in the FUV range and the Windt's optical constants in the EUV range [46]. The results are shown in Figure 2.4.

The gratings simulations:

The two gratings of PHEBUS are aberration corrected holographic gratings. The gratings are made on an aluminum substrate with a 40 nm thick reflective platinum

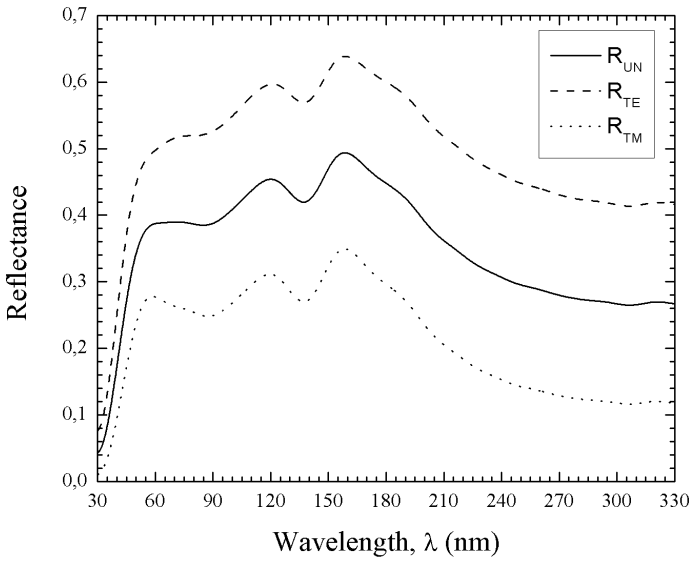

Figure 2.4. Reflectance simulations of the SiC entrance mirror performed by the IMD code. In the image is reported the TE and TM reflectance ($R_{TE} = |r_x^m|^2$ and $R_{TM} = |r_y^m|^2$) together their arithmetic average R_{UN}.

coating; the active area size foreseen is 42 mm by 15 mm. The mean grooves density designed is 1600 grooves/mm for the FUV and 2700 grooves/mm for the EUV. Groove profile is laminar ion-etched optimized for the respective spectral range.
The simulations of the EUV and FUV gratings have been performed by using the PC grate demo code [47]. The input parameters adopted for the simulation have been provided by the producer company Jobin Yvon , which performed the surface and groves shape characterization of the first prototype of PHEBUS gratings with the Atomic Force Microscope(AFM). In Figure 2.5 are shown the efficiency curves computed for the grating order -1, the working order of the spectrometer. The EUV grating has been evaluated only at its wavelength working range ($55 - 155$nm) because the efficiency at longer wavelengths is negligible; the FUV has been evaluated also at lower wavelengths with respect to its working range ($145 - 315$ nm) because its efficiency is still considerable (see Figure 2.5(b)).

The first row coefficients of the PHEBUS matrix:

The first row coefficients of the PHEBUS Mueller matrix have been computed for each channel using the optical simulations obtained for each subsystem element.

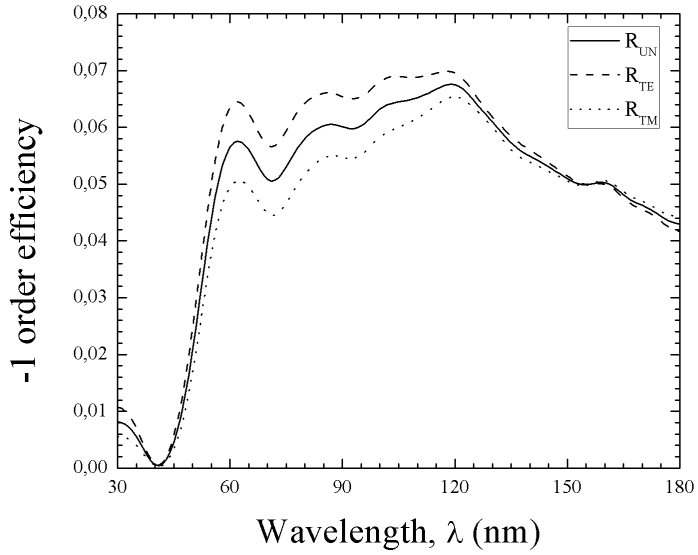

(a)

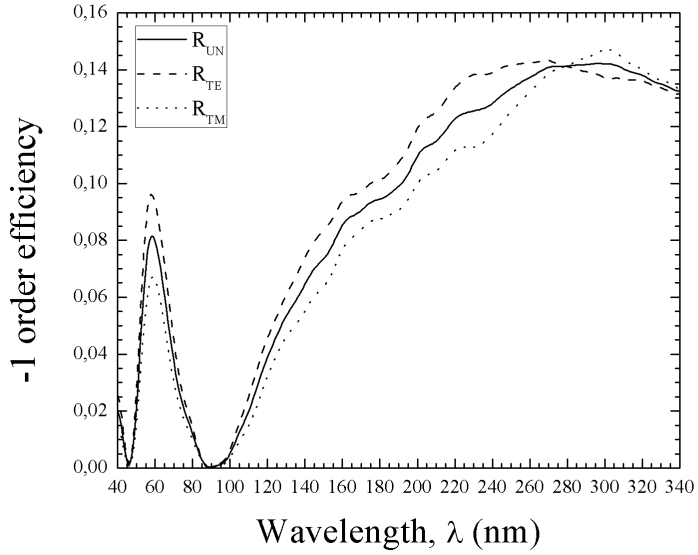

(b)

Figure 2.5. Efficiency simulations of the -1 order for the EUV grating (Figure 2.5(a)) and FUV grating (Figure 2.5(b)) performed by PC grate demo version. In the images the TE and TM efficiency ($R_{TE} = |r_x^g|^2$ and $R_{TM} = |r_y^g|^2$) together their average R_{UN} are reported.

From the equations 2.13, we can observe that m_{13} and m_{14} are zero when the scanning angle θ is zero or 180°; at the angles $\theta = 90°$ or $\theta = 270°$ the m_{11} and m_{12} coefficients are at their minimum value. On the contrary, the modulus of the coefficients m_{13} and m_{14} are maximized for the scanning angle $\theta = 45°$ or $\theta = 135°$. From these observations and since all coefficients vary with 2θ-sinusoidal trends, the angle $\theta = 45°$ (or, equivalently, the angle $\theta = 135°$) becomes the "magic" working angle useful to evaluate the real impact of the last two coefficients m_{13} and m_{14} on the instrument response. The first row coefficients of the matrix computed for $\theta = 45°$ are shown in Figure 2.6 for both PHEBUS channels.

Figure 2.6 suggests that the values of m_{13} and m_{14} are still at least one order lower than m_{12} at each wavelength in both channels; then, the instrument response can be rewritten according to the following approximation:

$$R \simeq \eta_d \left(m_{11} S_0 + m_{12} S_1 \right) \tag{2.16}$$

Finally, in order to estimate the relative importance between the stokes parameters S_0 and S_1 of the input light beam we have calculated the instrument output R for a different set of Stokes parameters described by the vector

$$\boldsymbol{S} = \begin{pmatrix} 1 \\ \pm P \\ 0 \\ 0 \end{pmatrix}$$

where P is the degree of polarization; in fact this set of Stokes vectors describes different source status, ranging from a completely unpolarized one ($P = 0$) to a completely linearly polarized one ($P = 1$). If the degree of polarization of the source is less than 0.2, (i.e. $\boldsymbol{S} = \begin{pmatrix} 1 & \pm 0.2 & 0 & 0 \end{pmatrix}^T$), the calculated instrument response R can be approximated as

$$R \simeq \eta_d \left(m_{11} S_0 + C \right)$$

where C is a correction factor lower than 10% [48]. In this case, the recovering of the irradiance of the input source can be obtained by knowing only m_{11} with an error lower than 10%. Instead, for higher polarization factors, the approximation 2.16 have to be adopted.

2.2.3 Instrument level evaluation of m_{11} and m_{12}

The polarization behavior of the spectrometer PHEBUS can be described with a well approximation when the first two coefficients m_{11} and m_{12} of the instrument Mueller matrix are known. Their values are usually indirectly determined by the

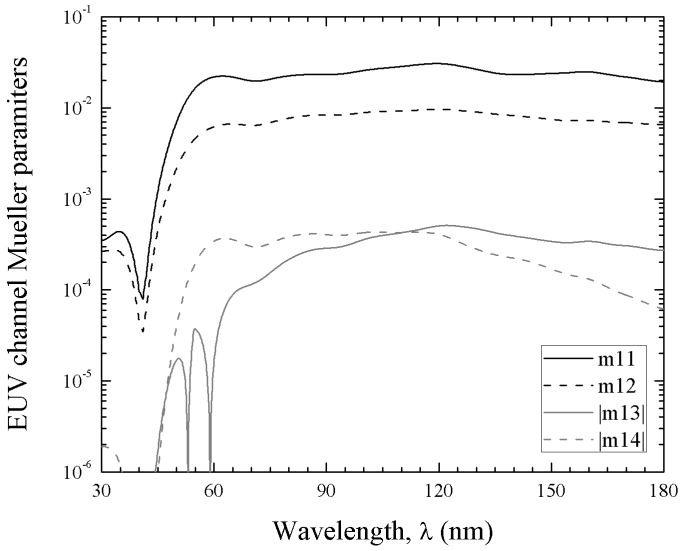

(a)

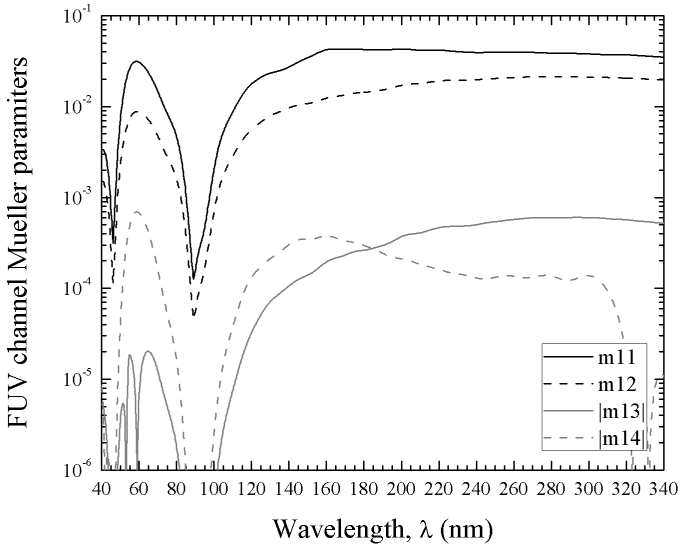

(b)

Figure 2.6. The first row parameters of the Mueller matrix of PHEBUS with a scanning angle $\theta = 45°$; in Figure 2.6(a) the coefficients are computed for the EUV channel while in Figure 2.6(b) are computed for the FUV channel.

experimental characterization of each subsystem element[5] but they can be also found by instrument level measurements. The method is demonstrated by using Stokes-Mueller formalism and without considering the form of the PHEBUS matrix terms. Then, again, the results obtained can be applied not only to PHEBUS but onto a generic optical instrument.

Let $\boldsymbol{S}$ be the Stokes vector of a light beam incoming into a optical instrument described by the equivalent Mueller matrix $\mathbf{M}_I$. If the instrument is rotated around the z-axis by an angle α, the equivalent Mueller matrix of the instrument changes because the planes of incidence of each element rotate with respect to the reference system adopted at the beginning. The new Mueller matrix of the rotated instrument $\mathbf{M}_I^{(\alpha)}$ can be derived from the previous one considering before the instrument a rotator element described by the matrix $\mathbf{M}(\alpha)$. We have

$$\begin{aligned}\mathbf{M}_I^{(\alpha)} = \mathbf{M}_I\mathbf{M}(\alpha) = \begin{pmatrix} m_{11} & m_{12} & m_{13} & m_{14} \\ m_{21} & m_{22} & m_{23} & m_{24} \\ m_{31} & m_{32} & m_{33} & m_{34} \\ m_{41} & m_{42} & m_{43} & m_{44} \end{pmatrix} \begin{pmatrix} 1 & 0 & 0 & 0 \\ 0 & \cos 2\alpha & \sin 2\alpha & 0 \\ 0 & -\sin 2\alpha & \cos 2\alpha & 0 \\ 0 & 0 & 0 & 1 \end{pmatrix} = \\ = \begin{pmatrix} m_{11} & m_{12}\cos 2\alpha - m_{13}\sin 2\alpha & m_{12}\sin 2\alpha + m_{13}\cos 2\alpha & m_{14} \\ * & * & * & * \\ * & * & * & * \\ * & * & * & * \end{pmatrix}\end{aligned} \tag{2.17}$$

where with the symbol $*$ are indicated the terms that are unnecessary for our analysis. After the assumption that the detector of the instrument is polarization insensitive, the response of the rotated instrument can be write as

$$\begin{aligned} R^{(\alpha)} &= \begin{pmatrix} \eta_d & 0 & 0 & 0 \end{pmatrix} \mathbf{M}_I^{(\alpha)} \boldsymbol{S} = \\ &= \eta_d \left[S_0 m_{11} + m_{12} \left(S_1 \cos 2\alpha + S_2 \sin 2\alpha \right) + m_{13} \left(S_2 \cos 2\alpha - S_1 \sin 2\alpha \right) + m_{14} S_3 \right] \end{aligned}$$

in which we find that the contribution of the Stokes parameters S_0 and S_3 are independent to the instrument rotation angle α. In general, knowing the polarization state of the input light $\boldsymbol{S}$, with three distinct measurements performed at different angles α not too closed to each other, we can find the terms $S_0 m_{11} + m_{14} S_3$, m_{12} and m_{13} solving a system of three linear equations with three unknowns; unfortunately, in a general case the terms m_{11} and m_{13} cannot be isolated.

[5] This is the method adopted also for PHEBUS spectrometer and it will be discussed in Chapter 3.

Consider now the special case of incoming light described by the Stokes vector

$$\boldsymbol{S} = \begin{pmatrix} S_0 \\ S_1 \\ 0 \\ 0 \end{pmatrix} = S_0 \begin{pmatrix} 1 \\ \pm P \\ 0 \\ 0 \end{pmatrix}.$$

where, in this particular case, the degree of polarization P takes the name *polarization factor*; in fact, this is a partially polarized light with a horizontal or vertical polarized component[6]. The instrument response becomes

$$R^{(\alpha)} = \eta_d S_0 \left[m_{11} + m_{12}(\pm P) \cos 2\alpha - m_{13}(\pm P) \sin 2\alpha \right]$$

and evaluating it at $\alpha = 0°$ and $\alpha = 90°$, we obtain the system of two equation and two unknowns:

$$\begin{cases} R^{(0°)} = \eta_d S_0 \left[m_{11} + m_{12}(\pm P) \right] \\ R^{(90°)} = \eta_d S_0 \left[m_{11} - m_{12}(\pm P) \right] \end{cases} \tag{2.18}$$

The solutions of the system 2.18 are

$$m_{11} = \frac{R^{(0°)} + R^{(90°)}}{2\eta_d S_0}$$
$$m_{12} = \frac{R^{(0°)} - R^{(90°)}}{2\eta_d S_0(\pm P)}$$

Furthermore, if we write an additional equation obtained by evaluating the instrument response at $\alpha = 45°$, also the coefficient m_{13} can be retrieved:

$$m_{13} = \frac{R^{(0°)} + R^{(90°)}}{2\eta_d S_0(\pm P)} - \frac{R^{(45°)}}{\eta_d S_0(\pm P)}.$$

2.3 Geometrical response

The polarization effects analyzed in the previous paragraph has been performed considering a very small size beam entering in the center of the of the entrance pupil. In others words, the model has been built for the chief ray. However, in a complete radiometric model, the geometry of the instrument and its capability to collect optical energy from a source have to be considered.
As example, let us consider a Newtonian telescope; when the size of the primary

[6] As will be discussed in Chapter 3, this polarization state describe also the test beam obtainable in a normal incident reflectometer facility.

mirror increases also the light-gathering capability of the instrument increases and at the focus we have much more optical energy. In contrast, if a diaphragm is placed before the primary mirror (vignetting in the system) or the secondary mirror is misaligned (the image plane position change with respect to the detector) the optical energy available at the focus decreases. In this paragraph we investigate the geometry effects onto the output response and we define the main parameters useful to model the geometrical behavior of an optical instrument. The results will be applied to PHEBUS.

2.3.1 Definition of radiance

As it is shown in Figure 2.7, let us consider an infinitesimal source element with area $\mathrm{d}A_S$ which emits a radiant power $\mathrm{d}^2\Phi$ in the direction of viewing at an angle ξ_S from the surface normal. The radiance L is defined as the quantity of radiant flux

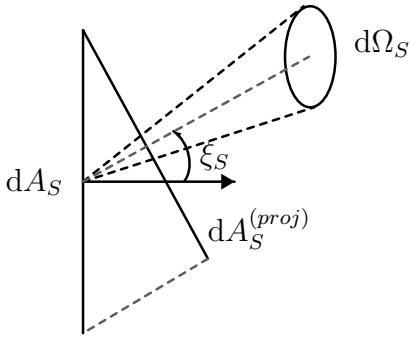

Figure 2.7. Radiant flux collecting per unit of solid angle along the direction making an angle ξ_S with the normal of the radiating area. The projected area of the surface is indicated with $\mathrm{d}A_S^{(proj)}$

emitted by the projected area perpendicular to the direction of viewing per unit of solid angle:

$$L = \frac{\mathrm{d}^2\Phi}{\mathrm{d}A_S \cos\xi_S \mathrm{d}\Omega_S} \tag{2.19}$$

The radiance has the same value at any point along a ray propagating in a uniform, non-absorbing medium. Figure 2.8 pictures a beam of light that pass from the infinitesimal source area $\mathrm{d}A_S$ to the receiver infinitesimal area $\mathrm{d}A_R$ situated at distance r from each other. The central ray of the light beam makes angles of ξ_S and ξ_R, respectively, relative to the areas normal.

At the source side, the solid angle $\mathrm{d}\Omega_S$ is

$$\mathrm{d}\Omega_S = \frac{\mathrm{d}A_R \cos\xi_R}{r^2}, \quad \text{where} \quad \mathrm{d}A_R \cos\xi_R = \mathrm{d}A_R^{(proj)}$$

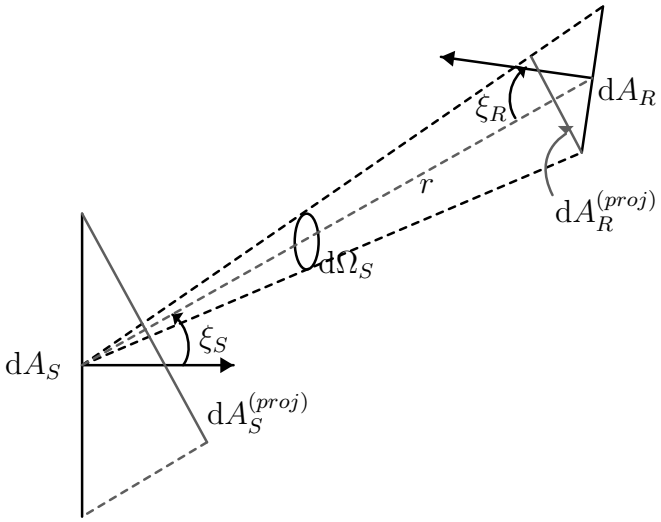

Figure 2.8. Geometry used to show the invariance of the radiance in a uniform lossless medium.

and, according to the definition 2.19, the radiance L_S at $\mathrm{d}A_S$ is given by

$$L_S = \frac{\mathrm{d}^2\Phi}{\mathrm{d}\Omega_S \mathrm{d}A_S \cos\xi_S} = \frac{\mathrm{d}^2\Phi}{\frac{\mathrm{d}A_R \cos\xi_R}{r^2}\mathrm{d}A_S \cos\xi_S}.$$

By similar argument, in which we reverse the role of the source and the receiver in Figure 2.8, we have

$$L_R = \frac{\mathrm{d}^2\Phi}{\mathrm{d}\Omega_R \mathrm{d}A_R \cos\xi_R} = \frac{\mathrm{d}^2\Phi}{\frac{\mathrm{d}A_S \cos\xi_S}{r^2}\mathrm{d}A_R \cos\xi_R}$$

from which we conclude that $L_S = L_R$. This important propriety, named as *radiance invariant*, shows that when the medium is uniform and lossless a radiometric calculus can be performed indifferently from the point of view of either the source or receiver.

Let us suppose that an optical instrument is illuminated by a source characterized by the radiance L. The instrument can collect only the optical energy coming from points inside its field of view solid angle Ω_{FoV}. The quantity of radiant power arriving per a unit area at the entrance pupil is the irradiance S and it can be obtained by

$$S = \int_{\Omega_{FoV}} L \,\mathrm{d}\Omega.$$

In definition 2.4 the Stokes parameters and the Stokes vector $\boldsymbol{S}$ were defined in term of light beam irradiance; however, sometime it could be convenient to redefine them

in term of light beam radiance: in these cases we indicate as $\boldsymbol{L}$ the Stokes vector defined in term of radiance[7].

2.3.2 Extended source: the Étendue, real Étendue and effective Étendue

Suppose now, referring to the Figure 2.9, that we wish to know the quantity of radiant power reaching an entrance pupil infinitesimal element of area $\mathrm{d}A_R$ considering an ideal instrument. If L is the radiance of the source, from the instrument point of view we have

$$\mathrm{d}^2\Phi = L\,\mathrm{d}A_R\cos\xi\mathrm{d}\Omega_R$$

and the total radiant power at the entire instrument entrance pupil due to the entire field of view is, by integration,

$$\Phi = \int_{A_R}\int_{\Omega_{FoV}} L(x,y,\varphi,\psi)\cos\xi\,\mathrm{d}\Omega_R\mathrm{d}A_R \quad \text{with } \mathrm{d}\Omega_R = \mathrm{d}\varphi\mathrm{d}\psi,\ \mathrm{d}A_R = \mathrm{d}x\mathrm{d}y$$

where, by adding powers rather than amplitudes in this integration, we have tacitly assumed that the radiation source emits incoherent radiation; as shown, L is function of the source element position in the instrument field of view (φ,ψ) and entrance pupil element position (x and y). If the source L is independent to the infinitesimal

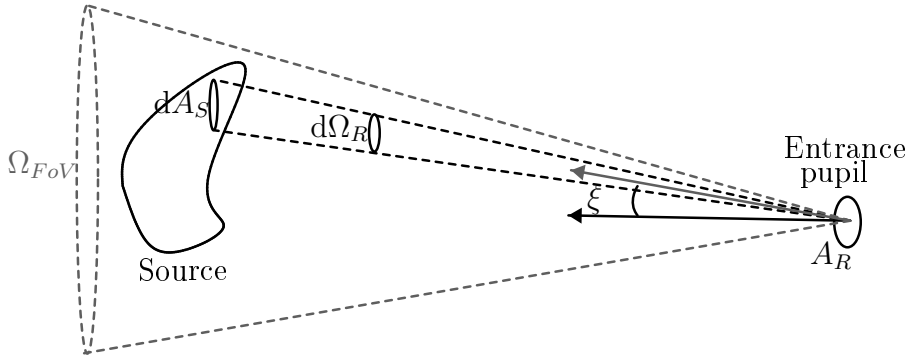

Figure 2.9. Geometry used to define the geometrical Étendue of an instrument.

source element position and to the infinitesimal entrance pupil element position[8], we can write $L(x,y,\varphi,\psi) = L_0$ and the total radiant power becomes

$$\Phi = L_0\int_{A_R}\int_{\Omega_{FoV}} \cos\xi\mathrm{d}\Omega_R\mathrm{d}A_R = L_0 G \tag{2.20}$$

[7] In this case the Stokes space is indicated as $\mathbb{L}$ instead of $\mathbb{S}$.

[8] This source is also said *Lambertian source*.

where the parameter G is named *Étendue*[9]. From 2.20 the Étendue parameters can be assimilated as a purely geometric quantity that measures the flux gathering capability of an ideal optical system.

In a real system, the instrument has losses due to the efficiency of each optical element. In additional, the system could be affected by vignetting or misalignment which decrease the total amount of energy transferred from the entrance pupil onto the detector. With a similar argument, for a general optical instrument we can define the effective Étendue as

$$G_{eff} = \int_{A_R} \int_{\Omega_{FoV}} V(x, y, \varphi, \psi)\eta(x, y, \varphi, \psi) \cos \xi \mathrm{d}\Omega_R \mathrm{d}A_R \tag{2.21}$$

where the function $V(x, y, \varphi, \psi)$, named *vignetting function*, takes into account the losses due to vignetting and misalignment and $\eta(x, y, \varphi, \psi)$ takes into account the losses due to the optical elements efficiency. We wish to point out that if the vignetting in the system is negligible, the function $V(x, y, \varphi, \psi) = 1 \quad \forall x, y, \varphi, \psi$; with the additional hypothesis $\eta(x, y, \varphi, \psi) = \eta_I$ we find an intuitive relationship between the Étendue and effective Étendue:

$$\begin{aligned} G_{eff} &= \int_{A_R} \int_{\Omega_{FoV}} \eta(x, y, \varphi, \psi) \cos \xi \mathrm{d}\Omega_R \mathrm{d}A_R = \\ &= \eta_I \int_{A_R} \int_{\Omega_{FoV}} \cos \xi \mathrm{d}\Omega_R \mathrm{d}A_R = \eta_I G \end{aligned} \tag{2.22}$$

Usually, the efficiency of each optics at the first order can be well approximated with the efficiency for the chief-ray and then the assumption $\eta(x, y, \varphi, \psi) = \eta_I$ seems reasonable[10]. However, for a real optical system, in general the vignetting effects cannot be neglected. In order to maintain the validity of the relationship 2.22, in a real case it seems appropriate to redefine the geometric Étendue as real geometric Étendue G_r,

$$G_r = \int_{A_R} \int_{\Omega_{FoV}} V(x, y, \varphi, \psi) \cos \xi \mathrm{d}\Omega_R \mathrm{d}A_R \tag{2.23}$$

[9] The term Étendue comes from the French *étendue géométrique*, meaning "geometrical extent". Other names for this property are acceptance, throughput, light-grasp, collecting power, optical extent, and $A\Omega$ product.

[10] Also for PHEBUS, the efficiency of each element has been computed also taking into account the different incidence angles due to the curvature of the optics but the differences obtained were negligible with respect to the efficiency of the chief-ray.

and then, we can write[11]

$$G_{eff} = \eta_I G_r \ .$$

As was described in section 2.2, if the incoming light is partially or full polarized, the efficiency η_I changes with the polarization state. The instrument behavior can be described with the Stokes-Mueller formalism from which the simple efficiency η_I and then the effective Étendue G_{eff} become a vector of four coefficients defined as

$$\begin{aligned} \boldsymbol{\eta_I} &= \mathbf{D}\,\mathbf{M_I} \\ \mathbf{G}_{eff} &= G_r\,\mathbf{D}\,\mathbf{M_I} \end{aligned} \tag{2.24}$$

where the $\mathbf{D}$ is detector transformation and $\mathbf{M_I}$ is the Mueller matrix of the optical instrument.
We are now ready to define the instrument full radiometric model in case of extended source observations. Let $\boldsymbol{L}$ be the radiance Stokes vector describing the polarization state of an extended source observed by our optical instrument which works in its linear range. The instrument is characterized by its real Étendue G_r, its Mueller matrix $\mathbf{M_I}$ and its detector transformation $\mathbf{D}$. The total output signal viewed by the instrument $R^{(tot)}$ (photons s^{-1}) can be estimated as

$$R^{(tot)} = G_r \mathbf{D}\mathbf{M_I}\boldsymbol{L} = \mathbf{G}_{eff}\,\boldsymbol{L} \tag{2.25}$$

2.3.3 Instrument level measurement of the real Étendue

In the calibration of an optical instrument it could be interesting to measure the real Étendue: the original and innovative method proposed here is the *Field of View mapping methods* [31]. In order to understand this experimental procedure, we start with the investigation of a radiometric properties that any optical instrument possesses.
Let $\boldsymbol{L}(x, y, \varphi, \psi)$ be the radiance Stokes vector of an arbitrary extended source that illuminate our instrument. If the source angular direction is changed by the offset angles (α, β), the new radiance vector becomes $\boldsymbol{L}(x, y, \varphi - \alpha, \psi - \beta)$. In general, we can write

$$\begin{aligned} R^{(tot)}(\alpha,\beta) &= \int_{A_R}\int_{\Omega_{FoV}} V(x,y,\varphi,\psi)\boldsymbol{\eta_I}(x,y,\varphi,\psi)\boldsymbol{L}(x,y,\varphi-\alpha,\psi-\beta)\cos\xi \mathrm{d}\Omega_R \mathrm{d}A_R \\ &= \int_{A_R}\int_{\Omega_{FoV}} \mathbf{V_I}(x,y,\varphi,\psi)\boldsymbol{L}(x,y,\varphi-\alpha,\psi-\beta)\cos\xi \mathrm{d}\Omega_R \mathrm{d}A_R \end{aligned}$$

[11] From the definitions 2.20, 2.21 and 2.23 we have

$$G_{eff} \leq G_r \leq G$$

where the equality occurs in an ideal lossless instrument.

where $\boldsymbol{\eta_I}(x, y, \varphi, \psi)$ is the instrument efficiency and $V(x, y, \varphi, \psi)$ is the vignetting function of the instrument.
We image now to change the angular position of the source and sum the instrument counts obtained for each position. From a mathematical point of view, we are integrating the counts over the direction (α, β):

$$\begin{aligned}
&\iint_{(\alpha,\beta)} R^{(tot)}(\alpha,\beta)\mathrm{d}\alpha\mathrm{d}\beta = \\
&= \iint_{(\alpha,\beta)} \left(\int_{A_R}\int_{\Omega_{FoV}} \mathbf{V_I}(x,y,\varphi,\psi)\boldsymbol{L}(x,y,\varphi-\alpha,\psi-\beta)\cos\xi \mathrm{d}\Omega_R \mathrm{d}A_R \right) \mathrm{d}\alpha\mathrm{d}\beta = \\
&= \int_{A_R}\int_{\Omega_{FoV}} \mathbf{V_I}(x,y,\varphi,\psi) \left(\iint_{(\alpha,\beta)} \boldsymbol{L}(x,y,\varphi-\alpha,\psi-\beta)\mathrm{d}\alpha\mathrm{d}\beta \right) \cos\xi \mathrm{d}\Omega_R \mathrm{d}A_R
\end{aligned}$$

where the integral

$$\iint_{(\alpha,\beta)} \boldsymbol{L}(x,y,\varphi-\alpha,\psi-\beta)\mathrm{d}\alpha\mathrm{d}\beta = \boldsymbol{S}(x,y,\varphi,\psi)$$

is the irradiance of the source per unit area at the entrance pupil as function of the source angular position expressed with the reference system angles (φ, ψ). In fact, we have found that

$$\iint_{(\alpha,\beta)} R^{(tot)}(\alpha,\beta)\mathrm{d}\alpha\mathrm{d}\beta = \int_{A_R}\int_{\Omega_{FoV}} \mathbf{V_I}(x,y,\varphi,\psi)\boldsymbol{S}(x,y,\varphi,\psi)\cos\xi \mathrm{d}\Omega_R \mathrm{d}A_R.$$

If the instrument is illuminated by a collimated test beam with uniform irradiance and a diameter big enough to fill the entrance pupil, $\boldsymbol{S}(x, y, \varphi, \psi)$ becomes independent on (x, y). Moreover, if the instrument Field of view is small enough, the irradiance of the collimated beam can be also considered independent[12] on the angle (φ, ψ) and then $\boldsymbol{S}(x, y, \varphi, \psi) = \boldsymbol{S}_0$. With these hypotheses we have

$$\iint_{(\alpha,\beta)} R^{(tot)}(\alpha,\beta)\mathrm{d}\alpha\mathrm{d}\beta = \int_{A_R}\int_{\Omega_{FoV}} \mathbf{V_I}(x,y,\varphi,\psi)\cos\xi \mathrm{d}\Omega_R \mathrm{d}A_R\, \boldsymbol{S}_0 = \mathbf{G}_{eff}\, \boldsymbol{S}_0.$$

If the instrument efficiency can be considered independent on the instrument field of view position and the instrument entrance pupil position then,

$$\iint_{(\alpha,\beta)} R^{(tot)}(\alpha,\beta)\mathrm{d}\alpha\mathrm{d}\beta = G_r \boldsymbol{\eta_I}\, \boldsymbol{S}_0. \tag{2.26}$$

[12] If the field of view is big, the irradiance is dependent on the projected entrance pupil area as discussed in the subsection 2.3.4. For the PHEBUS case the field of view is about $0.1° \times 2°$ which is small enough to consider $\cos 2° \simeq 1$.

The source irradiance $\boldsymbol{S}_0$ can be measured with a calibrated detector in front of which a well-known mask is used to define precisely the detector collecting area. In additional, also the polarization state of the collimated test beam can be easily characterized. The continuous integral

$$\iint_{(\alpha,\beta)} R^{(tot)}(\alpha,\beta)\mathrm{d}\alpha\mathrm{d}\beta$$

can be evaluated as a discrete sum by mapping the field of view with the defined steps $\Delta\alpha$ and $\Delta\beta$. For each position (α_i, β_j) mapped, the instrument counts $R^{(tot)}(\alpha_i, \beta_j)$ are measured and the integral can be approximated by the relationship

$$\iint_{(\alpha,\beta)} R^{(tot)}(\alpha,\beta)\mathrm{d}\alpha\mathrm{d}\beta \simeq \Delta\alpha\Delta\beta \sum_{i,j} R^{(tot)}(\alpha_i,\beta_j).$$

Finally, from the relation 2.26 we have

$$G_r = \frac{\iint_{(\alpha,\beta)} R^{(tot)}(\alpha,\beta)\mathrm{d}\alpha\mathrm{d}\beta}{\boldsymbol{\eta_I}\,\boldsymbol{S}_0} \simeq \frac{\Delta\alpha\Delta\beta\sum_{i,j} R^{(tot)}(\alpha_i,\beta_j)}{\boldsymbol{\eta_I}\,\boldsymbol{S}_0} \tag{2.27}$$

2.3.4 Punctual source: the real collecting area and effective area

If the optical instrument has been conceived for observing objects far away, like stars, the radiation light arrives to the instruments as a plane wave. This circumstance can occur also for a space instrument designed to observe extended sources: e.g. in common practice, the stars are usually used as source during the in-flight calibrations.
A source far away can be assimilated, from an optical point of view, as a punctual source at the infinity and it is characterizes in term of its irradiance S which usually can be considered constant. With a similar procedure followed in the previous section, we can define three geometrical factors that determine the instrument response during punctual source observations. Referring to Figure 2.10, let us consider an ideal lossless instrument. The total radiant power collected by an infinitesimal element area of the entrance pupil is

$$d\Phi = dA_R \cos\xi\, S \quad \text{where } dA_R\cos\xi = dA_R^{(proj)}$$

and the total power flux collected by the entire entrance pupil A_R is[13]

$$\Phi = \int_{A_R} S\cos\xi\, dA_R = S\cos\xi \int_{A_R} dA_R = S\, A_R^{(proj)}$$

[13] We wish to point out that for a punctual source also the angle ξ is independent to the infinitesimal element position and then $\cos\xi$ is a constant.

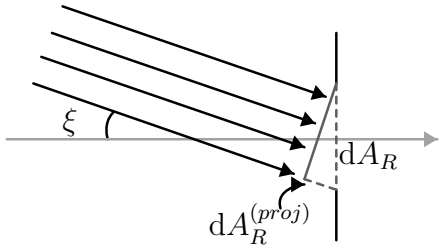

Figure 2.10. Radiant flux coming from a punctual source collected by an infinitesimal element of the instrument entrance window. The projected area is indicated with $\mathrm{d}A_R^{(proj)}$.

where A_R is the entrance pupil area. For a real instrument, the efficiency of the optical element, the vignetting and the misalignment can be considered in the total power flux computation adopting the instrument efficiency $\eta(x, y)$ and the vignetting function $V(x, y)$:

$$\Phi = S \cos\xi \int_{A_R} \eta(x, y) V(x, y)\, dA_R.$$

As discussed previously, the instrument efficiency can be still considered as a constant with respect to the pupil position and we obtain

$$\Phi = S\eta_0 \cos\xi \int_{A_R} V(x, y)\, dA_R = S\eta_0 A_r^{(\xi)} = S A_{eff}^{(\xi)}$$

where we have defined, respectively, the *real collecting area* and the *effective collecting area* of the instrument as

$$\begin{aligned} A_r^{(\xi)} &= \cos\xi \int_{A_R} V(x, y)\, dA_R \\ A_{eff}^{(\xi)} &= \eta_0 A_r^{(\xi)} \end{aligned} \tag{2.28}$$

Finally, if the source is polarized or partially polarized, the instrument behavior is described by the Stokes-Mueller formalism as discussed in section 2.2 and both the simple efficiency η_I and effective collecting area $A_{eff}^{(\xi)}$ become a vector of four coefficients defined as

$$\begin{aligned} \boldsymbol{\eta_I} &= \mathbf{D}\,\mathbf{M_I} \\ \mathbf{A}_{eff}^{(\xi)} &= A_r^{(\xi)}\,\mathbf{D}\,\mathbf{M_I} \end{aligned}$$

where $\mathbf{D}$ is detector transformation and $\mathbf{M_I}$ is the Mueller matrix of the optical instrument.
If $\boldsymbol{S}$ is the Stokes vector which described the polarization state of the punctual

source observed by our optical instrument, the total output signal viewed by the instrument can be estimated as

$$R^{(tot)} = A_r^{(\xi)} \mathbf{DM_I} \boldsymbol{S} = \mathbf{A}_{eff}^{(\xi)} \boldsymbol{S} \tag{2.29}$$

The last relationship suggests us also an operative procedure to measure the real collecting area: if the instrument is illuminated with a uniform collimated beam described by the Stokes vector $\boldsymbol{S}$ and well alligned with the entrance pupil (with $\xi = 0°$), from the 2.29 we have

$$A_r^{(\xi=0°)} = \frac{R^{(tot)}}{\boldsymbol{\eta_I} \boldsymbol{S}} = \frac{R^{(tot)}}{\mathbf{DM_I} \boldsymbol{S}}.$$

2.3.5 Numerical simulations of PHEBUS geometric factors

With the paraxial approximation, we can compute the geometrical factors of PHEBUS. From the optical design we have an entrance pupil diameter $\Phi = 25.4\,\text{mm}$ and a field of view of about $0.18\,\text{deg}^2$, as computed in Chapter 1. From the mechanical design of the instrument, we also know that between the two grating is foreseen a gap of 1 mm and a consequent dead area of $A_d = 1 \times 42 = 42\,\text{mm}^2$ (42 mm is the height of the gratings). Then, for each channel we have

$$A_r^{(\xi=0°)} = \frac{g}{2} \frac{\pi \Phi^2}{4} = 232.3\,\text{mm}^2$$

where the parameter g takes into account the dead area between the two gratings[14] and it is defined as

$$g = \frac{\frac{\pi \Phi^2}{4} - A_d}{\frac{\pi \Phi^2}{4}} = 0.917$$

Finally, considering the filed of view computed in Chapter 1, we have

$$G_r = A_r^{(\xi=0°)} \Omega_{FoV} = 12737 \cdot 10^{-6}\,\text{mm}^2\text{sr}$$

However, the calculation of this factors with the paraxial approximation doesn't take into account the aberration effects and eventual vignetting effects presented in the spectrometer. A more detailed computation of the geometric factors $A_r^{(\xi)}$ and G_r has been performed by using the ray-trace software ZEMAX as described in the calibration document [49]. For the $A_r^{(\xi)}$ computation the entrance pupil of the instrument has been filled by uniformly distributed rays chosen parallel to the

[14] The term $\frac{g}{2}$ in the relationship accounts that the initial beam is separated into two parts between the EUV and FUV channels.

optical axis (angle $\xi = 0$); the number of rays impacting the detector without being vignetted, divided by the number of incoming rays, and multiplied by the area of the entrance pupil, gives the real collecting area $A_r^{(\xi=0^\circ)}$ of the channel under investigation[15] . Similarly, for the extended sources case, the incoming rays are chosen uniformly distributed inside a solid angle of the Field of View of the system, and uniformly distributed inside the entrance pupil. The ratio between the unvignetted rays and the total rays multiplied by the solid angle of the incoming rays and by the entrance pupil area is a good estimation of the G_r for the channel under investigation.
From the data analysis, it appeared that the geometric factors $A_r^{(\xi=0^\circ)}$ and G_r are dependent to the position of the scanning angle θ and the dependence can be well described in every configuration by the simple sine law

$$Z = X + Y \sin\theta \tag{2.30}$$

where X and Y are two parameters defined by the configuration; in table 2.2 are reported the factors required for the estimation of $A_r^{(\xi=0^\circ)}$ and G_r.

Z		X	Y
$A_r^{(\xi=0^\circ)}$	EUV channel	$231.79\,\mathrm{mm}^2$	$4.69\,\mathrm{mm}^2$
	FUV channel	$231.79\,\mathrm{mm}^2$	$-4.69\,\mathrm{mm}^2$
G_r	EUV channel	$12846 \cdot 10^{-6}\,\mathrm{mm}^2\mathrm{sr}$	$-796 \cdot 10^{-6}\,\mathrm{mm}^2\mathrm{sr}$
	FUV channel	$12844 \cdot 10^{-6}\,\mathrm{mm}^2\mathrm{sr}$	$-794 \cdot 10^{-6}\,\mathrm{mm}^2\mathrm{sr}$

Table 2.2. The parameters X and Y required for estimating the the geometric factors of PHEBUS using the sine law 2.30.

As we can see, the terms X are very close to those calculated with the paraxial approximation. However, we have found an additional dependence on the scanning angle θ through the term Y: in fact, the optical geometry of the instrument changes when the baffle rotates and then also the aberrations introduced by the entrance mirror rotate with respect to the entrance slit. With a similar procedure, also the real Étendue with the entrance slit removed has been computed. We have found the same law of 2.30 with $X = 298.33 \cdot 10^{-3}\,\mathrm{mm}^2\mathrm{sr}$ and $Y = -14.9 \cdot 10^{-3}\,\mathrm{mm}^2\mathrm{sr}$ for both channels. With the paraxial approximation, the field of view of the instrument becomes about $3^\circ \times 1.4^\circ \simeq 4.3\,\mathrm{deg}^2$ and we obtain $G_r \simeq 304.3 \cdot 10^{-3}\,\mathrm{mm}^2\mathrm{sr}$.

[15] The general real collecting area can be computed with the relationship

$$A_r^{(\xi)} = A_r^{(\xi=0^\circ)} \cos\xi.$$

Finally, we point out that the geometrical parameters computed with the paraxial approximation or with the ray-trace procedure don't take into account the stray-light or optical-components misalignment effects which can significantly change these quantities [25]. For these reasons, a well modelling of the instrument geometry can be achieved by an experimental characterization.

2.4 The full radiometric model for PHEBUS

Given the Stokes vector of an extended source $\boldsymbol{L} = \begin{pmatrix} L_0 & L_1 & L_2 & L_3 \end{pmatrix}^T$ in terms of radiance and considering the approximations discussed in section 2.2, the count rate of PHEBUS for a generic channel is:

$$\begin{aligned} R^{(tot)} &= \mathbf{G}_{eff}\boldsymbol{L} = G_r\boldsymbol{\eta}_I\boldsymbol{L} = G_r\mathbf{DM}_{PHEBUS}\boldsymbol{L} = \\ &= G_r\eta_d\left(m_{11}L_0 + m_{12}L_1 + m_{13}L_2 + m_{14}L_3\right) \simeq \\ &\simeq \eta_d\left(X + Y\sin\theta\right)\left(m_{11}L_0 + m_{12}L_1\right) \end{aligned} \tag{2.31}$$

where the values of X and Y are reported in Table 2.2 and the values of m_{11} and m_{12} can be computed using the relations 2.13; for example, in Figure 2.11 are reported the m_{11} and m_{12} parameters for the scanning angle $\theta = 45°$. The equation 2.31 can be re-arranged as

$$R^{(tot)} \simeq G_r\eta_d m_{11}L_0\left(1 + M_{12}\frac{L_1}{L_0}\right), \quad M_{12} = \frac{m_{12}}{m_{11}}$$

and we can deduce that the degree of polarization of the source must be known a priori. The calibration give us the values $G_r\eta_d m_{11}$ and M_{12}, thus we can deduce the value of L_0 starting from $R^{(tot)}$ and the ratio L_1/L_0. Furthermore, the term $G_r\eta_d m_{11}$ can be assimilated to the Effective Étendue G_{eff} for unpolarized light. The term inside brackets represents a correction factor of G_{eff} taking into account the incident polarization state and the polarization response of the instrument. It can be also seen as an error factor if the polarization effects are not taken into account.

Similarly, given the Stokes vector of an punctual source $\boldsymbol{S} = \begin{pmatrix} S_0 & S_1 & S_2 & S_3 \end{pmatrix}^T$ in terms of irradiance, the count rate of PHEBUS is:

$$\begin{aligned} R^{(tot)} &= \mathbf{A}^{(\xi)}_{eff}\boldsymbol{S} = A^{(\xi)}_r\boldsymbol{\eta}_I\boldsymbol{S} = A^{(\xi)}_r\mathbf{DM}_{PHEBUS}\boldsymbol{S} = \\ &= A^{(\xi)}_r\eta_d\left(m_{11}S_0 + m_{12}S_1 + m_{13}S_2 + m_{14}S_3\right) \simeq \\ &\simeq \eta_d\cos\xi\left(X + Y\sin\theta\right)\left(m_{11}S_0 + m_{12}S_1\right) \end{aligned}$$

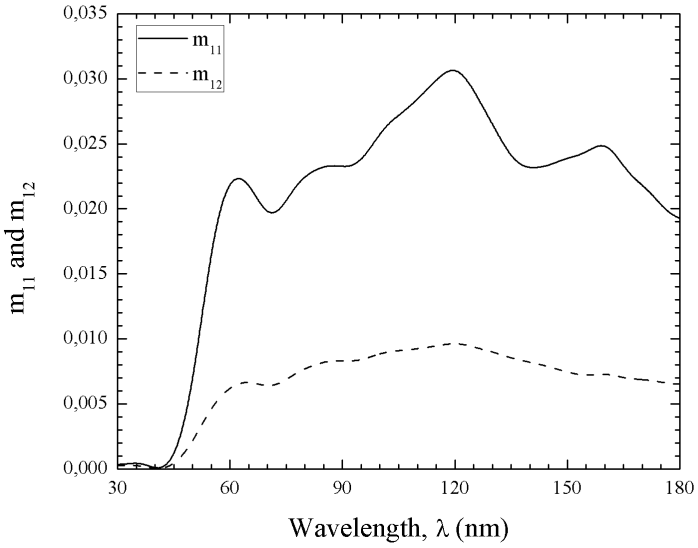

(a)

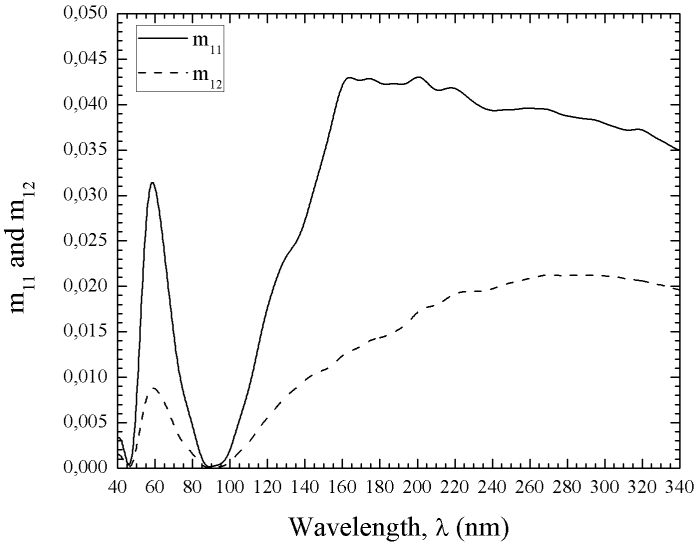

(b)

Figure 2.11. The parameters m_{11} and m_{12} of the Mueller matrix of PHEBUS with a scanning angle $\theta = 45°$; in Figure 2.11(a) the coefficients are computed for the EUV channel while in Figure 2.11(b) are computed for the FUV channel.

Chapter 3

The optical sub-systems calibrations

In Chapter 2 the radiometric model of an optical instrument was discussed in term of radiometric function and the results were applied onto the spectrometer PHEBUS. After the assumption of the polarization independence of the detector, the radiometric function of PHEBUS for an extended source becomes

$$\begin{aligned} R^{(tot)} &= G_r \mathbf{DM}_{PHEBUS} \boldsymbol{L} = \\ &= \eta_d G_r \left(m_{11} L_0 + m_{12} L_1 + m_{13} L_2 + m_{14} L_3 \right) \ . \end{aligned} \tag{3.1}$$

From equation 3.1 we can note that if we want to determine the radiometric function with experimental measurements, we need to measure the six parameters

$$\eta_d, \qquad G_r, \qquad m_{11}, \qquad m_{12}, \qquad m_{13} \quad \text{and} \quad m_{14}.$$

Furthermore, the efficiency of the detector η_d is always determined when the flight model of the detector is built and characterized; thus, it remains to measure five parameters: the first row of the instrument Mueller matrix and the geometrical coefficient of the instrument G_r[1]. As it can be observed from the equations 2.13, the first row of the PHEBUS Mueller matrix depends on the pure reflectance or efficiency of the optical components[2]. In fact, these parameters can be experimentally retrieved also only with the subsystems-level characterization which is easier and more convenient than an instrument-level characterization.

The subsystem characterizations have been performed for the Qualification Model (QM) and Flight Model (FM) optical subsystems and the measurements have been performed in vacuum because the Extreme Ultra Violet (EUV) range doesn't propagate in air. In the first section of this Chapter the experimental facility used in the

[1] If the punctual source case is discussed, the geometrical parameter is $A_r^{\xi=0^\circ}$.

[2] This is also valid for a generic optical instrument.

subsystems characterization is rather described from a theoretical point of view and experimentally characterized. In the second section, the results obtained from the subsystems characterization are discussed, compared with the theoretical previsions expected and used to compute the first row of the PHEBUS Mueller matrix. Finally, in the last section are reported also the characterization of the backup entrance mirror samples obtained using synchrotron radiation.

3.1 The FUV/EUV reflectometer facility

The PHEBUS optical sub-systems were tested in the normal-incidence reflectometer at the CNR-IFN UOS Padova laboratory. The facility is composed by four parts: the source, the monochromator, the focusing section and the experimental chamber; An image and an opto-mechanical sketch of the reflectometer facility are shown in Figure 3.1. The lamp used as source is connected to the input of the monochromator by the entrance slit. The monochromator is composed by a toroidal grating $f/10$ with 600 grooves/mm and coated by Platinum. The spectral resolution improvement is obtained with an additional output slit placed in order to fix the subtended angle α between entrance and exit slit at about 25°. The height of both slits is 3 mm and the width is adjustable from zero to 650 μm by a micrometer. A step by step motor rotates the grating following a *Johnson-Onaka configuration* [50] in order to select at the output slit the desired wavelength. With this arrangement, the reflectometer can work from about 30 nm up to the visible range.
After the output slit, a gate valve can isolate the monochromator chamber from the following hexagonal chamber in which is placed a toroidal mirror coated by platinum. This mirror focuses the light coming from the output slit to the center of the experimental chamber. The sample under characterization is placed in a support which runs along a sled fixed to the bottom of chamber by a rotating micrometer mechanism. An additional rotating micrometer mechanism is used to place the detector in order to perform reflectance measurements in θ-2θ configuration, with varied incidence angles. The reflectometer is served by a vacuum system composed by two primary pumps (scroll pumps) and two secondary pumps (turbo-molecular pumps) which reach an high vacuum up to 10^{-7} mbar of pressure, avoiding the absorption of the EUV radiation by the air.

3.1.1 The sources

The choice of the radiation sources to be used for the calibration activities is an important aspect because the PHEBUS working range is large and we need to test different wavelengths as much as possible; in Table 3.1 are shown the sources and the wavelengths used for the subsystems calibration activities. In the following the

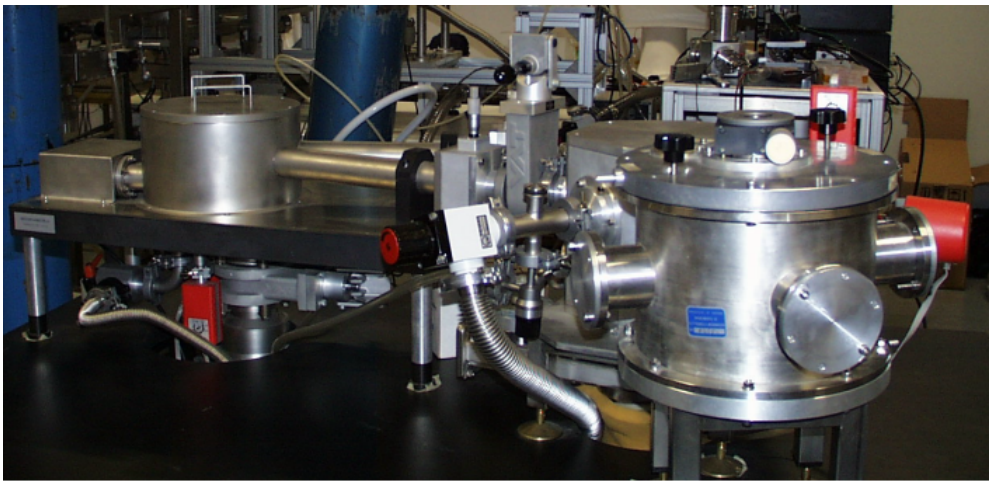

(a)

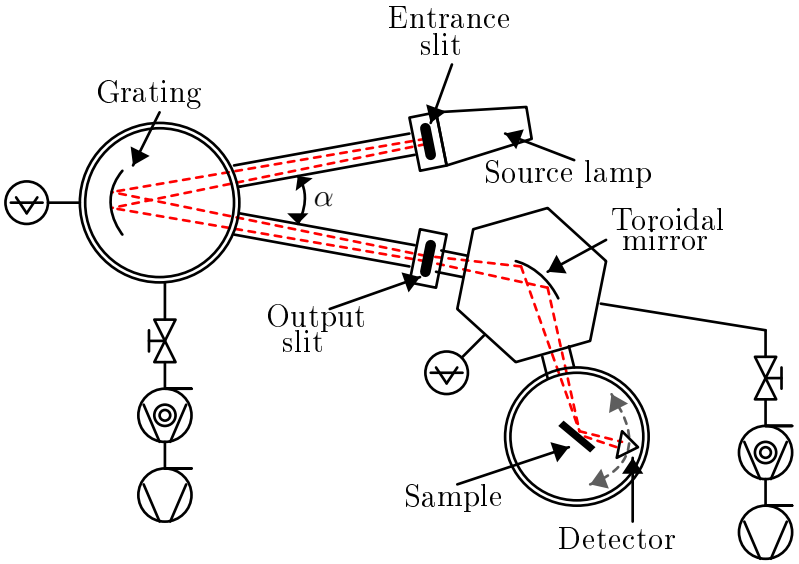

(b)

Figure 3.1. The FUV-EUV normal incidence reflectometer used in the subsystem calibration. In Figure 3.1(a) is shown a picture of this facility while in Figure 3.1(b) is shown an opto-mechanical sketch.

main sources are briefly discussed referring to specific literature for a more detailed description.

Wavelength	Source	Element	Detector
30.4 nm	Hollow Cathode	He	CEM
46.1 nm	Hollow Cathode	Ne	CEM
58.4 nm	Hollow Cathode	He	CEM
73.6 nm	Hollow Cathode	Ne	CEM
74.4 nm	Hollow Cathode	Ne	CEM
91.9 nm	Hollow Cathode	Ar	CEM
102.5 nm	Hollow Cathode	He	CEM
106.6 nm	Hollow Cathode	Ar	CEM
121.6 nm	Deuterium lamp	D	CEM
123.3 nm	Deuterium lamp	D	CEM
140.0 nm	Deuterium lamp	D	CEM
160.0 nm	Deuterium lamp	D	CEM
253.1 nm	Mercury vapor lamp	Hg	PMT
264.8 nm	Mercury vapor lamp	Hg	PMT
279.9 nm	Mercury vapor lamp	Hg	PMT
296.3 nm	Mercury vapor lamp	Hg	PMT
302.2 nm	Mercury vapor lamp	Hg	PMT
312.7 nm	Mercury vapor lamp	Hg	PMT

Table 3.1. A list of the wavelengths used during the subsystem calibration activities with the sources and detectors used; the acronym CEM is *Channel Electron Multiplier* while PMT is *Photo-Multiplier Tube*. See the subsection 3.1.2 for more details.

Hollow-cathode lamp:

For the EUV range we adopted an *Hollow-Cathode* lamp [51, 52] filled by the classical noble gases like Argon (Ar), Neon (Ne) or Helium (He). An HCL usually consists of a glass tube in which two terminals act as cathode (with a shape of hollow cylinder) and anode. The tube is filled by the desired gas and a large voltage (of about $1000 - 2000$ V, depending on the geometry and the gas pressure) across the anode and cathode causes a ionization and a plasma channel formation. The gas ions are accelerated into the cathode and sputter off atoms from it. Both the gas ions and the sputtered cathode atoms are excited by collisions with other atoms/particles in the plasma and during the decay process photons are emitted with a lines structure according to the gas used.

Deuterium lamp:

In order to cover the range above 115 nm, a *Deuterium lamp* has been also used [52]. A deuterium lamp uses a tungsten filament and an anode placed on the opposite sides of a nickel box structure with a restrictive aperture. An arc of several hundred milliampere is created from the filament to the anode through the box structure restrictive aperture: the discharge is similar that occurs in an arc lamps. The arc excites the molecular deuterium contained within the bulb to a higher energy state and then light is emitted when the excited deuterium transitions back to its initial state. The filament requires high temperature to operate and for this reason is heated for approximately twenty seconds before the lamp usage; once the arc is created the discharge process heats itself the lamp filament. The lamp casing is usually realized with fused quartz, UV glass, or magnesium fluoride depending on the specific usage and the working temperatures foreseen.

The mercury-vapor lamp:

A mercury-vapor lamp is a gas discharge lamp that uses an electric arc through vaporized mercury to produce light [53]. The arc discharge is generally confined to a small fused quartz arc tube with two primary electrodes. This arc tube is also mounted within a larger isolation tube made with different materials depending on the lamp usage.
At the normal temperature, the mercury in the arc tube is liquid and no discharges between the two main electrodes can occur. The mercury is vaporized with a starter mechanism consisting of a third additional electrode, named "starting electrode", mounted near one of the main electrodes and connected through a resistor to the other main electrode. The tube with mercury is also filled by argon gas at low pressure in order to create a small arc between the starting electrode and the adjacent main electrode when a proper voltage is applied. This starting discharge heats the mercury and eventually provides enough ionized mercury to strike an arc between the two main electrodes; this process takes from about 5 minutes. Some bulbs include a thermal switch which shorts the starting electrode to the adjacent main electrode, extinguishing the starting arc, once the main arc strikes.

3.1.2 The detectors

In the reflectometer facility two different detectors were adopted: the photo-multiplier tube working in the wavelength range above the 200 nm, where the radiation can propagate also in air, and the channel electron multiplier (CEM) working in the range below to 200 nm, where the radiation can propagate only in vacuum. In the following, a brief description of the two detectors is given, referring to specific

literature for more detailed information.

The photo-multiplier tube:

Photo-multiplier tubes (or PMTs), is an extremely sensitive detector of light in the ultraviolet, visible, and near-infrared ranges [54]. These detectors can multiply the photo-emitted electrons produced by incident light up to about 100 million times (i.e., 160 dB) and then also the radiation with very low flux can be detected.
A photo-multiplier has a glass envelope with high vacuum inside, which houses a photo-cathode, the electron multiplier stage and an anode. Incident photons strike the photo-cathode material, which is present as a thin layer on the entrance window of the device, and electrons are produced for photoelectric effect. These electrons are directed by a focusing electrode toward the electron multiplier stage, where electrons are multiplied by a secondary emission process. This electron multiplier stage consists of a number of electrodes called dynodes; each dynode is held at a more positive voltage, of about 100 V, than the previous one. When the primary electrons leave the photo-cathode, they have the energy of the incoming photon minus the work function of the photo-cathode and they are accelerated by the electric field applied toward the first dynode. Upon striking the first dynode, more low energy electrons are emitted, and these electrons in turn are accelerated toward the second dynode. The geometry of the dynode chain is such that a cascade occurs with an ever-increasing number of electrons being produced at each stage. For example, if at each stage an average of 4 new electrons are produced for each incoming electron, and if there are 12 dynode stages, then at the last stage one expects for each primary electron about $5^{12} \simeq 10^8$ electrons. This large number of electrons reaching the last stage, called the anode, results in a current that is easily detectable. In Figure 3.2(a) is reported a sketch which summarized the working principle of the photon-multiplier tube.
During the calibration activities was used the HAMAMATSU R6352 photo-multiplier tube [55] directly connected to the Keithley 617 femto-amperometer.

The channel electron multiplier (CEM):

A channel electron multiplier is a compact continuous dynode electron multiplier system that can detect Electrons, Ions, EUV radiation, Soft X-rays, and other Nuclear Particles at rates greater than one million events per second [56, 57]. The primary incoming radiation passes through the inlet funnel-shaped aperture and strikes the surface of the channel electron multiplier. This surface is coated by and high secondary emissive semi-conductive material and if the radiation energy or the ion collision energy is sufficient, at least one electron is ejected from the CEM wall.

The ejected electrons are accelerated into the interior of the CEM by the local electric field obtained by a bias voltage. If the magnitude of the bias voltage is sufficient, the accelerated electrons acquire enough energy to trigger more secondaries when they strike the CEM surface again. This process continues down the length of the CEM, striking the CEM surface many times, each time generating more and more secondaries. At the end of the CEM channel, a charge collector collects the electrons obtaining a detectable current. In Figure 3.2(b) is reported a sketch which summarized the working principle of the CEM. A single photon or particle input event can trigger an output electron avalanche of more than 10^7 electrons.
During the calibration activities was used the AMPEKTRON MD-501 CEM [57].

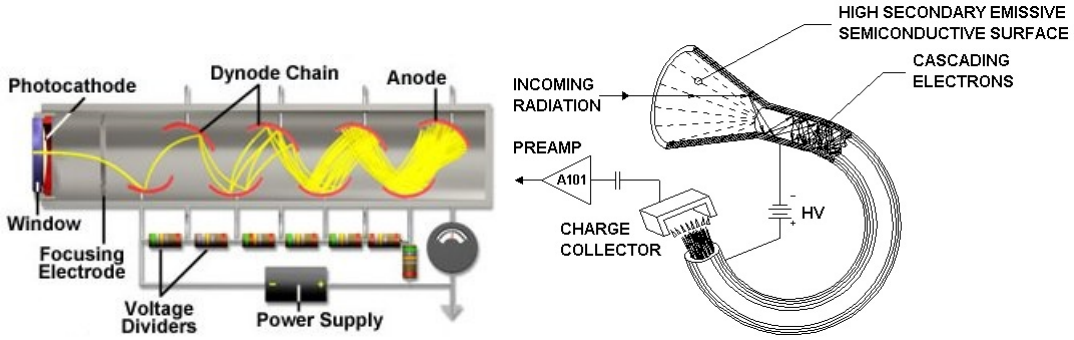

(a) (b)

Figure 3.2. The working principle of the detectors used in subsystem calibration activities: in Figure 3.2(a) the photo-multiplier tube and in Figure 3.2(b) the channel electron multiplier.

3.1.3 Polarization state of the reflectometer test beam

Adopting the Stokes-Mueller formalism, the polarization state of the test beam obtained with the normal incident reflectometer facility can be analyzed. With the reference of Figure 3.1(b), the light emitted from the source encounters the toroidal grating and the focusing toroidal mirror. The equivalent Mueller matrix of the reflectometer facility is

$$\begin{aligned}\mathbf{M}_R &= \mathbf{M}_{mirror}\,\mathbf{M}_{grating} = \\ &= \begin{pmatrix} A_gA_m + B_gB_m & A_gB_m + B_gA_m & 0 & 0 \\ A_gB_m + B_gA_m & A_gA_m + B_gB_m & 0 & 0 \\ 0 & 0 & C_mC_g - D_mD_g & C_mD_g + D_mC_g \\ 0 & 0 & -C_mD_g - D_mC_g & C_mC_g - D_mD_g \end{pmatrix}\end{aligned} \tag{3.2}$$

in which the subscript g refers to the monochromator grating, m refers to the toroidal focusing mirror[3] and

$$\begin{aligned} A_g &= \frac{|r_x^{(g)}|^2 + |r_y^{(g)}|^2}{2} & A_m &= \frac{|r_x^{(m)}|^2 + |r_y^{(m)}|^2}{2} \\ B_g &= \frac{|r_x^{(g)}|^2 - |r_y^{(g)}|^2}{2} & B_m &= \frac{|r_x^{(m)}|^2 - |r_y^{(m)}|^2}{2} \\ C_g &= 2\,\mathrm{Re}\left(r_x^{(g)} r_y^{(g)*}\right) & C_m &= 2\,\mathrm{Re}\left(r_x^{(m)} r_y^{(m)*}\right) \\ D_g &= 2\,\mathrm{Im}\left(r_x^{(g)} r_y^{(g)*}\right) & D_m &= 2\,\mathrm{Im}\left(r_x^{(m)} r_y^{(m)*}\right) \end{aligned}$$

where $|r_x^{(m,g)}|^2$ is the TE reflectance and $|r_y^{(m,g)}|^2$ is the TM reflectance.
The hollow-cathode lamp as well as the deuterium lamp or the mercury lamp emits unpolarized light and then the Stokes vector expressed in term of radiance is

$$\boldsymbol{L}_{lamp} = \begin{pmatrix} L_0 \\ 0 \\ 0 \\ 0 \end{pmatrix}$$

and, considering the relation 3.2, we have

$$\boldsymbol{L}_{test} = \mathbf{M}_{reflect}\,\boldsymbol{L}_{lamp} = L_0 \begin{pmatrix} A_g A_m + B_g B_m \\ A_g B_m + B_g A_m \\ 0 \\ 0 \end{pmatrix} = L_0\,(A_g A_m + B_g B_m) \begin{pmatrix} 1 \\ P \\ 0 \\ 0 \end{pmatrix} \tag{3.3}$$

where P is the *polarization factor* of the reflectometer facility[4]. Considering a uniform radiance along the entrance slit of the monochromator and using the definition of the polarization factor and the Stokes parameters, we find

$$P = \frac{L_1}{L_0} = \frac{|E_x|^2 - |E_y|^2}{|E_x|^2 + |E_y|^2} \tag{3.4}$$

[3] In the scheme shown in Figure 3.1(b), the planes of incidence of the grating and the mirror coincide. The misalignment between the two planes of incidence can be taken into account with the relationship

$$\mathbf{M}_R = \mathbf{M}_{mirror}\,\mathbf{M}(\xi)\,\mathbf{M}_{grating}$$

where $\mathbf{M}(\xi)$ is the matrix of a rotator element with the rotation angle ξ; if ξ is small the $\mathbf{M}(\xi) \simeq \mathbf{I}$.

[4] From equation 3.3 could seem that the polarization factor is defined as a ratio between positive terms because usually we have $|r_x|^2 \geq |r_y|^2$. However, this last condition is not valid for a grating because it always presents, starting from a specific wavelength, an *inversion point* from which we have $|r_x|^2 \leq |r_y|^2$.

where E_x is the TE component and E_y is the TM component of the electric field.

The characterization of the polarization factor of the reflectometer facility is a pivotal step before starting the subsystem calibration measurements. In fact, if only the unpolarized reflectance of an optical component is required, the polarization factor of the facility doesn't affect the characterization because the unpolarized reflectance can be simply retrieved with the arithmetic average between the values measured at two experimental chamber configurations, placed at 90° one to each other (see Figure 3.3). However, if the reflectance for the TE and TM configurations are required, the polarization factor P has to be known in order to extrapolate the information starting from the two measurements performed with our facility.

In order to fix this concept, let us imagine to measure the reflectance of an optical

(a) (b)

Figure 3.3. The two configuration of the reflectometer experimental chamber. In Figure 3.3(a) is shown the *up-configuration* while in Figure 3.3(b) is shown the *down-configuration* obtained by a rotation of 90° with respect to the up-configuration.

subsystem using the reflectometer facility described before. In the first configuration (see Figure 3.3(a)), which is called *up-configuration*, we measure with the detector the direct beam and the reflected beam and we compute the reflectance in up-configuration as

$$R^{(up)} = \frac{I_{reflected}}{I_{direct}}$$

where $I_{reflected}$ is the detector signal when the reflected beam is measured and I_{direct} is the detector signal when the direct beam is measured. With the same procedure, the experimental chamber is rotated of 90° reaching the *down-configuration* and the reflectance $R^{(down)}$ is measured (see Figure 3.3(b)). From the polarization factor of

the reflectometer test beam defined by the relationship 3.4, we can write

$$\begin{cases} R^{(up)} = |r_x|^2 P + (1-P)\dfrac{|r_x|^2 + |r_y|^2}{2} \\ R^{(down)} = |r_y|^2 P + (1-P)\dfrac{|r_x|^2 + |r_y|^2}{2} \end{cases} \quad \text{for } P > 0$$

and

$$\begin{cases} R^{(up)} = |r_y|^2 |P| + (1-|P|)\dfrac{|r_x|^2 + |r_y|^2}{2} \\ R^{(down)} = |r_x|^2 |P| + (1-|P|)\dfrac{|r_x|^2 + |r_y|^2}{2} \end{cases} \quad \text{for } P < 0$$

where $|r_x|^2$ and $|r_y|^2$ are the TE and TM reflectances of the sample under test, respectively[5]. In fact, with the first equation we say that the part P of the test beam energy is linearly polarized and reflected by the sample in a TE configuration (or TM if $P < 0$) while the remaining part $1 - P$ of the energy is unpolarized. Similarly, with the second equation we say that when the chamber is rotated of 90°, the linearly polarized part of the test beam is now reflected by the sample in a TM configuration (or TE if $P < 0$).
Solving the systems for $|r_x|^2$ and $|r_y|^2$, after some algebraic manipulations we find the general relationships

$$\begin{aligned} |r_x|^2 &= \frac{R^{(up)} + R^{(down)}}{2} + \frac{R^{(up)} - R^{(down)}}{2P} \\ |r_y|^2 &= \frac{R^{(up)} + R^{(down)}}{2} - \frac{R^{(up)} - R^{(down)}}{2P} \end{aligned} \tag{3.5}$$

which allow us to compute the TE and TM reflectances of the sample starting from the two measurements performed in our reflectometer facility and knowing the polarization factor P of the test beam.

The experimental characterization of the polarization factor P has been performed following the these three steps:

1. The reflectance of a well-known sample (an reference Au mirror for the EUV range and a Silicon wafer for the FUV range) is measured for different incidence angles in two experimental chamber configurations, one at 90° to each other;

[5] We point out that the polarization factor P of the facility is defined considering the planes of incidence of the toroidal grating and the focusing toroidal mirror and it is independent on the chamber rotation.

2. The arithmetical average between the reflectances obtained from measurements are fitted optimizing the optical constants and the surface roughness (also checked with AFM measurements on the reference samples);

3. The reflectances measured at each chamber configuration are fitted optimizing the polarization factor of the incident beam and adopting the roughness and optical constants values retrieved in the previous step.

In Figure 3.4 are reported as example two fits of the reference samples reflectance used to retrieve the polarization factor of the facility: the first one is at 70.4 nm with gold reference mirror and the second one is at 302.2 nm with Silicon substrate reference. In Table 3.2 the experimental polarization factors of the facility retrieved for the wavelengths in Table 3.1 are reported with the error associated to the determination procedure.

Wavelength	Polarization factor P	Error ΔP
30.4 nm	0.40	0.02
46.1 nm	0.48	0.02
58.4 nm	0.53	0.03
73.6 nm	0.59	0.03
74.4 nm	0.59	0.03
91.9 nm	0.73	0.04
102.5 nm	0.85	0.06
106.6 nm	0.82	0.04
121.6 nm	0.90	0.05
123.3 nm	0.90	0.05
140.0 nm	0.91	0.05
160.0 nm	0.92	0.05
253.1 nm	−0.38	0.02
264.8 nm	−0.68	0.03
279.9 nm	−0.82	0.04
296.3 nm	−0.70	0.04
302.2 nm	−0.75	0.04
312.7 nm	−0.63	0.03

Table 3.2. The experimental polarization factors of the EUV-FUV reflectometer facility obtained for the wavelengths reported in Table 3.1.

The uncertainty associated to the polarization factor measurements is given by the contribution of systematic errors, the non-perfectly uniformity of the detector sensitive area, the small fluctuations of the source radiance and possible small set-up misalignments. In order to take into account all these contributions, the uncertainty has been estimated evaluating the polarization factor measurement repeatability.

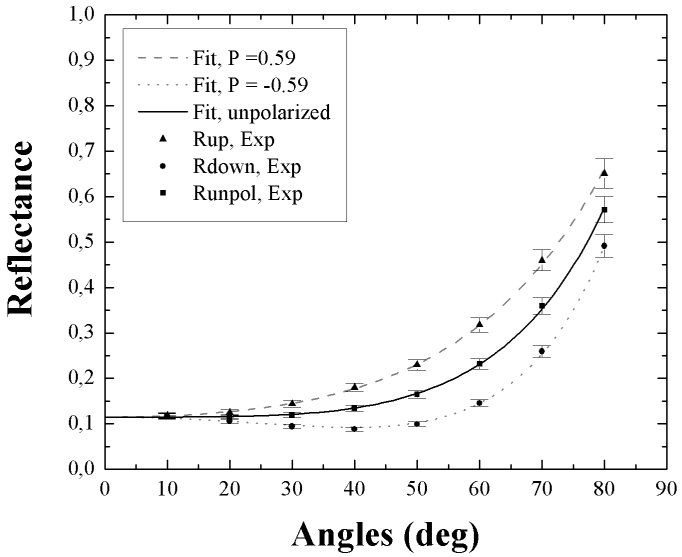

(a)

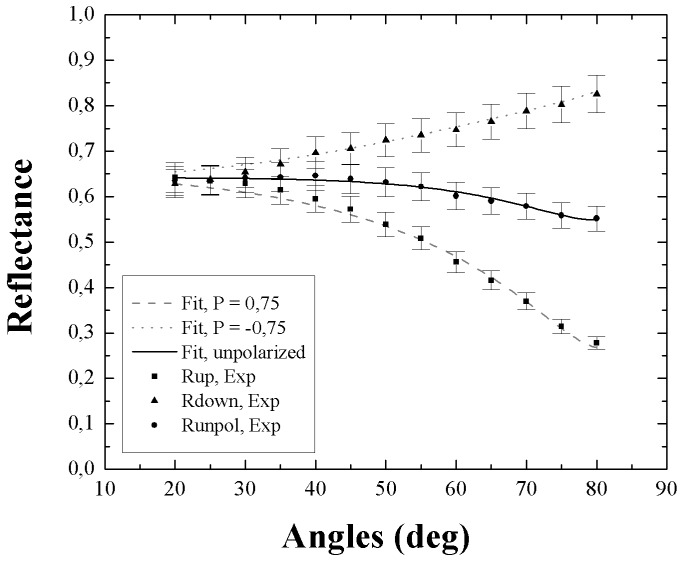

(b)

Figure 3.4. Reflectance of the reference samples versus incidence angle measured during the reflectometer polarization factor characterization. In the graph the curves obtained from the fitting process are also reported: in Figure 3.4(a) for the 70.4 nm line in the EUV range and in Figure 3.4(b) for the 302.2 nm line in the FUV range.

3.2 Subsystem calibration results

The optical subsystems (entrance SiC mirror, EUV grating and FUV grating) of both Qualification Model (QM) and Flight Model (FM) of PHEBUS were characterized with our normal incidence reflectometer facility. The experimental data retrieved from this activities where used to compute the efficiency of the instrument which depends on the first row of the equivalent Mueller matrix of PHEBUS.

Using the relationships 3.5, the TE and TM reflectances can be well-determined from the experimental measurements performed in the reflectometer facility and then also the coefficients m_{11} and m_{12} of the equivalent Mueller matrix are obtained; in fact, if we adopt the simplify model discussed in Section 2.4, the parameters m_{11} and m_{12} are enough to describe the total efficiency of the instrument. However, if also the parameters m_{13} and m_{14} have to be determined we need to know also the phase shift $\phi^{(m)}$ of the entrance mirror. The methods useful to the phase determination are very hard to apply in the entire working range of PHEBUS because no phase shift elements with well efficiency or good polarizers are available: the problem was overcame recovering the phase shift $\phi^{(m)}$ by using a fitting process of the reflectances measured on the sample with the Fresnel's law and obtaining an *hybrid model*. The activities carried out for each optical element can be summarized in these five steps:

1. Experimental measurements of the $R^{(up)}$ and $R^{(down)}$ of the components;

2. Determination of the reflectance for unpolarized light R_{un} averaging the two measurements of $R^{(up)}$ and $R^{(down)}$;

3. Fitting of $R^{(un)}$ with a simulation software (optimization of optical constants and roughness via IMD software [44] in case of SiC mirror and optimization of grooves parameters via PC Grate Software demo version [47] in case of the gratings);

4. Determination of $|r_x|^2$ and $|r_y|^2$ using the measurements of $R^{(up)}$ and $R^{(down)}$ and the polarization factor P experimentally determined during the facility characterization activities; for the entrance mirror, the $|r_x|^2$ and $|r_y|^2$ curves are simulated and compared with experimental results: eventually, some small adjustments of the simulation parameters determined in the previous step can be performed. Finally, the phase shift $\phi^{(m)}$ of the entrance mirror can be determined from the simulations;

5. From the values retrieved in the previous steps, the first row of the equivalent Mueller matrix of PHEBUS is computed.

The experimental uncertainty was estimated evaluating again the measurements repeatability and we found an experimental uncertainty bar of 5% for $R^{(up)}$ and

$R^{(down)}$. Finally, the uncertainties associated to $|r_x|^2$ and $|r_y|^2$ were calculated through the quadratic propagation of the $R^{(up)}$, $R^{(down)}$ and P uncertainties.

3.2.1 The entrance mirrors characterization and results

Both SiC entrance mirrors were characterized using our reflectometer facility as shown in Figure 3.5 using the sources and detectors reported in Table 3.1. For the EUV part of the working range the measurements were performed with a vacuum lower the 10^{-5} mbar.

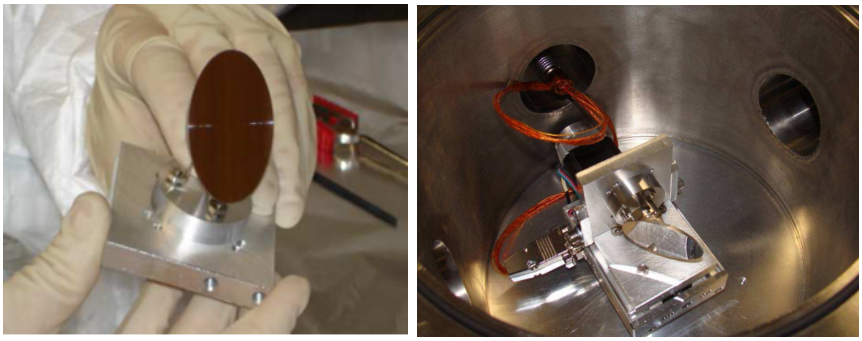

(a) (b)

Figure 3.5. The SiC entrance mirror during the characterization activities using our reflectometer facility. In Figure 3.5(a) is shown the QM mirror and in Figure 3.5(b) is shown the FM mirror fixed inside the reflectometer experimental chamber.

Figure 3.7 shows the results obtained for the QM and FM entrance mirror characterizations together the best fit achieved with the theoretical model. The characterization have been performed over the whole PHEBUS working range, since the mirror is shared by both channels. In the range from 30.4 nm to 121.6 nm the fitting have been computed by using the experimental optical constants provided by D. Windt [46] and finely adjusting the roughness surface ($\sigma = 2.1$ nm) and the roughness of the substrate ($\sigma = 1$ nm). As it can be seen, in both cases a very good match has been obtained by simulations. In the range from 123.3 to 160 nm, experimental optical constants are available in literature only for two wavelengths (132 and 149 nm) and beyond 200 nm (Fernandez-Perea [58], Larruquert [59]), and only in case of a SiC layers deposited by sputtering or Pulsed Laser Deposition (PLD) (Monaco [60, 61]). In the FUV range, therefore, the fitting has involved also the optical constants starting from Fernandez-Perea [58], Larruquert [59] below 200 nm, and Palik [45] for longer wavelengths. The unavailability of well-known optical constants beyond 121.6 nm can justify the mismatch that still persists between simulations and value derived by experimental measurements. In particular, the discrepancy between the

FM and QM mirror in the FUV range can be attributed to the different history of the two components (different deposition conditions, different contamination conditions, different surface oxidation conditions).

3.2.2 The EUV gratings characterization and results

Both QM and FM gratings for the EUV channel were characterized using our reflectometer facility as shown in Figure 3.6. The EUV gratings were characterized only in their nominal working range, for the wavelengths shorter than 160 nm, using the sources and detectors reported in Table 3.1. The measurements were performed with a vacuum condition lower than 10^{-5} mbar.

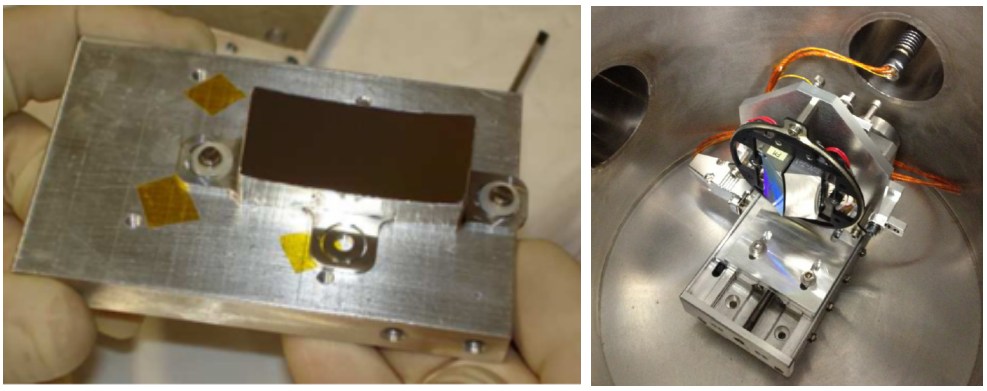

(a) (b)

Figure 3.6. The EUV gratings during the characterization activities using our reflectometer facility. In Figure 3.6(a) is shown the QM grating for the EUV and in Figure 3.5(b) is shown the FM gratings for both PHEBUS channels fixed inside the reflectometer experimental chamber.

In the case of the EUV gratings, the fitting and then the simulations have been computed with PC Grate Software demo version; the input parameters (20 nm depth, 2726 grooves/mm, land to period ratio $c/d = 0.45$) are taken from the grating's specifications provided by the manufacturing company Jobin Yvon. The substrate is Aluminum, the coating is Platinum with a Chromium interlayer interposed; the optical constants used are those provided with the software and are very well known in the EUV spectral range. It is worth to be noticed that the theoretical curve is perfectly compatible with the experimental data for the FM gratings. On the other hand, for the QM gratings bigger discrepancies between the theoretical curves and the experimental data are present; again, this behavior can be attributed to the different history of the two gratings (especially the history concerning to the production conditions and contamination).

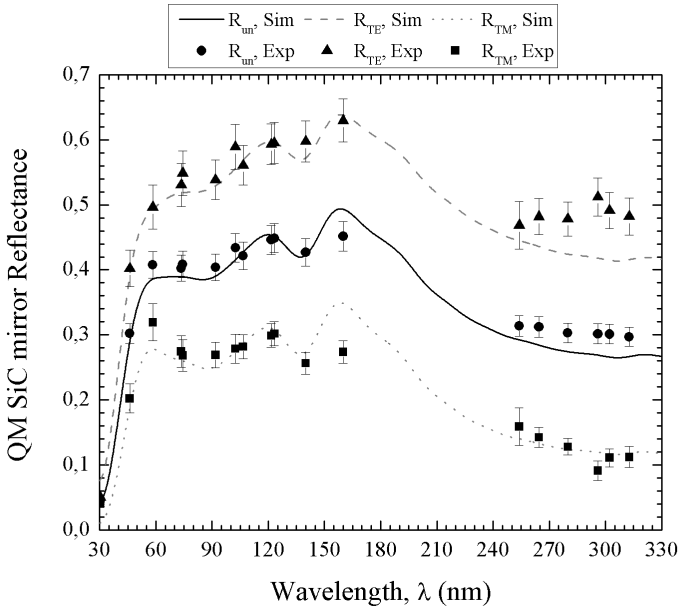

(a)

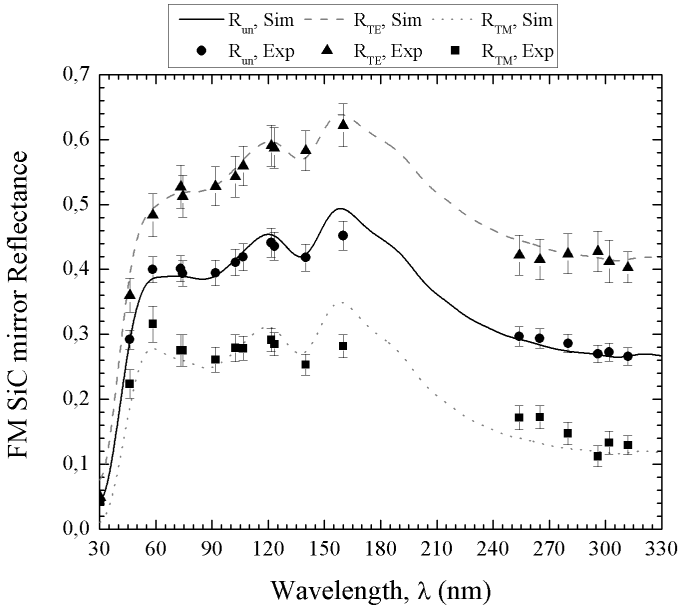

(b)

Figure 3.7. The experimental reflectances of the QM and FM SiC entrance mirror compared with the theoretical curves. In Figure 3.7(a) are shown the QM results while in Figure 3.7(b) are shown the FM results.

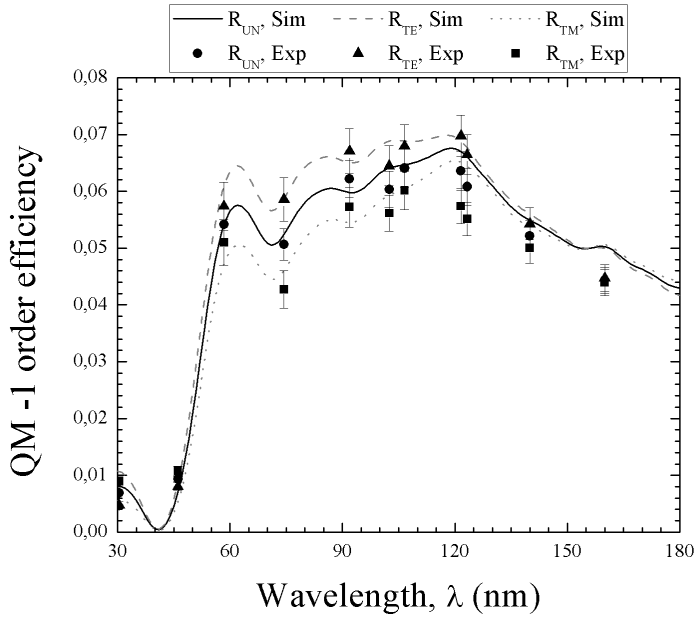

(a)

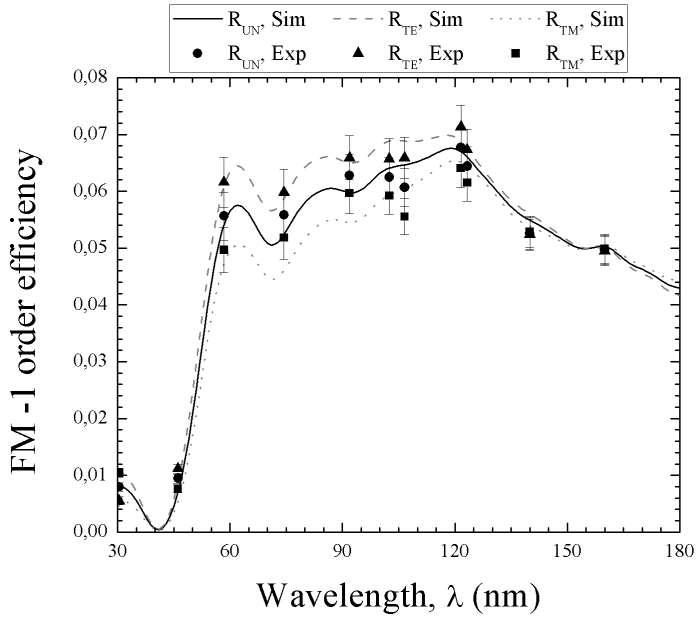

(b)

Figure 3.8. The experimental efficiency of the −1-order of the QM and FM gratings for the EUV channel compared with the theoretical curves obtained with PC Grate demo version. In Figure 3.8(a) are shown the results for the QM component while in Figure 3.8(b) are shown the results for the FM component.

3.2.3 The FUV gratings characterization and results

Analogous procedure has been followed for the FUV gratings which were characterized using the EUV/FUV reflectometer facility. These components were characterized in the FUV range (between about 250 nm up to about 315 nm) using the mercury vapor lamp as source. The results are shown in Figure 3.9. The data collected during experimental activities were compared with the efficiency simulations computed by the PC Grate Software: the input parameters adopted (51.7 nm depth, 1603 grooves/mm and $c/d = 0.56$) were again provided by the manufacturing company Jobin Yvon. However, in this case the experimental efficiencies are slightly higher than the those simulated, especially for the wavelengths longer than about 290 nm. This discrepancy was expected because it is very hard to predict the grating behavior at these wavelengths: the discrepancy can be attributed to differences between the optical constants used in the calculus, which they are very dependent on the deposition process at these wavelengths, and actual ones and mostly in the modeling of the groove profile.

3.2.4 The experimental Mueller matrix parameters

The experimental characterizations of the optical subsystems, performed both for the FM exemplar and QM exemplar, have been used to estimate the experimental first row of the equivalent instrument Mueller matrix. For the parameters m_{13} and m_{14} were adopted an hybrid solution in which the entrance mirror phase shift was theoretically estimated starting from the fitting of the reflectance measurements. However, as were already discussed in the Chapter 2, the values assumed by these two parameters are much lower than the values assumed by the coefficients m_{11} and m_{12} and the instrument efficiency of a generic channel can be approximated as

$$\boldsymbol{\eta_0} = \mathbf{D}\,\mathbf{M}_{PHEBUS} \simeq \eta_d \begin{pmatrix} m_{11} & m_{12} & 0 & 0 \end{pmatrix}$$

where, again, we have assumed a polarization insensitive detector with well-known efficiency η_d.
The experimental coefficients m_{11} and m_{12} were computed for both instrument models starting from the subsystems characterization; the uncertainties associated to the m_{11} and m_{12} values were obtained with the quadratic propagation of the measurement errors.
In Figure 3.10 are shown the results for the QM[6] and computed for a scanning angle

[6]Furthermore, also the parameters m_{13} and m_{14} were evaluated and the values found were compatible or lower than the theoretical previsions. These data are not reported here for shortness reasons and also because no additional information are given.

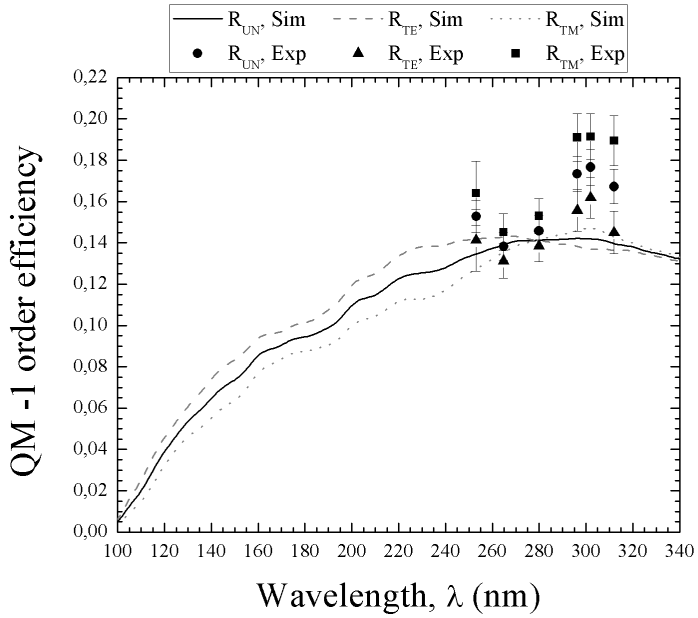

(a)

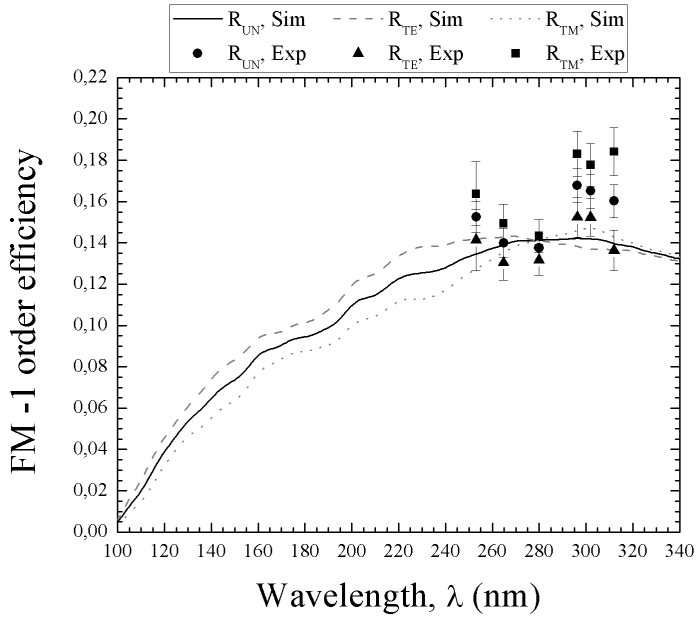

(b)

Figure 3.9. The experimental efficiency of the −1-order of the QM and FM gratings for the FUV channel compared with the theoretical curves obtained with PC Grate demo version. In Figure 3.9(a) are shown the results for the QM component while in Figure 3.9(b) are shown the results for the FM component.

$\theta = 45°$; in the figure the data are also compared with the theoretical curves already presented in Figure 2.11. Similarly, in Figure 3.11 are shown the results for the FM and computed for a scanning angle $\theta = 45°$.
From the Figures, it can be noted that the values obtained for the EUV channel (QM and also FM) are compatible with the theoretical curves and then, the theoretical model well described the polarization behavior of the EUV channel. On the other hand, for the FUV channel the accordance between the experimental values and the theoretical model for wavelengths longer than 290 nm is not as good as the accordance for the EUV channel. As discussed before, the main reasons are the difficulties to know the materials optical constants at these wavelengths together to the difficulties to model the FUV grating, especially for wavelengths longer than 290 nm. Nevertheless, the results obtained are important because suggest us a way to read the information collected by the PHEBUS FUV channel: for the wavelengths shorter than 290 nm the theoretical model describes quite well the real behavior while, for wavelengths longer, the model describes with an higher error the real behavior. As alternative to the theoretical model, a polynomial fit of the experimental data can be also used.

3.3 The backup solutions for the entrance mirror

The entrance mirror is constituted by a super-polished SiC substrate on top of which a SiC coating is deposited. The substrate material was selected for mass constraints in the baffle mechanism while the SiC coating was selected because this material has a good flatness of the reflectance curve in the whole PHEBUS working range. However, the realization of this mirror is a technological challenge due to the fragility of the Silicon carbide and this component has a potential high failure probability. For this reason, in parallel to the subsystems calibration activities, a backup solution for this mirror was studied. The back-up solution selected for the PHEBUS primary parabolic mirror was an Aluminum substrate mirror in which the shape error and roughness were improved using a polished Nickel coating on the top. In order to improve the efficiency in the working range of PHEBUS (from about 50 nm up to 420 nm), an additional coating was deposited above the Nickel layer. Two samples of this substrate solution, one with Platinum and one with Silicon carbide, were realized and characterized in term of reflectance at the BEAR beam line[7] (Elettra Synchrotron, Trieste-Italy)[62] see Figure 3.12.
The procedure followed for reflectance measurements is entirely similar to that adopted in the subsystems characterization. The reflectance was measured in two

[7] For the characterization of the backup samples was chosen the synchrotron radiation because we can measure the reflectance with small steps in wavelength in the whole working range foreseen.

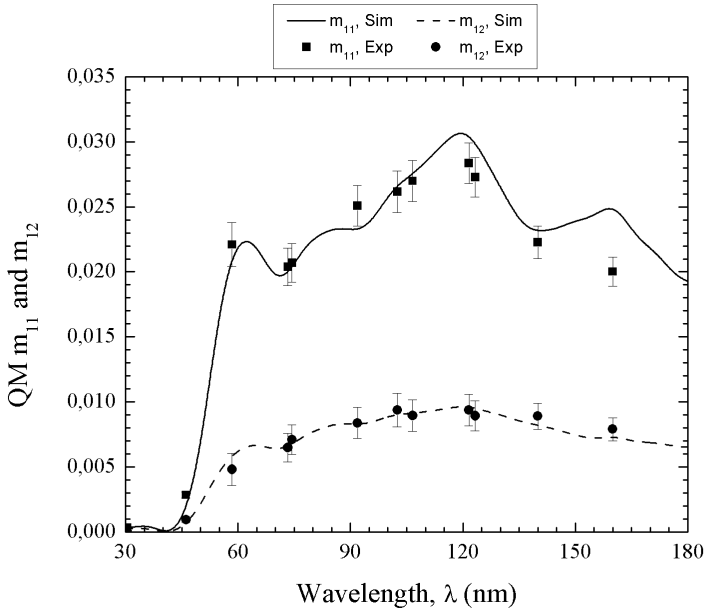

(a)

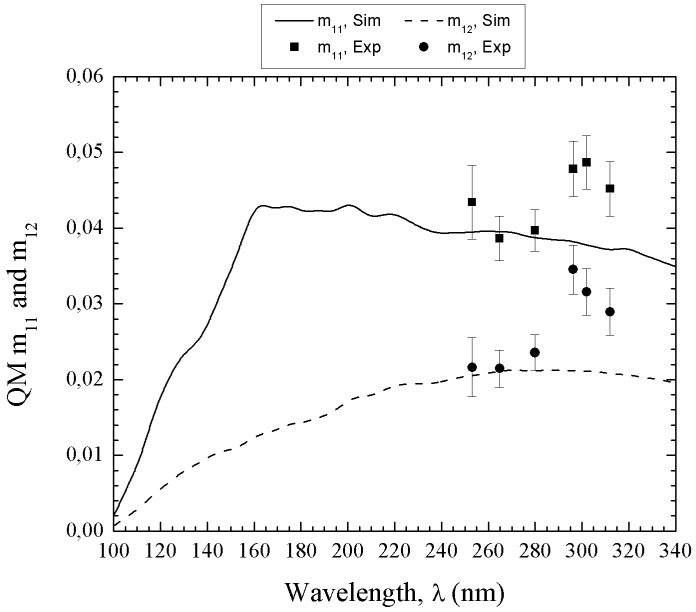

(b)

Figure 3.10. The experimental parameters m_{11} and m_{12} computed for the PHEBUS qualification model with and scanning angle $\theta = 45°$: the Figure 3.10(a) refers to the EUV channel while the 3.10(b) refers to the FUV channel.

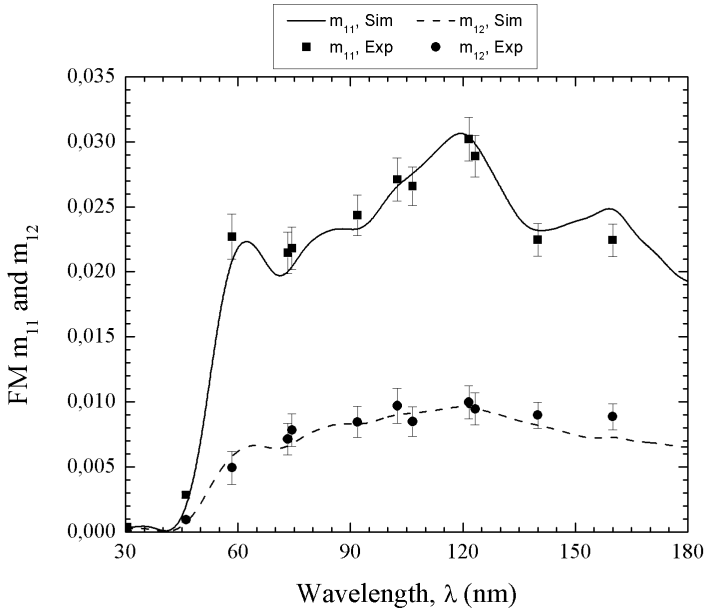

(a)

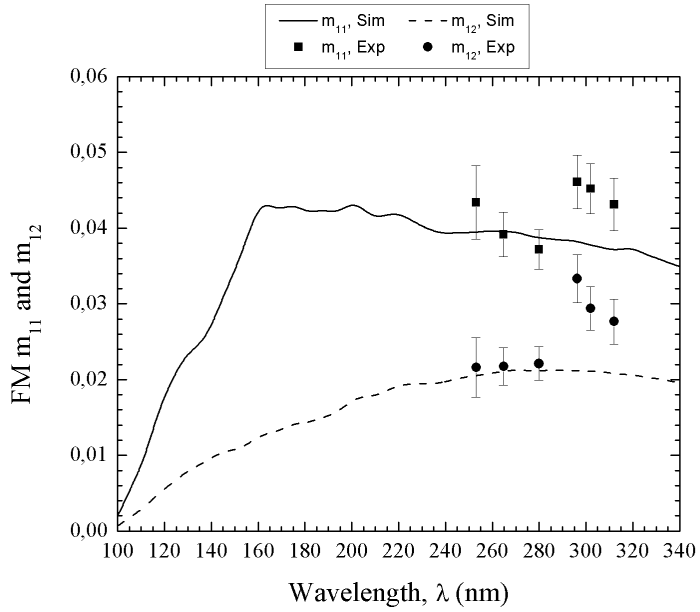

(b)

Figure 3.11. The experimental parameters m_{11} and m_{12} computed for the PHEBUS flight model with and scanning angle $\theta = 45°$: the Figure 3.11(a) refers to the EUV channel while the 3.11(b) refers to the FUV channel.

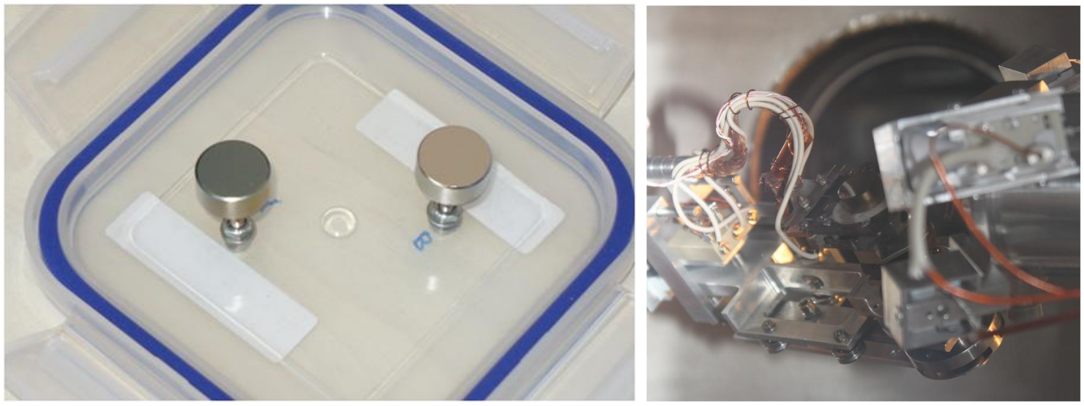

(a) (b)

Figure 3.12. The samples of the backup solution for the SiC entrance mirror: in Figure 3.12(a) the two samples coated by Platinum and Silicon carbide are shown while the Figure 3.12(b) shows the sample with Platinum inside the BEAR beam-line experimental chamber.

different configurations of the experimental chamber, one rotated of 90° to each other, and the TE and TM reflectances where recovered from 2.7 eV to 42 eV (from $\simeq$ 30 nm up to $\simeq$ 450 nm) using the polarization factor of the beamline[8]. In order to avoid higher orders of the monochromator a set of filters were also interposed before the experimental chamber: the experimental condition are reported in Table 3.3. The results obtained are shown in Figure 3.13; the error associated at these measurements is lower than 2%.

From the results, both samples have good reflectance but with some small differences. The Platinum has very high efficiency at longer wavelengths, achieving even 60% in the FUV range, but its efficiency is low in the EUV range. On the contrary, the SiC sample has a quite flat characteristic with higher efficiency in the EUV range and lower efficiency in the FUV if it is compared with the Platinum sample. Considering the fact that the EUV gratings has in general lower efficiency than the FUV gratings, the sample with the SiC optical coating seems a reasonable choice for the back-up solution which increases the EUV efficiency without sacrificing too much the FUV channel.

[8]In the synchrotron facility the radiation is expressed as photon energy instead wavelength. A quick conversion between wavelength and photon energy can be obtained with the relationship

$$\lambda \simeq \frac{1239}{E_{ph}}$$

where λ is expressed in nm and the energy E_{ph} in eV.

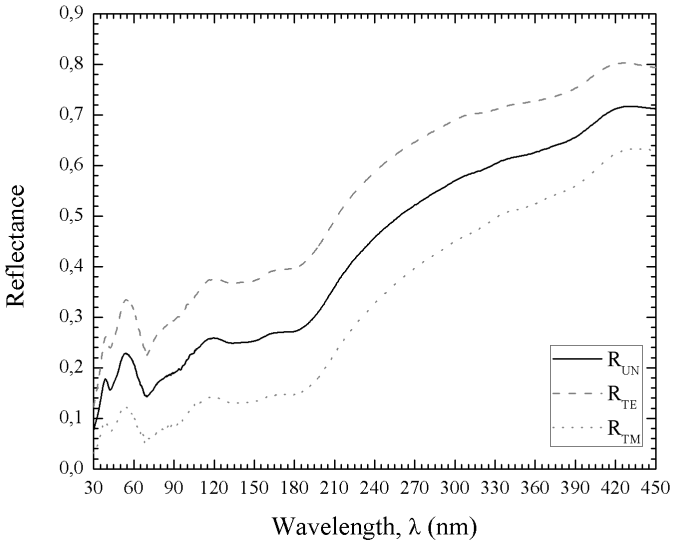

(a)

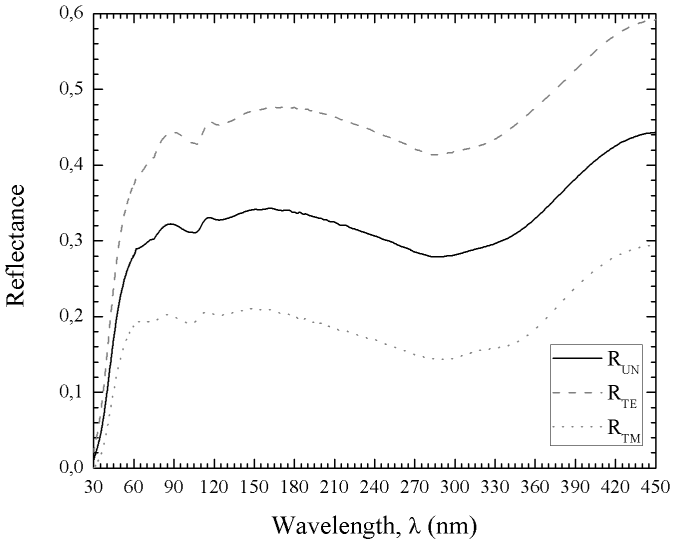

(b)

Figure 3.13. The experimental reflectance of the backup samples obtained using the synchrotron radiation. In Figure 3.13(a) the results for the Pt coated sample are reported while in Figure 3.13(b) the results for the SiC coated sample are reported.

Photon Energy	Filter	Energy step
2.7 eV−4.0 eV	Full beam	0.01 eV
3.9 eV−7.0 eV	SiO2 filter	0.01 eV
6.0 eV−12 eV	LiF window	0.02 eV
11.5 eV−17 eV	In filter	0.05 eV
15 eV−24 eV	Sn filter	0.1 eV
20 eV−42 eV	Full beam	0.1 eV

Table 3.3. The experimental conditions adopted during the synchrotron measurements.

3.4 Additional notes to the chapter

The measurements presented in this chapter were published in the following paper and conference proceedings:

1. A.J. Corso, V. Polito, P. Zuppella, S. Zuccon, M. Nardello, P. Nicolosi, J. L. Maria, J. F. Mariscal, E. Quémerais, M. G. Pelizzo, *Extreme and near ultraviolet experimental facility for calibration of space instrumentation*, Proceeding Paper of SPIE, Vol. 8861, Optics for EUV, X-Ray, and Gamma-Ray Astronomy VI, San Diego (USA), (2013).

2. P. Zuppella, A.J. Corso, V. Polito, J.F. Mariscal, N. Rouanet, J.L. Maria,P. Nicolosi, E. Quémerais and M.G. Pelizzo, *Optical subsystems calibration and derived radiometric instrument response of the PHEBUS spectrometer on board of the BepiColombo Mission*, Journal of Instrumentation 7, P10023 (2012).

3. P. Zuppella, A.J. Corso, P.Nicolosi, M.G. Pelizzo, V. Polito, J.F. Mariscal, N. Rouanet, E. Quémerais, J.L. Maria, *Radiometric calibration of PHEBUS: model and results*, Proceeding Paper of SPIE, Vol. 8443, Space Telescopes and Instrumentation Conference Ultraviolet to Gamma Ray, Amsterdam (Netherland), 84434S (2012).

4. P. Nicolosi, P. Zuppella, A.J. Corso, V. Polito; M.G. Pelizzo, J. F. Mariscal, N. Rouanet, P.O. Mine, E. Quémerais, J.L. Maria, *Optical subsystem characterization in laboratory*, Proceeding Paper of SPIE, Vol.8076, EUV and X-Ray Optics: Synergy between Laboratory and Space II, Prague (Czech Republic), 80760B (2011).

Chapter 4

Instrument level activities: setups and early results on the QM

With the subsystem level calibrations, the first row of the instrument Mueller matrix has been experimentally determined allowing the computation of the pure efficiency of the instrument. More complicated and critical is the experimental measurement of the geometrical factors (e.g. G_r and $A_r^{(\xi=0^\circ)}$), the detector linearity range or the spectral behavior because we have to work at instrument level.
In the first section of this chapter, the optical set-up and the vacuum facility designed and developed for the instrument level calibrations are discussed: the main set-up are the FUV collimator system required for the geometrical factor measurement and the vacuum facility for EUV characterizations. Finally, in the second section, the early results obtained on the QM of PHEBUS are presented and discussed. The optical benches, the vacuum facility and the first QM activities described here have been performed in the CNR-IFN UOS Padova cleanroom. In particular, the space hardware has been always handled in the area at ISO 6.

4.1 Optical benches for the instrument level characterizations

The experimental procedure proposed for the experimental measurement of the real Étendue as well as for the effective collecting area requires a FUV (or a EUV) monochromatic and collimated beam. Furthermore, such collimated beam can be useful in many other instrument level characterizations such as the evaluation of the experimental spectral resolution or the detector linearity range. The main requirements for the collimated beam are its uniformity and its diameter which has to be large enough to fill the entrance pupil of the instrument ($\Phi = 25.4\,\mathrm{mm}$). In the FUV range, the requirements can be quite simply achieved while in the EUV range the

design becomes complicated, especially because no transmissive components can be used[1] and the reflective components have low efficiency: for these reasons, in the PHEBUS ground calibration plan is foreseen the geometric factors measurement only in the FUV range. On the other hand, in the EUV range is possible to realize a quite uniform and nearly collimated source with a small diameter (about $5-15$ mm) that can be useful in pure efficiency measurements at instrument level, in spectral resolution measurements or in experimental determination of the detector linearity range.
In this section the optical benches developed for activities in the FUV (geometric factors, spectral resolution and detector linearity) and EUV (pure efficiency, spectral resolution and detector linearity) range are presented and discussed.

4.1.1 The FUV optical bench

The optical bench for the FUV range has been realized in air because, at these wavelengths, the radiation is able to propagate. As source is adopted a mercury-vapor lamp with an appropriate inferential filters for the lines selection. The source is spatially filtered with a pinhole placed at the focus of an off-axis parabola which is the collimating component of the system: in fact, in this system, the pin-hole approximates a punctual source placed in the focal point of the off-axis parabola. A sketch of the system is shown in Figure 4.1.

Actually, the pin-hole has finite size and then the beam after the parabola has a small residual divergence. This residual divergence can be considered negligible if the pin-hole size is much smaller than the size d_{lim} required to full fill the smaller direction of the PHEBUS field of view. In order to compute the limit size d_{lim} we consider the optical sketch in Figure 4.1. The total magnification of the system (off-axis parabola and PHEBUS entrance mirror) can be computed as

$$M = \frac{f_{in}}{f_A} \simeq 0.54.$$

Let d be the diameter of the pin-hole, if we want the residual divergence smaller than the small side of the field of view the following condition should be verified

$$M \cdot d \ll b$$

where b is the smaller side length of the PHEBUS entrance slit. We find the ideal condition

$$d_{lim} \ll \frac{b}{M} = \frac{283 \cdot 10^{-6}}{0.54} \simeq 524\,\mu\text{m}.$$

[1] Below to about 115 nm there are not materials that transmit with a reasonable efficiency the radiation. The 115 nm wavelength is the absorption edge of the Magnesium Fluoride MgF_2.

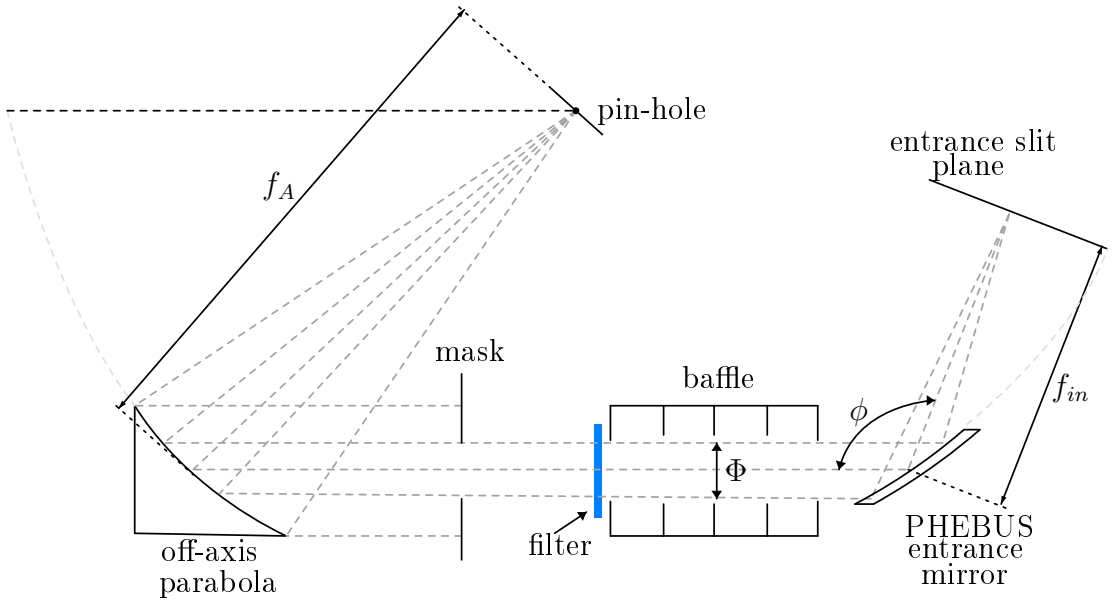

Figure 4.1. Optical sketch of the system adopted as collimator in the FUV: $f_A = 316.5\,\text{mm}$, $f_{in} = 170\,\text{mm}$, $\phi = 100°$ and $\Phi = 25.4\,\text{mm}$. In the sketch is also shown the collecting part of PHEBUS (baffle, entrance mirror and slit plane).

At the same time, the pin-hole has to be large enough to have signal on the detector: in fact, PHEBUS is very sensible to the faint source fluxes but in the field of view mapping method we have also to measure the irradiance of the collimated beam before the instrument baffle. The measurement will be performed collecting the light with a well-known fused silica lens and focusing it on a calibrated Silicon photo diode detector. In order to achieve a reasonable signal to noise ratio in this measurement, the beam should be not too faint. With an experimental approach, measurements with different pin-hole sizes were performed and a compromise was achieved: with a pin-hole of $100 - 200\,\mu\text{m}$ we have a good irradiance of the beam with a reasonable residual divergence for the field of view mapping.

A crucial point of the collimation quality is the alignment of the pin-hole with the focal point of the off-axis parabola: the alignment precision was achieved using the Zygo interferometer. A flat reference mirror were pre-aligned with the off-axis parabola and arranged in the same support (see Figure 4.2(a)). The light outcoming from the interferometer illuminates the parabola and the reference flat mirror; referring to the interferogram produced by the reference flat mirror, the support is adjusted acting on the tip-tilt micrometers until the fringes disappear. In a second moment, a Zygo reference sphere (focal of 37 mm, $f/0.68$) is placed behind the parabola focus. Referring to the interferogram produced by the system parabola

and reference sphere, the distance and the tip-tilt of the reference sphere is varied until a well spherical pattern is achieved. At this point, the pin-hole is placed at the focal point of the parabola: when the pin-hole is well-aligned with the parabola, no variation of the interferogram is observed with respect to the case without pin-hole. When a well-alignment of the pin-hole is achieved, the lamp source can be placed behind the pin-hole. The optimization of the lamp position can be performed collecting the light after the parabola with a fused silica lens and focusing it on a photo-diode: the lamp is moved in the x-y-z direction until the signal of the detector is maximized (see Figure 4.2(a) and Figure 4.2(b)). In front of the photo diode an interferential filter is placed in contact with the case in order to shield the detector from the visible light: we have worked with a filter tuned at 253.1 nm with a band-width of 10 nm. After alignment procedures, a containment box coupled with an ozone-eater was used for the lamp in order to avoid straight-light and ozone in the room.

The uniformity of the output beam was investigated with a Silicon photo-diode by sampling the output collimated beam in a transverse section of about 36.5 × 39 mm. From the sampling results, the more uniform region of the beam was selected by a calibrated mask with a diameter of 25.4 mm and mounted in a micro-metric support. The collimated beam obtained after the alignment procedure and the position of the calibrated mask are shown in Figure 4.3. Finally, the desired mercury-vapor lamp emission line was selected with and interferential filter. The filters were placed very close to the baffle entrance in order to shield as much as possible the ambit visible light (computer monitor, indicator lights, etc...) because the PHEBUS FUV detector is slightly sensitive to visible photons. The FUV lines selected by the filters were 253.1 nm, 279.9 nm, 296.3 nm, 302.2 nm and 312.7 nm.
The Field of View mapping method requires to change the source angle with respect to the instrument entrance pupil. However, the collimating system alignment is sensitive to the movements. As alternative, a precision stage for the instrument has been designed and developed: this stage is named *Taga-dá* and it can move the instrument with a step resolution of 0.01° allowing the alignment of the instrument with the collimating system and a fine scanning of its field of view.

4.1.2 The EUV optical bench

The pure efficiency of PHEBUS will be tested at instrument level also for the EUV channel in order to validate the results obtained by the optical subsystems calibration. Furthermore, also the spectral behavior should be tested. For these purposes, a small monochromatic collimated beam is introduced at the center of the field of view and the entrance pupil of the instrument for a defined position of the baffle: in fact, the instrument is illuminated in the *chief-ray condition*. Due to the small beam dimensions required a monochromator system has been developed in order to achieve

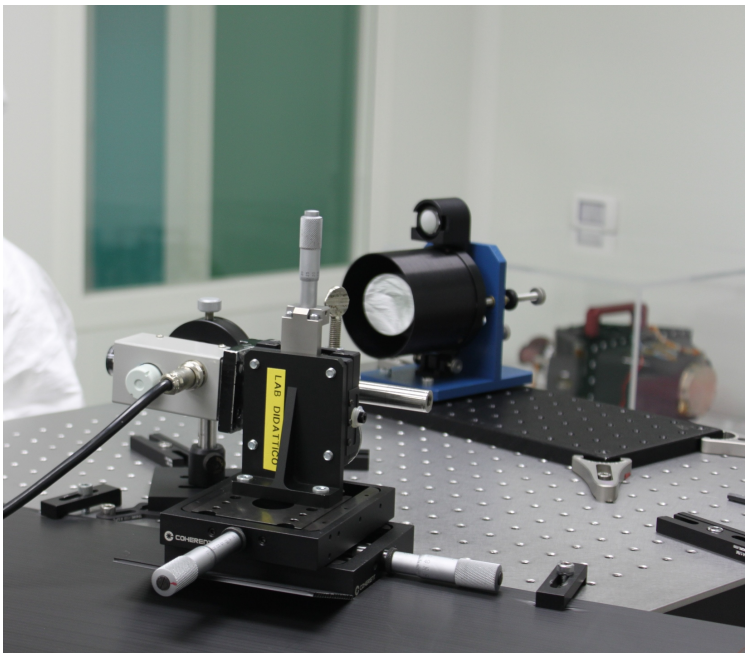

(a)

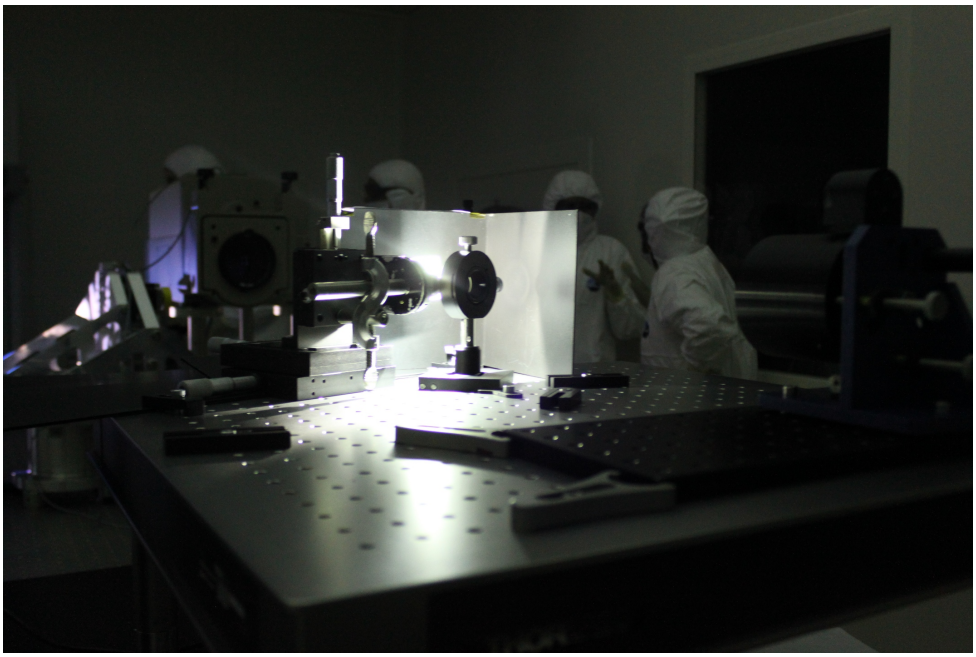

(b)

Figure 4.2. Images of the FUV collimator system used during QM calibration. In Figure 4.2(a) is shown the off-axis parabola with above its reference flat mirror while in Figure 4.2(b) is shown the source lamp (turned on) and the pinhole after alignment.

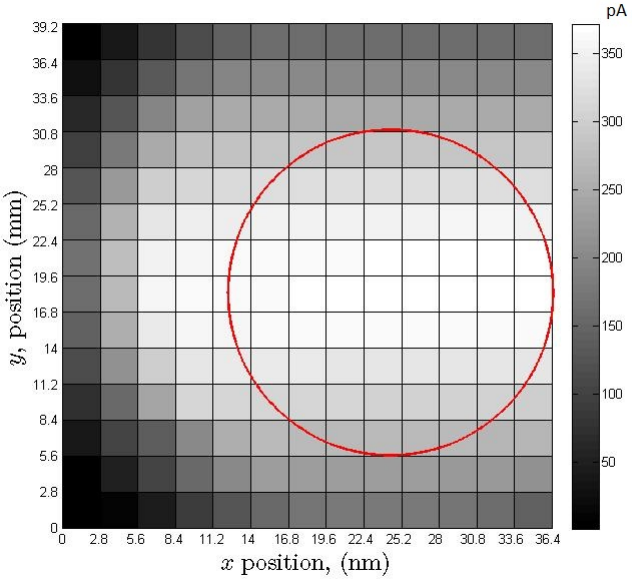

Figure 4.3. The uniformity of the collimated beam obtained by the transverse sampling with a Silicon photo-diode. The red circle indicates the more uniform area selected by the mask with a diameter of 25.4 mm.

high spectra purity useful for the calibration activities foreseen. The measurements need an high vacuum level (lower than 10^{-5} mbar) and then also PHEBUS is put in vacuum inserting it in a big vacuum chamber. This chamber, named also *tank*, has a dimension of about 3 m^3 and it can reach up to about 10^{-7} mbar pressure (see Figure 4.4(a)). It is equipped with electrical and mechanical feed through for flight models testing. The door is interfaced with the Area at IOS 6 of the cleanroom (for example, PHEBUS will enter inside this front door), but it is fully operate from Area at ISO 7, where vacuum systems and controllers are placed. In the case of an electrical blackout or any malfunctioning safety interlocks shut down the tank vacuum system by closing the gate valves between the vacuum chamber and the pumping system (two big turbo pumps). A two axis rotation stage can be placed inside the tank or removed out by a rail; the stage is remotely controlled. The instrument under test can be placed on top of this stage and aligned with respect to the entering beam by a fine rotation with 0.01° of resolution.
The vacuum chamber is coupled with a McPherson monochromator, Model 234/302, which is based on a *Seya - Namioka* configuration [63]. The spectrometer is composed by three different parts: the *source section*, the *monochromator section* and the *collimating section*. The source section of the spectrometer is composed by the lamp and the reflective condenser (McPherson Model 615 Condenser) which collects

(a)

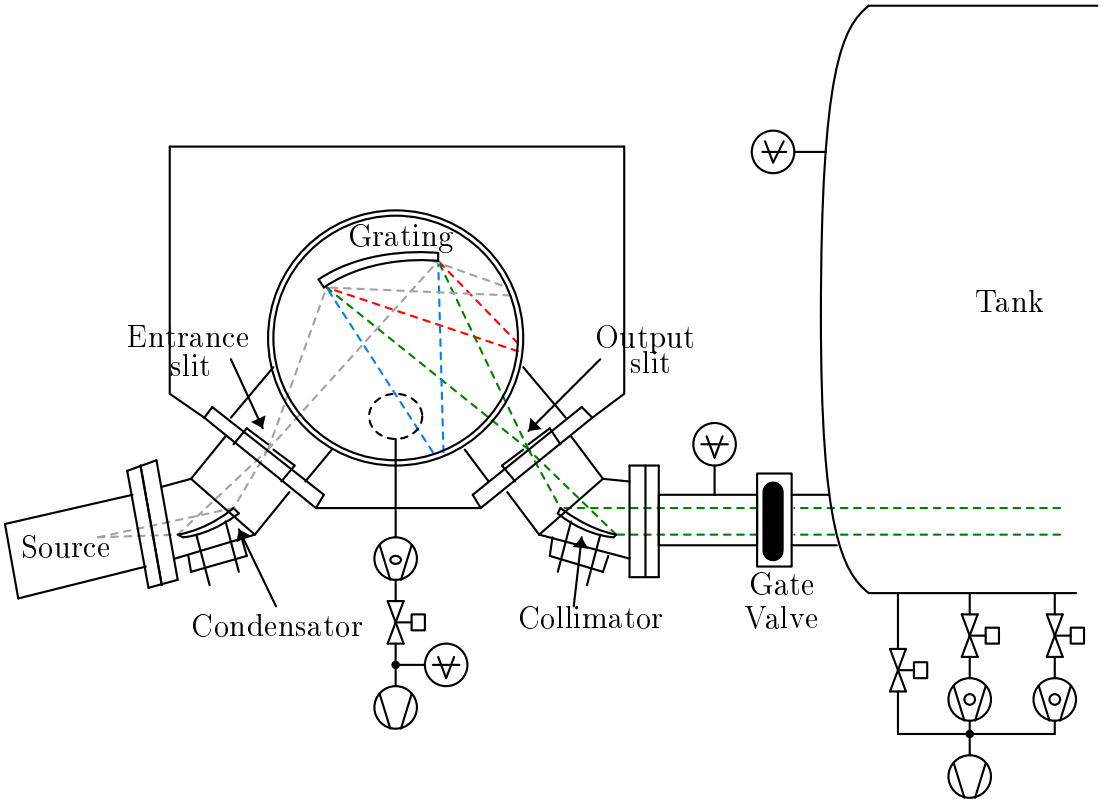

(b)

Figure 4.4. EUV optical bench developed for the PHEBUS instrument level activities. In Figure 4.4(a) is shown an image of the system placed in the CNR-IFN U.O.S. Padova cleanroom: the big chamber, named *tank*, is coupled with the monochromator system and it will host PHEBUS during the measurements in vacuum. In Figure 4.4(b) is reported an optical-mechanical sketch of the monochromator system.

the light coming from the source and focused it onto the entrance slit. The spectrometer is composed by a 2400 grooves/mm (for shorter wavelengths up to 100 nm) and a 1200 grooves/mm (for longer wavelengths) IV type aberration corrected concave gratings. The gratings can be selected by a rotating turret mechanism. The selected grating collects the radiation coming from the entrance slit and focuses it onto the exit slit. Finally, an off axis parabolic mirror with a grazing incidence angle of about 20° collimates the beam. An optical layout of the full monochromator system is reported in Figure 4.4(b). The optical system was optimized in order to obtain a beam divergence of about 0.8° (both spectral and spatial direction) and a spot size of about 16 mm × 16 mm (spectral) × (spatial) at 2 m of distance from the exit slit when this last one is settled at 0.25 mm × 2 mm. The 0.25 mm width setting corresponds to about 1 nm of bandpass.

4.2 The early activities on the PHEBUS QM

At this moment (end of 2013), only the QM model of PHEBUS has been integrated but without the EUV detector. This model has been used also as training for the calibration activities that will be performed on the FM. A lot of technical unexpected problems were solved during the QM activities collecting a good background experience. The FM model will be integrated in 2014 and all channels will be calibrated performing the geometrical factors measurement as well as the detectors range of linearity.
This section shows the early results obtained with the QM during the calibration campaign performed at the CNR - IFN UOS Padova laboratory. The channel was calibrated in air using the FUV collimating system described before. In particular the spectral assignment and the detector linearity range determination were performed.

4.2.1 Operations start-up

PHEBUS were accommodated on the taga-dá stage and aligned with the collimation system (as shown in Figure 4.5(a)). The system and the cleanroom ambient were arranged in order to reduce as much as possible the background visible light: in fact, we found a slight sensitivity of the FUV detector of visible photons. The background images were taken for each measurement condition performed during the activities but with the source stopped by a shutter; then, the images obtained were removed from the data during the analysis (see Figure 4.5(b) as example). The level of dark counts is quite low with less than 100 counts per second for 512 × 256 pixels, less than 10^{-3} counts per pixel per second.

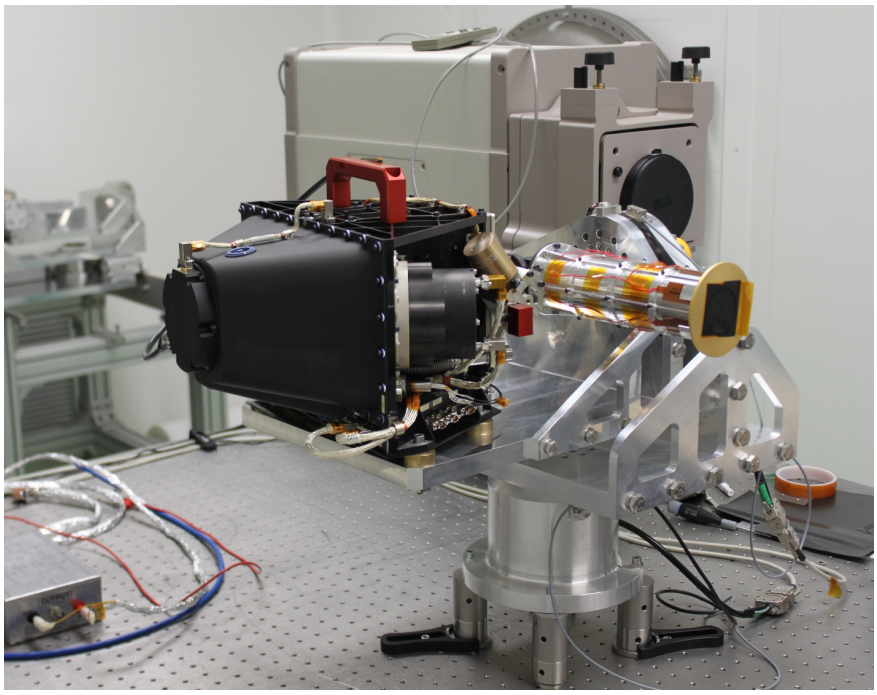

(a)

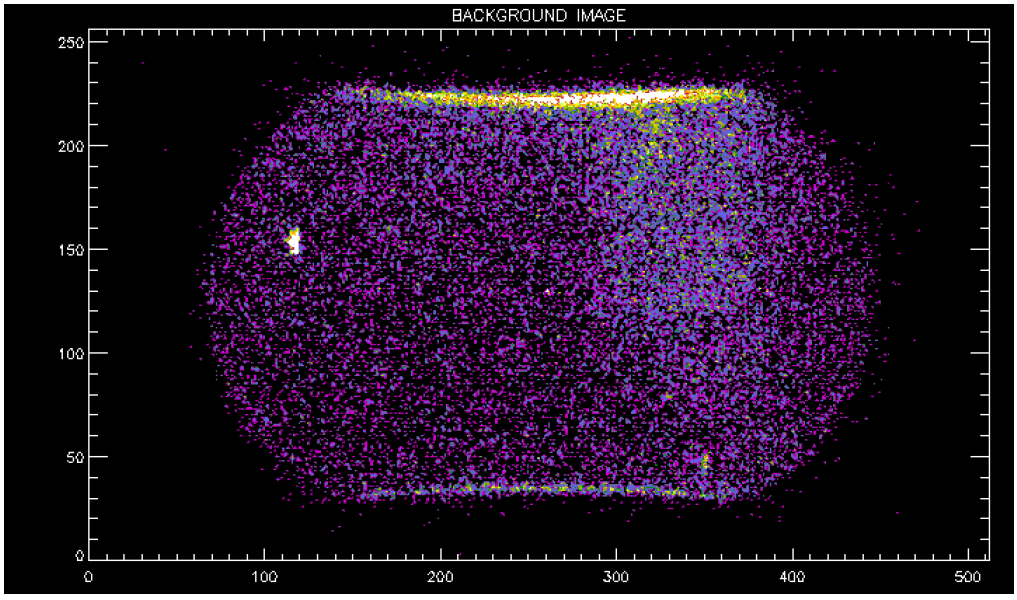

(b)

Figure 4.5. (a) PHEBUS accommodated on the taga-dá stage in our clean-room. (b) shows an example of dark images obtained by a cumulation of images when the source was not active. This constitutes a background image that is removed from the measurements.

4.2.2 FUV detector range of linearity

For the measurements of the detector range of linearity, a line of the Hg Lamp source has been selected with 3 spectral filters: we isolated the 279.9 nm line (see Figure 4.6(a)). The source beam has been kept the same during the whole observation session and the total intensity has been regularly monitored in order to evaluate variations: the source lamp was found very stable during the session. The use of 3 spectral filters on the optical path eliminates all spectral contributions except a narrow band around 279.9 nm (the FWHM band bass of the filters was about 10 nm). In addition various neutral optical densities with well calibrated transmission functions have been placed and removed on the light path in order to change the illuminating flux at will. The spectral shape has been monitored and it was not changed by the neutral densities. During measurements the total counts on the MCP array has been also monitored.
Ten images with an integration time of 8 seconds and the MCP nominal high voltage (4500 V) have been taken and then average spectrums with an equivalent cumulative time of 80 seconds have been computed. Each image has been taken in *binning mode*, with a resolution of 512 pixels and not 1024 pixels. An image of the average spectrum obtained at 279.9 nm[2] is shown in Figure 4.6(b). The image shows the main line (at 279.9 nm) with a width of about 8 pixels (about 3.4 nm) and a smaller line at shorter wavelength (at about 275 nm) on the right side in the plot. The wavelength interval between the two lines is 4 nm and the second line is 3% of the peak value of the first line. Both lines are well defined in each measurement even if the faintest line is hidden in the noise background when the source intensity is very attenuated.
From the measurements collected it is possible to plot the count rate of the detector as a function of the relative flux intensity. The highest source flux S_{MAX} is defined as 1. Figure 4.7(a) shows the total count rate per second as a function of the relative beam flux. A perfectly linear detector should give a straight line instead the plot shows that the detector is not linear after approximately $2000 - 3000$ counts per second on the total array.
A second important parameter is the line width evaluated as function of the total count rate reported in Figure 4.7(b). The width should be independent on the count rate but we see that the width increases for count rates (total counts on array per second) when the detector works in its non-linear characteristic (above 2000 counts per second). In the figure is also shown the average line width (dashed grey line) computed with the data collected when the detector works in linearity.

From the measurements it appears that the detector is not linear for total count

[2] As we will see in the following, this spectrum has been collected with the conditions required by linearity of the detector.

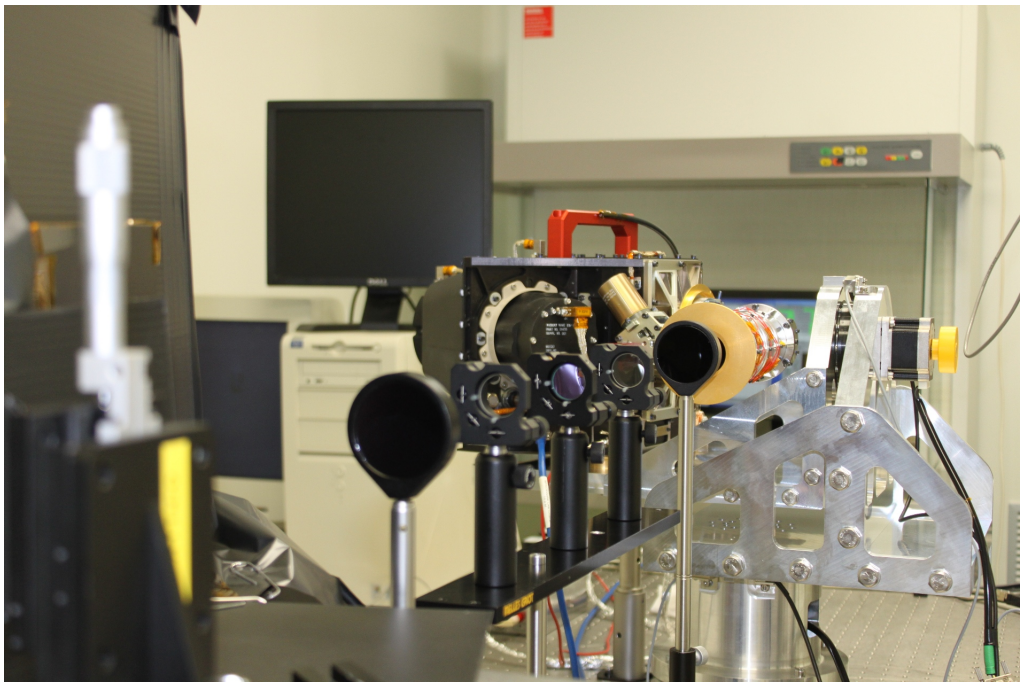

(a)

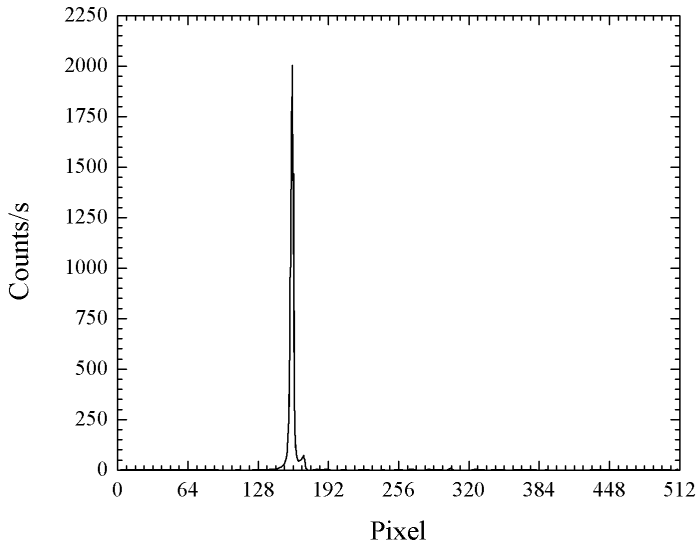

(b)

Figure 4.6. Figure 4.6(a) the optical set-up adopted for the detector linearity range measurements. In Figure 4.6(b) the appearance of the average spectrum taken by PHEBUS at 279.9 nm after filtration. The total cumulative time is 80 seconds.

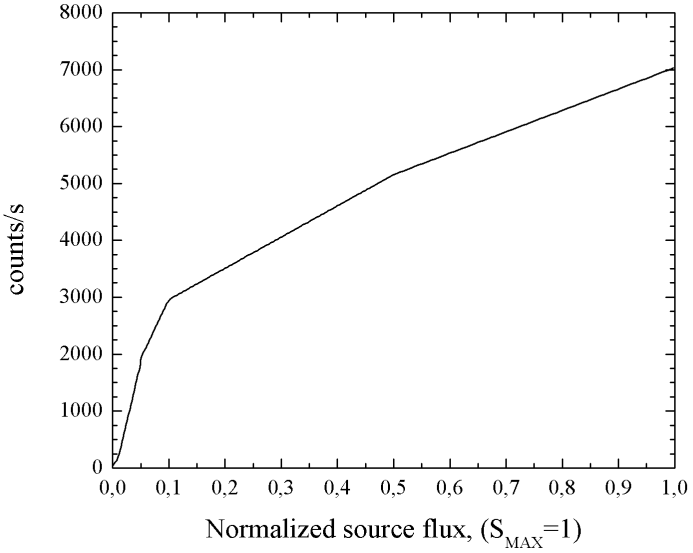

(a)

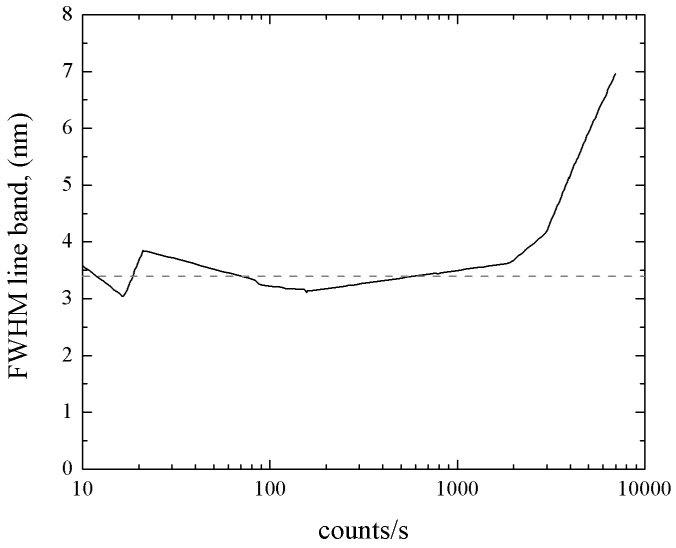

(b)

Figure 4.7. In Figure 4.7(a) is shown the total count rate versus the relative source flux: the highest source flux S_{MAX} is defined as 1. In Figure 4.7(b) is shown the width of the line (FWHM) as a function of total counts on the array.

rates on the array higher than 2000 counts per second. In fact, this behavior is caused by the response of the MCP to an irradiance value that is too high. When beams are too intense, the intensifier loses linearity creating a local saturation on the number of counts per pixel. This creates a loss of linearity between the count rate and the intensity of the beam and also creates a deformation of the line shape because the center of the line is saturated but not the wings.

4.2.3 Experimental spectral assignment

Wavelength assignment (relation between pixel number and wavelength of the line) on the detector has been obtained by observing a well-known source with multiple lines. In-flight this is done by observing a well-calibrated star even if this method is less precise because stellar lines tend to be much larger than calibration lamp lines. On the other hand, exospheric lines are very narrow and it will be easy to track changes of the wavelength assignment during flybys and in orbit around Mercury.
The source adopted in these measurements is still a vapor mercury lamp placed in the collimating system already described but without filtering. The total flux of the beam has been attenuated with a set of neutral optical densities in order to achieve a liner working point of the detector (see Figure 4.8(a)). At the same time, the spectrum of the collimating beam has been also observed with a well calibrated reference spectrometer: in our measurements we have used the Ocean optics USB4000 spectrometer [64]. Wavelengths assignment has been performed by determining the characteristics of each line in both measurements and comparing the wavelength value given by the reference spectrometer with the pixel number given by the PHEBUS detector. The couples (pixel-wavelength) where analyzed. As expected the relationship is not strictly linear but it can be fit by a third-order polynomial law even if the non-linearity is not very large, with a small stretch of about 1 nm onto 100 nm. In Figure 4.8(b) is shown the mercury-vapor lamp spectrum taken by PHEBUS after the conversion pixel-wavelength.
The spectral resolution measurements require narrow lines in order to precisely determine their width at half of the maximum value. However, in this range the lines of the calibration lamp are not thin enough to make such measurement. On the other hand, with a cross-comparison of measurements performed with the two spectrometers (PHEBUS and the reference spectrometer) we can conclude that the spectral resolution of the two spectrometers are comparable and in the $1 - 2$ nm range.

(a)

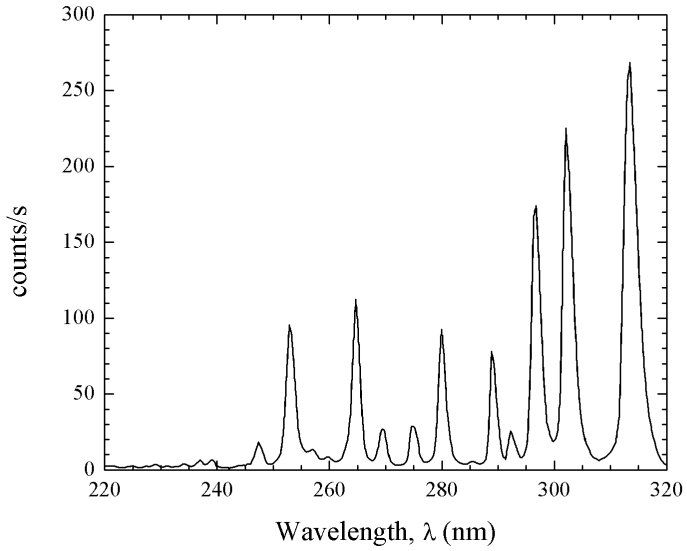

(b)

Figure 4.8. In Figure 4.8(a) is shown a picture of the optical setup used for the wavelengths assignment with the collimating system and the neutral optical densities for the beam attenuation. In Figure 4.8(b) is shown the spectrum of the mercury-vapor lamp taken by PHEBUS after the wavelengths assignment.

Chapter 5

Conclusions

Probing of Hermean Exosphere By UV Spectroscopy (PHEBUS) is a dual channel spectroscope working in the EUV (from 55 nm to 155 nm) and FUV (from 145 nm to 315 nm) that will be launched on July 2016 on board of ESA BepiColombo mission. This instrument is developed by an international cooperation of four countries: France that has the leadership of the instrument and the responsibility of its integration, Russia that has the responsibility of the movement mechanisms, Japan that has the responsibility of the detectors and Italy that has the responsibility of the instrument calibration. PHEBUS will be devoted to study the composition, dynamic and formation mechanisms of the Mercury exosphere by using a spectroscopic approach. A more detailed description of the optical configuration of PHEBUS together its scientific objectives is given in Chapter 1.
The data collected during the mission will be interpreted by using a model which well-describes the instrument spectral and radiometric behaviour. Furthermore, this model has also to be validated and, eventually, adjusted by experimental characterization activities[1] in order to match as much as possible the real instrument behavior. In this work, the radiometric characteristics of an optical instrument have been widely studied. In Chapter 2 an original and innovative approach for the radiometric modelling of a generic instrument has been proposed, considering also the effects introduced by the polarized light. In particular, we have found that the radiometric response of an instrument working in its linear range can be divided into two main components: the *efficiency term* which takes into account the efficiency of each optical element also considering the polarization state of the light (by using the Stokes-Mueller formalism) and the *geometrical part* which takes into account the geometry of the instrument (field of view, entrance pupil, etc...). The formalization of this radiometric model has also suggested us an operative procedure to

[1]Sometimes said also *ground calibration activities*.

its experimental determination and validation: the efficiency term can be retrieved by subsystem level characterizations while the geometrical part can be measured by an instrument level approach. Moreover, at the instrument level, other functional characteristics can be tested: typical measurements are the point spread function for an imaging instrument or the spectral assignment and resolution for a spectroscopic instrument.
The radiometric approach proposed has been also applied to PHEBUS. An experimental calibration plan devoted to model validation has been defined. The subsystems characterizations have been performed both for the QM and FM optics and the efficiency term has been retrieved: the results obtained have been presented and discussed in Chapter 3. In addition, the optical benches and vacuum facilities required for the instrument level calibrations of PHEBUS, both in the EUV and FUV range, have been designed and developed: a collimator optical system have been realized for the Étendue and spectral measurements in the FUV range while a vacuum facility have developed for efficiency and spectral measurements in the EUV range. Together the optical benches, in Chapter 4 are also reported the early instrument level characterizations concerning to the detector linearity range determination and the spectral assignment performed on the QM. The same optical benches and the vacuum facility will be used for the detailed calibration at instrument level of the FM (Field of View mapping, spectral behaviour, detector linearity range etc...). The experimental activities carried out on the QM have taught us much concerning to PHEBUS and its operation and the vested background obtained will be crucial to successfully complete the radiometric characterization of the FM. The model that will be built for the PHEBUS FM will be pivotal in the data processing during the scientific observations.
Finally, it is important to highlight that the radiometric modelling followed in this work have been obtained with a general treatment and then it can be applied at any instrument, especially when the polarized light effects have to be considered.

Appendix A

The Mueller matrix of PHEBUS

The Mueller matrix of a PHEBUS channel is derived by the left-multiplication of each optical element Mueller matrix encountered in the light path. For both channels, optical components involved in the light path are: the entrance mirror, the EUV or FUV grating and the EUV or FUV detector. Due to the rotation ability of the mirror against the rest of the instrument, we have to take into account the rotation angle θ. We have

$$\mathbf{M}_{PHEBUS} = \mathbf{M}_{grating}\mathbf{M}_{scan}(\theta)\mathbf{M}_{mirror} \tag{A.1}$$

By replacing the matrices for each optical elements in A.1 and after some long algebraic manipulations the equivalent PHEBUS Mueller matrix is described by the relationship A.2 in which the mark "m" refers to the mirror, the mark "g" refers to the gratings and for reading reasons we have made the the following substitutions

$$\begin{aligned} A_i &= \frac{|r_x^i|^2 + |r_y^i|^2}{2}, \quad B_i = \frac{|r_x^i|^2 - |r_y^i|^2}{2}, \quad i = m, g \\ C_i &= \mathrm{Re}\left[r_x^i \left(r_y^i\right)^*\right], \quad D_i = \mathrm{Im}\left[r_x^i \left(r_y^i\right)^*\right], \quad i = m, g \end{aligned}$$

$$
\mathbf{M}_{PHEBUS} = \\
= \begin{pmatrix}
A_m A_g + B_m B_g \cos(2\theta) & A_g B_m + A_m B_g \cos(2\theta) & B_g C_m \sin(2\theta) & -B_g D_m \sin(2\theta) \\
A_m B_g + A_g B_m \cos(2\theta) & B_m B_g + A_m A_g \cos(2\theta) & A_g C_m \sin(2\theta) & -A_g D_m \sin(2\theta) \\
-B_m C_g \sin(2\theta) & -A_m C_g \sin(2\theta) & -D_m D_g + C_m C_g \cos(2\theta) & -C_m D_g - C_g D_m \cos(2\theta) \\
-B_m D_g \sin(2\theta) & -A_m D_g \sin(2\theta) & C_g D_m + C_m D_g \cos(2\theta) & C_m C_g - D_m D_g \cos(2\theta)
\end{pmatrix} \quad \text{(A.2)}
$$

Appendix B

Results of the subsystems characterizations

In this appendix, the experimental results obtained from the subsystems characterization activities are reported. For each kind of optical element, both the QM and FM results are reported.

	FM Entrance Mirror				QM Entrance Mirror			
Wavelength	R_{TE}	$\Delta R_{TE}(\%)$	R_{TM}	$\Delta R_{TM}(\%)$	R_{TE}	$\Delta R_{TE}(\%)$	R_{TM}	$\Delta R_{TM}(\%)$
30,4	0,048	9,04	0,042	10,08	0,050	8,85	0,040	10,41
46,1	0,360	7,28	0,224	9,88	0,402	7,04	0,202	11,05
58,4	0,484	6,88	0,316	8,80	0,497	6,86	0,319	8,86
73,3	0,527	6,29	0,275	8,85	0,531	6,28	0,275	8,89
74,4	0,513	6,30	0,275	8,72	0,549	6,25	0,268	9,16
91,9	0,528	5,69	0,261	7,42	0,538	5,69	0,269	7,38
102,5	0,543	5,77	0,279	7,53	0,589	5,85	0,279	8,12
106,6	0,560	5,45	0,278	6,64	0,561	5,45	0,282	6,61
121,6	0,591	5,30	0,291	6,14	0,593	5,30	0,299	6,09
123,3	0,587	5,30	0,285	6,18	0,595	5,30	0,302	6,07
140	0,583	5,31	0,253	6,46	0,598	5,31	0,256	6,51
160	0,622	5,28	0,282	6,27	0,630	5,29	0,273	6,40
253,1	0,422	7,23	0,172	10,78	0,468	7,73	0,159	18,07
264,8	0,415	7,54	0,172	10,38	0,482	5,78	0,142	10,99
279,9	0,424	7,34	0,147	11,96	0,478	5,50	0,128	9,93
296,3	0,428	7,24	0,112	14,60	0,512	5,72	0,091	16,34
302,2	0,412	7,98	0,133	13,26	0,491	5,62	0,111	12,41
312,7	0,403	5,94	0,129	11,18	0,482	5,90	0,112	14,36

Table B.1. The experimental reflectance of the FM and QM entrance mirrors obtained during optical subsystems characterizations.

	FM EUV grating				QM EUV grating			
Wavelength	R_{TE}	$\Delta R_{TE}(\%)$	R_{TM}	$\Delta R_{TM}(\%)$	R_{TE}	$\Delta R_{TE}(\%)$	R_{TM}	$\Delta R_{TM}(\%)$
30,4	0,006	12,86	0,010	8,00	0,005	12,84	0,009	8,01
46,1	0,011	7,42	0,008	9,43	0,008	9,10	0,011	7,55
58,4	0,062	7,16	0,050	8,10	0,057	7,32	0,051	7,83
73,3	0,060	6,74	0,052	7,24	0,059	6,54	0,043	7,65
74,4	0,060	6,74	0,052	7,24	0,059	6,54	0,043	7,65
91,9	0,066	5,92	0,060	6,10	0,067	5,87	0,057	6,17
102,5	0,066	5,43	0,059	5,54	0,065	5,44	0,056	5,58
106,6	0,066	5,51	0,056	5,69	0,068	5,52	0,060	5,65
121,6	0,071	5,27	0,064	5,32	0,070	5,26	0,057	5,37
123,3	0,067	5,27	0,061	5,32	0,066	5,25	0,055	5,37
140	0,052	5,25	0,053	5,24	0,054	5,23	0,050	5,28
160	0,050	5,23	0,050	5,22	0,045	5,21	0,044	5,23

Table B.2. The experimental -1 order efficiency of the FM and QM EUV gratings obtained during optical subsystems characterizations.

	FM FUV grating				QM FUV grating			
Wavelength	R_{TE}	$\Delta R_{TE}(\%)$	R_{TM}	$\Delta R_{TM}(\%)$	R_{TE}	$\Delta R_{TE}(\%)$	R_{TM}	$\Delta R_{TM}(\%)$
253,1	0,141	10,55	0,164	9,45	0,141	10,56	0,164	9,41
264,8	0,130	6,47	0,149	6,15	0,131	6,42	0,145	6,18
279,9	0,132	5,63	0,143	5,54	0,139	5,64	0,153	5,23
296,3	0,152	6,40	0,183	6,00	0,156	6,43	0,191	5,79
302,2	0,152	6,05	0,178	5,79	0,162	6,06	0,191	5,68
312,7	0,136	7,19	0,184	6,30	0,145	7,12	0,189	6,33

Table B.3. The experimental -1 order efficiency of the FM and QM FUV gratings obtained during optical subsystems characterizations.

Appendix C

Publications produced during my PhD

ISI journals:

1. M. Nardello, P. Zuppella, V. Polito, A.J. Corso, S. Zuccon, M.G. Pelizzo, *Stability of EUV multilayer coatings to low energy alpha particles bombardment*, Optics Express 21(23), 28334-28343 (2013).

2. A.J. Corso, P. Zuppella, F. Barkusky, K. Mann, M. Muller, P. Nicolosi, M. Nardello and M.G. Pelizzo, *Damage of multilayer optics with varying capping layers induced by focused extreme ultraviolet beam*, Journal of Applied Physics 113(20), 203106 (2013).

3. P. Zuppella, S. Tosatto, A.J. Corso, S. Zuccon and M.G. Pelizzo, *Graphene-noble metal bilayers for inverted surface plasmon resonance biosensors*, Journal of Optics 15, 055010 (2013).

4. M.G. Pelizzo, A.J. Corso, P. Zuppella, P. Nicolosi, *Multilayer coatings and their use in spectroscopic applications*, Nuclear Instruments and Methods in Physics Research Section A, 720, 49-52 (2013).

5. A.J. Corso, P. Zuppella, D.L. Windt, M. Zangrando, M.G. Pelizzo, *Extreme ultraviolet multilayer for the FERMI@Elettra free electron laser beam transport system*, Optics Express 20(7), 8006-8014 (2012).

6. P. Zuppella, A.J. Corso, V. Polito, J.F. Mariscal, N. Rouanet, J.L. Maria,P. Nicolosi, E. Quemérais and M.G. Pelizzo, *Optical subsystems calibration and derived radiometric instrument response of the PHEBUS spectrometer on board of the BepiColombo Mission*, Journal of Instrumentation 7, P10023 (2012).

7. M.G. Pelizzo, S. Fineschi, A.J. Corso, P. Zuppella, P. Nicolosi, J. Seely, B. Kjornrattanawanich, D.L. Windt, *Long-term stability of Mg/SiC multilayers*, Optical Engineering 51(2), 023801 (2012).

8. A.J. Corso, P. Zuppella, P. Nicolosi, D.L. Windt, E.M. Gullikson, M.G. Pelizzo, *Capped Si/Mo multilayers with improved performances at 30.4 nm for future solar missions*, Optics Express 19(15), 13963-13973 (2011).

9. M.G. Pelizzo, A.J. Corso, P. Zuppella, D.L. Windt, G. Mattei, P. Nicolosi, *Stability of EUV multiplayer coatings to low energy proton bombardment*, Optics Express 19(16), 14838-14844 (2011).

10. P. Zuppella, G. Monaco, A.J. Corso, P. Nicolosi, D.L. Windt, V. Bello, G. Mattei, M.G. Pelizzo, *Iridium/Silicon multilayers for extreme ultraviolet applications in the 20-35 nm wavelength range*, Optics Letters 36(7), 1203-1205 (2011).

11. M.G. Pelizzo, A.J. Corso, G. Monaco, P. Nicolosi, M. Suman, P. Zuppella, D. Cocco, *Multilayer optics to be used as FEL fundamental suppressors for harmonics selection*, Nuclear Instruments and Methods in Physics Research Section A 635, S24-S29 (2011).

Proceedings to conference:

1. L. Poletto, F. Frassetto, P. Miotti, A. Giglia, A. J. Corso, P. Zuppella, M.G. Pelizzo, S. Fineschi, E. Antonucci, G. Naletto, P. Nicolosi, M. Romoli, *Test of a multilayer-coated EUV grating for I-IV order spectroscopic measurements of the solar corona*, Proceeding Paper SPIE Vol. 8862, Solar Physics and Space Weather Instrumentation V, San Diego, USA on August 2013.

2. A.J. Corso, V. Polito, P. Zuppella, S. Zuccon, M. Nardello, P. Nicolosi, J. L. Maria, J. F. Mariscal, E. Quémerais, M. G. Pelizzo, *Extreme and near ultraviolet experimental facility for calibration of space instrumentation*, Proceeding Paper SPIE Vol. 8861, Optics for EUV, X-Ray, and Gamma-Ray Astronomy VI, San Diego, USA on August 2013.

3. M. Nardello, V. Polito, P. Zuppella, A. J. Corso, S. Zuccon, M. G. Sertsu, P. Nicolosi, S. Fineschi, G. Naletto, E. Antonucci, M. G. Pelizzo, *Solar alpha particles damage effects on UV and EUV optical coatings*, Proceeding Paper SPIE Vol. 8862, Solar Physics and Space Weather Instrumentation V, San Diego, USA on August 2013.

4. S. Zuccon, P. Zuppella, M. Nardello, A. J. Corso, M.G. Pelizzo, *Novel thin film materials for plasmonic applications* Proceeding Paper SPIE Vol. 8809, San Diego, Plasmonics: Metallic Nanostructures and Their Optical Properties XI, USA on August 2013.

5. V. Polito, A.J. Corso, P. Zuppella, P. Nicolosi, S. Fineschi, E. Antonucci, D.L. Windt, M.G. Pelizzo, *Analysis of optical efficiency of METIS coronagraph telescope on board the Solar Orbiter mission*, Proceeding Paper SPIE Vol. 8443, Space Telescopes and Instrumentation Conference: Ultraviolet to Gamma Ray, Amsterdam (Netherland), 84433G (2012).

6. P. Zuppella, A.J. Corso, P.Nicolosi, M.G. Pelizzo, V. Polito, J.F. Mariscal, N. Rouanet, E. Quémerais, J.L. Maria, *Radiometric calibration of PHEBUS: model and results*, Proceeding Paper SPIE Volume 8443, Space Telescopes and Instrumentation Conference Ultraviolet to Gamma Ray, Amsterdam (Netherland), 84434S (2012).

7. M.G. Pelizzo, P. Zuppella, V. Polito, A.J. Corso, P. Nicolosi, *Vacuum Facility for calibration of space instrumentation in clean room*, Proceeding Paper SPIE Volume 8443, Space Telescopes and Instrumentation Conference: Ultraviolet to Gamma Ray, Amsterdam (Netherland), 84432Q (2012).

8. M.G. Pelizzo, S. Fineschi, P. Zuppella, A.J. Corso, D. L. Windt, and P. Nicolosi, *SiC/Mg multilayer coatings for SCORE coronagraph: long term stability analysis*, SPIE Proc. 8148, San Diego, USA on August 2011 (Invited paper).

9. A.J. Corso, P. Zuppella, P. Nicolosi, M.G. Pelizzo, *Long term stability of optical coatings in close solar environment*, SPIE Proc. 8148, San Diego, USA on August 2011.

10. A.J. Corso, P. Zuppella, P. Nicolosi, D. Cocco, M.G. Pelizzo *Multilayer mirrors for FERMI@ELETTRA beam transport system*, SPIE Proc. Vol.8078, April Prague 2011.

11. M.G. Pelizzo, A.J. Corso, D. Cocco, *Delay systems and phase retarders based on multilayers coated mirrors for FEL beam manipulation*, SPIE Proc. Vol.8078, April Prague 2011.

12. P. Zuppella, A.J. Corso, P. Nicolosi, D.L. Windt, M.G. Pelizzo, *Innovative multilayer coatings for space solar physics: performances and stability over time*, SPIE Proc. Vol.8076, April Prague 2011 (Invited paper).

13. G. Monaco, A. J. Corso, P. Zuppella, P. Nicolosi, D.L. Windt, M.G. Pelizzo, *Thermal analysis experiment to evaluate the stability of multilayer coatings in a space environment close to the sun*, SPIE Proc. Vol.8077, April Prague 2011.

14. P. Nicolosi, P. Zuppella, A.J. Corso, V. Polito; M.G. Pelizzo, J. F. Mariscal, N. Rouanet, P.O. Mine, E. Quémerais, J.L. Maria, *Optical subsystem characterization in laboratory*, SPIE Proc. Vol.8076, Prague April 2011.

15. A.J. Corso, M. Suman, G. Monaco, P. Zuppella, P. Nicolosi and M.G. Pelizzo, *Multilayer coatings for METIS instrument*, International Conference on Space Optics, Rhodes (Greece) October 2010.

Bibliography

[1] E. Chassefiére, J.L. Maria, J.P. Goutail, E. Quémerais, F. Leblanc, S. Okano, I. Yoshikawa, O. Korablev, V. Gnedykh, G. Naletto, P. Nicolosi, M.G. Pelizzo, J.J. Correia, S. Gallet, C. Hourtoule, P.O. Mine, C. Montaron, N. Rouanet, J.B. Rigal, G. Muramaki, K. Yoshioka, O. Kozlov, V. Kottsov, P. Moisseev, N. Semena, J.L. Bertaux, M.Th. Capria, J. Clarke, G. Cremonese, D. Delcourt, A. Doressoundiram, S. Erard, R. Gladstone, M. Grande, D. Hunten, W. Ip, V. Izmodenov, A. Jambon, R. Johnson, E. Kallio, R. Killen, R. Lallement, J. Luhmann, M. Mendillo, A. Milillo, H. Palme, A. Potter, S. Sasaki, D. Slater, A. Sprague, A. Stern, and N. Yan. Phebus: A double ultraviolet spectrometer to observe mercury's exosphere. *Planetary and Space Science*, 58(1-2):201 – 223, 2010.

[2] M.S. Wedlund. *In-flight calibration of the PHEBUS UV instrument and Monte Carlo modelling of the hydrogen exosphere.* PhD thesis, Astronomy and Astrophysics - Université Pierre et Marie Curie, 2011.

[3] Correia A.C.M and J. Laskar. Mercury's capture into the 3/2 spin-orbit resonance as a result of its chaotic dynamics. *Nature*, (6994):848 – 850, 2004.

[4] Brian J. Anderson, Catherine L. Johnson, Haje Korth, Michael E. Purucker, Reka M. Winslow, James A. Slavin, Sean C. Solomon, Ralph L. McNutt, Jim M. Raines, and Thomas H. Zurbuchen. The global magnetic field of mercury from messenger orbital observations. *Science*, 333(6051):1859 – 1862, 2011.

[5] R. G. Strom, C. R. Chapman, W. J. Merline, S. C. Solomon, and J. W. Head. Mercury cratering record viewed from messenger's first flyby. *Science*, 321(5885):79 – 81, 2008.

[6] J. W. Head, S. L. Murchie, L. M. Prockter, M. S. Robinson, S. C. Solomon, R. G. Strom, C. R. Chapman, T. R. Watters, W. E. McClintock, D. T. Blewett, and J. J. Gillis-Davis. Volcanism on mercury: Evidence from the first messenger flyby. *Science*, 321(5885):69 – 72, 2008.

[7] Domingue D.L., Koehn P.L., Killen R.M., Sprague A.L., Sarantos M., Cheng A.F., Bradley E.T., and McClintock W.E. Mercury's atmosphere: A surface-bounded exosphere. In D.L. Domingue and C.T. Russell, editors, *The Messenger Mission to Mercury*, pages 161 – 186. Springer New York, 2007.

[8] B. Murray and E. Burgess. *Flight to Mercury*. Columbia Univ. Press, New York, 1977.

[9] NASA. The messenger mission website, http://www.nasa.gov/mission_pages/messenger/main/, 2013.

[10] Sean C. Solomon, Jr. McNutt, Ralph L., Robert E. Gold, and Deborah L. Domingue. Messenger mission overview. *Space Science Reviews*, 131(1-4):3 – 39, 2007.

[11] A.L. Broadfoot, S. Kumar, M.J.S. Belton, and M.B. McElroy. Mercury's Atmosphere from Mariner 10: Preliminary Results. *Science*, 185:166 – 169, 1974.

[12] A.L. Broadfoot, D.E. Shemansky, and S. Kumar. Mariner 10: Mercury atmosphere. *Geophysical Research Letters*, 3(10):577 – 580, 1976.

[13] N.F. Ness, K.W. Behannon, R.P. Lepping, and Y.C. Whang. Magnetic field of mercury confirmed. *Nature*, 255:204 – 205, 1975.

[14] Chase Jr. S.C., Miner E.D., Morrison D., Munch G., and Neugebauer G. Mariner 10 infrared radiometer results: Temperatures and thermal properties of the surface of mercury. *Icarus*, 28(4):565 – 578, 1976.

[15] NASA. Global mosaics of mercury, http://messenger.jhuapl.edu/the_mission/mosaics.html, 2013.

[16] Maria T. Zuber, David E. Smith, Roger J. Phillips, Sean C. Solomon, Gregory A. Neumann, Steven A. Hauck, Stanton J. Peale, Olivier S. Barnouin, James. W Head, and Catherine L. Johnson. Topography of the northern hemisphere of mercury from messenger laser altimetry. *Science*, 336(6078):217 – 220, 2012.

[17] James W. Head, Clark R. Chapman, Robert G. Strom, Caleb I. Fassett, Brett W. Denevi, David T. Blewett, Carolyn M. Ernst, Thomas R. Watters, Sean C. Solomon, and Scott L. Murchie. Flood volcanism in the northern high latitudes of mercury revealed by messenger. *Science*, 333(6051):1853 – 1856, 2011.

[18] Louise M. Prockter, Carolyn M. Ernst, Brett W. Denevi, Clark R. Chapman, James W. Head, Caleb I. Fassett, William J. Merline, Sean C. Solomon, Thomas R. Watters, and Robert G. Strom. Evidence for young volcanism on mercury from the third messenger flyby. *Science*, 329(5992):668 – 671, 2010.

[19] B.W. Denevi, M.S. Robinson, S.C. Solomon, S.L. Murchie, D.T. Blewett, D.L. Domingue, T.J. McCoy, C.M. Ernst, J.W. Head, T.R. Watters, and N.L. Chabot. The evolution of mercury's crust: A global perspective from messenger. *Science*, 324(5927):613 – 618, 2009.

[20] S.Z. Weider, L.R. Nittler, R.D. Starr, T.J. McCoy, K.R. Stockstill-Cahill, P.K. Byrne, B.W. Denevi, J.W. Head, and S.C. Solomon. Chemical heterogeneity on Mercury's surface revealed by the MESSENGER X-Ray Spectrometer. *Journal of Geophysical Research (Planets)*, 117, October 2012.

[21] W.E. McClintock, R.J. Vervack, E.T. Bradley, R.M. Killen, N. Mouawad, A.L. Sprague, M.H. Burger, S.C. Solomon, and N.R. Izenberg. MESSENGER Observations of Mercury's Exosphere: Detection of Magnesium and Distribution of Constituents. *Science*, 324:610 – 620, May 2009.

[22] R.J. Vervack, W.E. McClintock, R.M. Killen, A.L. Sprague, B.J. Anderson, M.H. Burger, E.T. Bradley, N. Mouawad, S.C. Solomon, and N.R. Izenberg. Mercury's Complex Exosphere: Results from MESSENGER's Third Flyby. *Science*, 329:672 – 675, 2010.

[23] Johannes Benkhoff, Jan van Casteren, Hajime Hayakawa, Masaki Fujimoto, Harri Laakso, Mauro Novara, Paolo Ferri, Helen R. Middleton, and Ruth Ziethe. Bepicolombo - comprehensive exploration of mercury: Mission overview and science goals. *Planetary and Space Science*, 58(1-2):2 – 20, 2010. <ce:title>Comprehensive Science Investigations of Mercury: The scientific goals of the joint ESA/JAXA mission BepiColombo</ce:title>.

[24] ESA. Bepicolombo homepage, http://sci.esa.int/bepicolombo/, 2013.

[25] Rouanet N., Mariscal J.F., and PHEBUS team. Cwp05 - qm results field of view measurement report. Technical report, LATMOS, 2013.

[26] Rouanet N., Mariscal J.F., and PHEBUS team. Cwp06 - qm results scanner exit slit field of view measurement. Technical report, LATMOS, 2013.

[27] K. Yoshioka, K. Hikosaka, G. Murakami, I. Yoshikawa, A. Yamazaki, and H. Nozawa. Development of the euv detector for the bepicolombo mission. *Advances in Space Research*, 41(9):1392 – 1396, 2008.

[28] K. Yoshioka, G. Murakami, I. Yoshikawa, J.-L. Maria, J.-F. Mariscal, N. Rouanet, P.-O. Mine, and E. Quemerais. Optical performance of phebus/euv detector onboard bepicolombo. *Advances in Space Research*, 49(8):1265 – 1270, 2012.

[29] Killen R., Shemansky D., and Mouawad N. Expected emission from mercury's exospheric species, and their ultraviolet-visible signatures. *The Astrophysical Journal Supplement Series*, 181(2):351, 2009.

[30] A.E. Potter and T.H. Morgan. Potassium in the atmosphere of mercury. *Icarus*, 67(2):336 – 340, 1986.

[31] Mariscal J.F., Rouanet N., and PHEBUS team. Optical ground calibration plan - issue 2. Technical report, LATMOS, 2013.

[32] Goldstein D. and Goldstein D.H. *Polarized light - Second edition*, chapter 3. Marcel Dekker, Inc., 2003.

[33] Pedrotti F.L., L.S. Pedrotti, and L.M. Pedrotti. *Introduction to optics - Third edition*, chapter 4. Pearson Education, Inc., 2007.

[34] Hurwitz H. and R.C. Jones. A new calculus for the treatment of optical systems. *Journal of the Optical Society of America*, 31(7):493–495, 1941.

[35] Goldstein D. and Goldstein D.H. *Polarized light - Second edition*, chapter 8. Marcel Dekker, Inc., 2003.

[36] Goldstein D. and Goldstein D.H. *Polarized light - Second edition*, chapter 4. Marcel Dekker, Inc., 2003.

[37] Goldstein D. and Goldstein D.H. *Polarized light - Second edition*, chapter 5. Marcel Dekker, Inc., 2003.

[38] Goldstein D. and Goldstein D.H. *Polarized light - Second edition*, chapter 6. Marcel Dekker, Inc., 2003.

[39] Born M. and Wolf E. *Principles of Optics: Electromagnetic Theory of Propagation, Interference and Diffraction of Light - 7th Edition*, chapter 14. Cambridge University Press, 1999.

[40] Goldstein D. and Goldstein D.H. *Polarized light - Second edition*, chapter 8. Marcel Dekker, Inc., 2003.

[41] Allen Jr J.E. and Penn M.J. Polarization in mercury's exosphere. In *Astronomical Polarimetry: Current Status and Future Directions*, volume 343, page 181, 2005.

[42] Buenzli E., Schmid H.M., and Joos F. Polarization models for rayleigh scattering planetary atmospheres. *Earth, Moon, and Planets*, 105(2 - 4):153 – 157, 2009.

[43] Tomc J., Zetner P., Westerveld W.B., and McConkey J.W. Variations in the polarization sensitivity of microchannel plates with photon incidence angle and wavelength in the vuv. *Applied Optics*, 23(5):656 – 657, 1984.

[44] D. L. Windt. Imd - software for modeling the optical properties of multilayer films. *Comput. Phys.*, 12(4):360–370, 1998.

[45] E.D. Palik. *Handbook of optical constants of solids*. Elsevier, 1994.

[46] Windt D.L., Jr. W.C. Cash, Scott M., Arendt P., Newnam B., Fisher R.F., Swartzlander A.B., Takacs P.Z., and Pinneo J.M. Optical constants for thin films of c, diamond, al, si, and cvd sic from 24 a to 1216 a. *Applied Optics*, 27(2):279 – 295, 1988.

[47] International Intellectual Group Inc. Pcgrate software - http://www.pcgrate.com/, 2013.

[48] Zuppella P., Corso A.J., Polito V., Mariscal J.F., Rouanet N., Maria J.L., Nicolosi P., Quemerais E., and Pelizzo M.G. Optical subsystems calibration and derived radiometric instrument response of the phebus spectrometer on board of the bepicolombo mission. *Journal of Instrumentation*, 7(10):P10023, 2012.

[49] Mariscal J.F., Rouanet N., and PHEBUS team. Cwp 1, 2, 3 and 4: Geometric factor simulation. Technical report, LATMOS, 2013.

[50] W.T. Welford. Vi aberration theory of gratings and grating mountings. In E. Wolf, editor, *Progress in Optics*, volume 4 of *Progress in Optics*, pages 241 – 280. Elsevier, 1965.

[51] Lieberman M.A. and Lichtenberg A.J. *Principles of Plasma Discharges and Materials Processing*. John Wiley and Sons, New York, 2005.

[52] Brodie K. and Neate S. Features and operation of hollow cathode lamps and deuterium lamps. Technical report, Varian, 1988. http://www.chem.agilent.com/Library/Support/Documents/Varian_FAQs/aa-083.pdf.

[53] D. Bertram, M. Born, and T. Justel. Incoherent light sources. In Frank Trager, editor, *Springer Handbook of Lasers and Optics*, pages 623 – 640. Springer Berlin Heidelberg, 2012.

[54] Kume H., Okano K., Sakai S., Yamashita K., Kamiya A., Taguchi T., Morita T., Tomiyama K., Watanabe T., Suzuki S., Nakanura M., Yamaguchi H., Hasegawa Y., Ogawa T., Uchiyama N., and Uchizono D. *Photomultiplier tube: principle and application*. Hamamatsu Photonics K.K., 1994.

[55] HAMAMATSU PHOTONICS K.K. Electron Tube Division. *Photomultiplier tube Hamamatsu catalog*, 2005.

[56] G.W. Goodrich and W.C. Wiley. Continuos channel electron multiplier. *Review of Scientific Instruments*, 1962.

[57] AMPTEKTRON. *The MD-501 AMPTEKTRON datasheet*, 2001.

[58] Mónica Fernández-Perea, José A. Méndez, José A. Aznárez, and Juan I. Larruquert. In situ reflectance and optical constants of ion-beam-sputtered sic films in the 58.4 to 149.2 nm region. *Applied Optics*, 48(24):4698 – 4702, 2009.

[59] Juan I. Larruquert, Antonio P. Pérez-Marín, Sergio García-Cortés, Luis Rodríguez de Marcos, José A. Aznárez, and José A. Méndez. Self-consistent optical constants of sic thin films. *Journal of Optical Society of America A*, 28(11):2340 – 2345, 2011.

[60] G. Monaco, M. Gastaldi, P. Nicolosi, M. G. Pelizzo, E. Gilioli, S. Rampino, F. Bissoli, F. Pattini, S. Agnoli, G. Granozzi, and N. Manuzzato. Silicon carbide thin films for euv and soft x-ray applications. *The European Physical Journal Special Topics*, 169(1):159 – 165, 2009.

[61] G. Monaco, D. Garoli, M. Natali, M.G. Pelizzo, and P. Nicolosi. Synthesis of heteroepytaxial 3c-sic by means of pld. *Applied Physics A*, 105(1):225–231, 2011.

[62] BEAR beamline team. Homepage of bear beamline - http://www.elettra.trieste.it/it/lightsources/elettra/elettra-beamlines/bear/bear.html, 2013.

[63] Namioka T. Theory of the concave grating. iii. seya-namioka monochromator. *Journal of the Opttical Society of America*, 49(10):951 – 959, 1959.

[64] Ocean optics. Homepage of usb4000 spectromiter - http://www.oceanoptics.com/products/usb4000.asp, 2013.